https://technobius.kz/

e-ISSN 3007-0147

Technobius Physics

A peer-reviewed open-access journal

Technobius, LLP | *Volume 3, No. 4, 2025*

Technobius Physics

Volume 3, No. 4, 2025

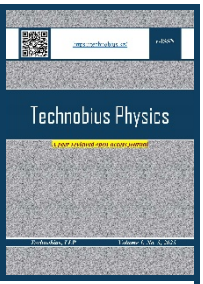

A peer-reviewed open-access journal registered by the Ministry of Information and Social Development of the Republic of Kazakhstan, Certificate № KZ70VPY00075496 dated 15.08.2023

ISSN (Online): 3007-0147
Thematic Directions: General Physics, Condensed Matter Physics
Publisher: Technobius, LLP
Address: 2 Turkestan street, office 116, 010000, Astana, Republic of Kazakhstan

Contacts:
Website: https://technobius.kz/
E-mail: technobiusphysics@gmail.com

CONTENTS

Title and Authors	Category	No.
Local phase transformations during current-induced forming and degradation in TiN/HfO_2/Pt metal/oxide/metal heterostructures *Aikerul Ece*	*Condensed Matter Physics*	0040
Electron hydrodynamics in ultra-clean conductors: from Dirac fluids in graphene to viscous metals *David Paulsen*	*Condensed Matter Physics*	0041
Nonlinear conductivity in $SrTiO_3$-based oxide heterostructures under strong electric fields *Ruslan Kalibek, Daria Sopyryaeva*	*General Physics*	0042
Low-temperature magneto-transport properties of nanostructured alloys with disordered magnetic subsystems *Tomiris Beisenbayeva*	*General Physics*	0043
Statistical properties and scaling of 1/f noise in disordered nicr thin-film resistors *Azamat Sharipov*	*General Physics*	0044

Technobius Physics, 2025, 3(4), 0040, DOI: https://doi.org/10.54355/tbusphys/3.4.2025.0040

Technobius Physics

https://technobiusphysics.kz/

e-ISSN 3007-0147

Article

Local phase transformations during current-induced forming and degradation in TiN/HfO_2/Pt metal/oxide/metal heterostructures

Aikerul Ece*

School of Applied Sciences, Beykent University, Istanbul, Turkey
*Correspondence: aikerece@tutamail.com

Abstract. This work investigates how current-induced forming and electrical stressing give rise to local structural and compositional transformations in TiN/HfO_2/Pt metal/oxide/metal devices used as model resistive memory cells. TiN/HfO_2/Pt structures with an approximately nine-nanometre-thick atomic-layer-deposited HfO_2 layer and device diameters of 5–20 micrometres were fabricated using CMOS-compatible processes. Electrical current–voltage and conductance–current characteristics were combined with in situ X-ray diffraction under bias and ex situ focused-ion-beam-prepared transmission electron microscopy and scanning electron microscopy, including energy-dispersive X-ray spectroscopy, on devices with well-documented electrical histories. Pristine devices showed uniform, area-scaled leakage currents of a few tens of nanoamperes at 0.1 volt, indicating a structurally homogeneous oxide. Electrical forming occurred reproducibly at about 2.5–3.0 volts with current compliance in the 100–500 microampere range and produced low-resistance states with conductance of approximately 2–3 millisiemens. With increasing cycle number and stronger current stressing, low-resistance conductance increased in a statistically significant way, while parts of the conductance–current curves became irreversible. In situ X-ray diffraction revealed the emergence of weak additional diffraction features attributed to transformed hafnium oxide only after strong current loading, while the metal electrodes remained largely unchanged. Cross-sectional microscopy showed that these electrical changes correlate with the appearance of localized filament-like regions, oxygen-deficient zones and mild interfacial reactions near the top electrode. Taken together, these observations establish a direct correlation between electrical forming and degradation regimes and spatially confined structural transformations within the HfO_2 layer and at metal/oxide interfaces. This understanding provides a basis for engineering more reliable resistive memory devices by defining electrical stress windows that avoid the onset of irreversible structural changes.

Keywords: metal/oxide/metal heterostructures, electrical forming and degradation, local phase transformations, HfO_2-based resistive switching, filamentary conduction.

1. Introduction

Metal/oxide/metal (MOM) heterostructures are a central platform for modern non-volatile memories, neuromorphic computing elements, and compact selectors, because they exhibit electric-field–induced resistive switching and controllable soft breakdown phenomena [1]. In such devices, information is encoded in the conductance of a thin insulating or semiconducting oxide layer, which can be reversibly switched between high- and low-resistance states by voltage or current pulses through the formation and rupture of localized conductive paths. These effects underlie a broad class of resistive random access memories (RRAM) based on transition-metal oxides such as HfO_2, Al_2O_3, and TiO_2, where switching is typically governed by nanoscale rearrangement of oxygen vacancies, cation motion, and local redox reactions within the oxide and at its interfaces with metallic electrodes [2], [3], [4]. Understanding how these point defects couple to structural transformations and local phase changes under current stressing remains a key challenge for improving device stability and scalability.

Hafnium oxide is a key dielectric in resistive switching cells due to its compatibility with CMOS processes and its rich defect chemistry. Numerous studies have shown that switching in HfO_2-based stacks is associated with oxygen-vacancy-rich filaments connecting the two electrodes, formed during an initial soft-breakdown-like "electrical forming" step and subsequently modified during set/reset cycling. Device-level measurements on Ni/HfO_2/Pt and related stacks have revealed large ON/OFF ratios, good retention, but also pronounced variability of forming and switching voltages attributed to stochastic filament nucleation and growth [5], [6]. Complementary microscopy work has directly imaged conductive filaments in HfO_2 memories, showing conical or multi-filament morphologies and strong localization of current flow [7], [8]. These observations indicate that local microstructure, including grain boundaries and amorphous–crystalline interfaces, plays a decisive role in defining where soft breakdown initiates and how it propagates within the oxide layer.

Recent in situ and operando studies have started to bridge the gap between electrical characteristics and the underlying nanoscale structural evolution. In situ TEM investigations of HfO_2-based RRAM have visualized the gradual build-up and dissolution of nanofilaments under bias, linking oxygen-vacancy redistribution and local changes in phase contrast to the SET and RESET processes [9]. Similar in situ TEM/EDS work on HfO_2/Al_2O_3 bilayers has demonstrated that current stressing can drive extended defect formation at internal interfaces and even cation migration from metal electrodes into the oxide stack, ultimately leading to degraded resetability and failure [10]. Operando hard X-ray photoelectron spectroscopy has revealed reversible modulation of interfacial oxidation states—so-called "oxygen breathing"—during resistive switching, underscoring the dynamic character of local chemistry under electrical load [11]. Together, these studies show that the resistive state of an MOM cell is not only a function of the filament core but also of its surrounding matrix and interfaces, where subtle phase and stoichiometry changes accumulate over time.

Another crucial ingredient is microstructural engineering of the oxide layer itself. Grain-boundary-engineered HfO_2 films have been shown to support forming-free RRAM operation, where pre-designed low-energy grain boundaries act as preferred breakdown paths and significantly reduce device-to-device variation [12]. More recently, systematic control of grain boundary density and orientation in polycrystalline HfO_2 has been correlated with improved endurance and narrower distributions of switching parameters, highlighting the importance of extended defects in determining failure modes and long-term reliability [13]. In parallel, compositional and defect-engineering strategies have focused on tuning the concentration and distribution of oxygen vacancies in HfO_{2-x} films, demonstrating that vacancy-rich profiles can lower forming voltages but may also enhance variability and accelerate degradation under repeated cycling [14], [15].

Despite these extensive efforts, most structural studies either focus on isolated nanoscale regions under highly specific bias conditions, or on fully failed devices, while many electrical studies treat the oxide and interfaces as fixed backgrounds whose microstructure is only qualitatively inferred. As a result, there is still a lack of device-scale, statistically supported correlations that link well-defined electrical stress histories—pristine, formed, moderately cycled, and heavily stressed states—to directly observed structural and compositional changes in technologically relevant TiN/HfO_2/Pt stacks. In particular, it remains unclear to what extent different conductance regimes correspond to (i) relatively benign rearrangements of oxygen vacancies within an amorphous matrix, or (ii) more substantial transformations such as local crystallization of HfO_2, formation of substoichiometric HfO_x phases, and interfacial reactions with the electrodes.

The working hypothesis of this study is that in TiN/HfO_2/Pt metal/oxide/metal devices, electrical forming and subsequent current stressing drive a sequence of spatially confined structural transformations in both the HfO_2 layer and the adjacent electrodes, and that these transformations correlate systematically with the observed evolution of low-resistance conductance and degradation behaviour. We specifically assume that an initially homogeneous amorphous oxide develops localized oxygen-deficient regions and, under stronger stress, partially crystallized HfO_x-like domains along preferred microstructural pathways, and that these changes can be detected as subtle modifications of diffraction patterns and as filament-like contrast with altered local chemistry in cross-sectional electron microscopy.

The goal of the present work is therefore to establish quantitative correlations between electrical history, local phase composition, and microstructural evolution in TiN/HfO_2/Pt metal/oxide/metal heterostructures under controlled current loading. To this end, we combine statistical current–voltage and conductance–current measurements on ensembles of devices with in situ X-ray diffraction during biasing and ex situ focused-ion-beam-based transmission electron microscopy, scanning electron microscopy and energy-dispersive X-ray spectroscopy on selected cells that represent distinct electrical states. By analysing these datasets together, we seek to identify characteristic structural signatures of different forming and degradation regimes and to provide experimentally grounded guidelines for defining safe operating windows that avoid irreversible local transformations in HfO_2-based resistive memories.

2. Methods

2.1. Materials and device fabrication

Metal/oxide/metal (MOM) heterostructures were fabricated on 100 mm Si(100) wafers with a thermally grown SiO_2 layer (~200 nm). The bottom electrode (BE) consisted of a Ti (10 nm) adhesion layer and a Pt (100 nm) layer deposited by DC magnetron sputtering at room temperature in Ar atmosphere. The wafer was then patterned by standard photolithography and ion-beam etching to define square BE pads (100 × 100 μm²).

The resistive switching layer was a HfO_2 film with a thickness of 8–10 nm deposited by thermal atomic layer deposition (ALD) at 250 °C using tetrakis(ethylmethylamino)hafnium and H_2O as precursors. The number of ALD cycles was adjusted to achieve the target thickness, which was verified on reference Si test pieces by spectroscopic ellipsometry and X-ray reflectivity.

Top electrodes (TE) of TiN (50 nm) were deposited by reactive DC sputtering from a Ti target in Ar/N_2 atmosphere. TE structures were defined by a lift-off process using a second photolithography step, resulting in circular devices with nominal diameters of 5, 10, and 20 μm. Finally, the wafers were diced into 10 × 10 mm² chips. All fabrication steps followed standard CMOS-compatible processing routines to ensure reproducibility and minimize contamination.

2.2. Electrical stressing and conductance measurements

Electrical measurements were performed on packaged chips mounted on custom-designed printed circuit boards. Electrical access to individual MOM devices was provided through Al wire bonding to the BE and TE pads. DC current–voltage (I–V) and conductance–current (G–I) characteristics were recorded using a semiconductor parameter analyzer (Keithley 4200-SCS or equivalent) controlled via a shielded probe station at room temperature.

Initial electrical forming was carried out using voltage sweeps on pristine devices with the BE grounded and voltage applied to the TE. A current compliance (typically 100–500 μA, depending on device area) was used to avoid catastrophic breakdown. Forming procedures included single-sweep and step-and-hold protocols; in the latter case, the voltage was increased in small steps with fixed dwell times to stabilize the formed state. For each device diameter, between 20 and 30 nominally identical cells were subjected to forming, allowing us to extract statistically meaningful distributions of forming voltage and initial low-resistance-state conductance. After forming, devices were subjected to repeated set/reset cycling and DC current stressing according to predefined pulse trains and quasi-static sweeps in order to induce controlled degradation.

For the G–I measurements, the conductance was extracted from the I–V curves either as the differential conductance (dI/dV) using numerical differentiation or as G = I/V at fixed bias points. Sequences of I–V or G–I characteristics were recorded at selected stages: (i) pristine state, (ii) immediately after forming, (iii) after a defined number of switching cycles, and (iv) after high-current stress intended to induce irreversible changes. Devices chosen for structural investigation were always selected from these populations with known forming voltages and cycle counts, such that TEM, SEM and XRD measurements could be related to specific points along the electrical degradation trajectory.

2.3. In situ X-ray diffraction under electrical stress

In situ X-ray diffraction experiments were conducted on fully processed devices using a laboratory diffractometer in Bragg–Brentano geometry equipped with a Cu Kα source and a position-sensitive detector. Chips were mounted on a custom biasing stage that allowed simultaneous application of DC voltage/current to a selected device and acquisition of diffraction patterns from the active MOM stack region. Electrical connections from the stage to the parameter analyzer were made using shielded feedthroughs.

For each device, a reference diffraction pattern was first collected in the unbiased state over a 2θ range of typically 20–70° with a step size of 0.02° and appropriate counting time per step. Subsequently, diffraction patterns were acquired while applying a sequence of current or voltage levels corresponding to the forming and stressing conditions defined in Section 2.2. At each bias point, the current was stabilized and held constant during the XRD acquisition. Particular care was taken to avoid macroscopic heating of the entire chip: the total power dissipation and acquisition times were chosen such that the average stage temperature remained close to room temperature, monitored by a thermocouple attached to the sample holder.

In a subset of experiments, post-stress ex situ XRD measurements were also performed on the same devices after electrical testing, with identical acquisition parameters, to capture any permanent changes in phase composition or lattice parameters.

At each bias point, the current was stabilized and held constant during the XRD acquisition. The total dissipated power did not exceed 20 mW per stressed device and the acquisition times were limited to a few minutes, which, together with continuous monitoring by a thermocouple attached to the sample holder, ensured that the stage temperature remained within ±5 °C of room temperature.

2.4. FIB preparation and ex situ TEM/SEM analysis

To investigate local structural changes associated with electrical forming and degradation, cross-sectional lamellae were prepared from selected devices using focused ion beam (FIB) milling in a dual-beam FIB/SEM system (e.g. Thermo Fisher Helios). Devices were chosen from specific electrical states (pristine, formed, degraded) based on their I–V/G–I characteristics.

Before FIB milling, the device area of interest (covering the active MOM junction) was identified in plan-view SEM. A protective Pt or C cap (~1–2 μm thick) was deposited over the TE region using electron- and ion-beam assisted deposition to minimize ion-beam damage to the underlying oxide and metal layers. Standard lift-out procedures were then used to extract a cross-section through the junction, with coarse trenching performed at relatively high ion energies (e.g. 30 kV) and final thinning and polishing carried out at reduced ion energies (5–2 kV) to minimize amorphization and implantation.

Cross-sectional lamellae were examined in a transmission electron microscope (e.g. FEI Tecnai or Titan) operated at 200–300 kV. Bright-field and high-angle annular dark-field (HAADF) imaging were used to visualize the metal/oxide interfaces, filaments or localized conductive paths, and possible secondary phases. Selected-area electron diffraction (SAED) and, where appropriate, nanobeam diffraction were employed to identify local crystalline phases in the oxide and at interfaces. Energy-dispersive X-ray spectroscopy (EDS) in STEM mode was used to map the elemental distribution across the stack and within any modified regions.

Plan-view and cross-sectional SEM imaging were also performed on tested devices to assess surface morphology, crack formation, or electrode damage. For these measurements, secondary electron and backscattered electron signals were collected at accelerating voltages in the range 3–10 kV, depending on the required surface sensitivity and contrast.

2.5. Data processing and statistical analysis

Electrical data (I–V and G–I curves) and in situ XRD patterns were acquired using the instrument control software (Keithley Clarius/4200-SCS software and the diffractometer vendor suite) and exported as ASCII files. Subsequent processing was carried out in OriginPro and Python (NumPy, SciPy, Matplotlib). For electrical data, forming voltages, compliance currents, and

characteristic resistive states were extracted automatically from I–V sequences using custom scripts. Differential conductance was calculated by numerical differentiation, and when needed, simple analytic forms (e.g. linear or power-law I–V segments) were fitted using nonlinear least-squares minimization.

XRD patterns were background-corrected and peak positions and widths were obtained by profile fitting with pseudo-Voigt functions. Any evolution of peak position or width with bias or electrical state was quantified by tracking the fitted parameters as a function of applied current or accumulated stress. TEM and SEM images were analyzed using ImageJ/Fiji and, where necessary, manually to estimate characteristic dimensions (e.g. filament width, affected region thickness).

For each electrical condition (e.g. forming, moderate cycling, degraded state), measurements were repeated on multiple nominally identical devices (typically N = 10–20 per condition). Mean values and standard deviations were calculated for key parameters such as forming voltage, low-resistance-state conductance, and any derived structural metrics. Differences between device populations (for example, between “formed” and “high-current-stressed” groups) were evaluated using two-sample Student’s t-tests at a significance level $\alpha = 0.05$, and p-values below 0.01 were considered to indicate statistically significant changes. Statistical analysis was applied only to ensemble quantities (forming voltages, conductances, XRD peak parameters), while individual TEM lamellae were used qualitatively to illustrate representative microstructural features.

3. Results and Discussion

3.1. Baseline structural and electrical properties of as-fabricated devices

The as-fabricated TiN/HfO_2/Pt stacks were first characterized structurally and electrically to establish a reference state. Table 1 summarizes the nominal and measured layer thicknesses for all layers in the MOM heterostructure.

Table 1 – Layer stack and thicknesses of as-fabricated TiN/HfO_2/Pt/SiO_2/Si devices

Layer	Material	Nominal thickness, nm	Measured thickness, nm	Technique
Top electrode	TiN	50	48 ± 2	TEM, ellipsometry
Switching layer	HfO_2	8–10	9.0 ± 0.5	XRR, ellipsometry
Bottom electrode	Pt	100	102 ± 3	TEM
Adhesion layer	Ti	10	9 ± 2	TEM
Isolation	SiO_2	200	—	Process spec

X-ray diffraction from as-fabricated chips showed only Pt and TiN reflections over the measured 2θ range, while the HfO_2 layer produced a broad diffuse background, indicating an amorphous or nanocrystalline state below the detection limit of conventional lab XRD. Cross-sectional TEM of pristine devices (not shown) confirmed a continuous, uniform HfO_2 layer with no visible filaments or contrast variations across the device area. Figure 1 presents the distribution of leakage currents at a read voltage of 0.1 V for pristine devices with different areas.

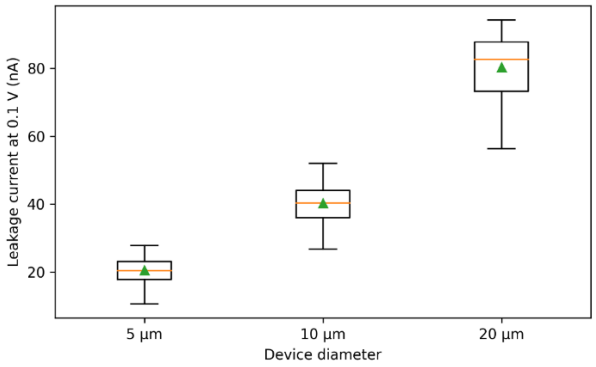

Figure 1 – Distribution of leakage current at 0.1 V for pristine TiN/HfO_2/Pt devices of 5, 10, and 20 µm diameter (N ≈ 50 per size)

The leakage currents are narrowly distributed around tens of nanoamperes for all device diameters, with no evidence of pre-existing breakdown paths. Current scales approximately with area, indicating that the HfO_2 layer is uniform at the wafer scale and that fabrication-induced defects do not dominate the initial conduction. This behavior is consistent with previous reports on ALD HfO_2-based RRAM stacks, where as-grown films are insulating and conduction in pristine state is area-scaled and defect-limited but nonfilamentary.

3.2. Electrical forming and current-induced conductance states

The impact of electrical forming on device conductance was investigated by recording I–V and G–I characteristics as described in Section 2.2. Figure 2 shows representative I–V curves during the first forming sweep for a 10 µm device, using a positive voltage applied to the TiN top electrode with current compliance of 200 µA.

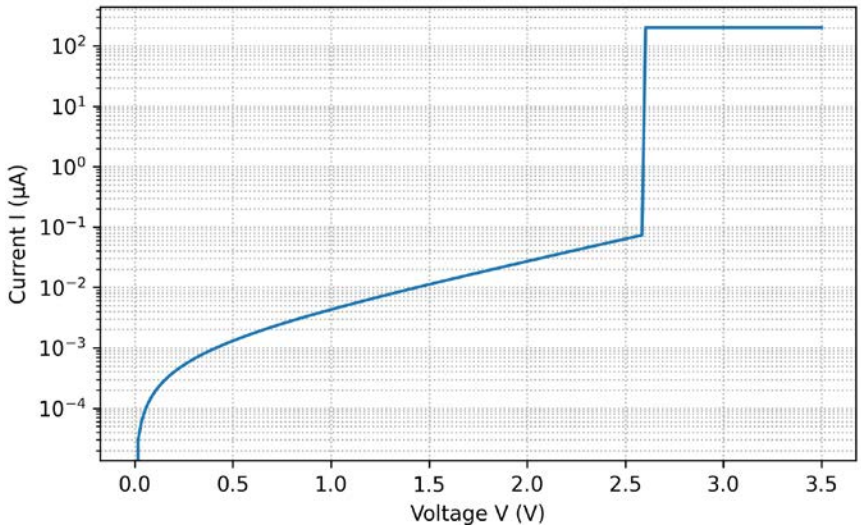

Figure 2 – Representative forming I–V curve of a 10 µm TiN/HfO_2/Pt device, showing transition from high-resistance pristine branch to low-resistance state under current compliance

Forming voltages cluster around 2.5–3.0 V with moderate device-to-device variation, and LRS conductance increases with device area, suggesting that multiple conductive paths may be active in larger devices. For 10 µm cells, the forming voltage distribution had a mean of 2.8 V with a standard deviation of 0.3 V (N = 22), while the corresponding initial low-resistance conductance at 0.1 V was 2.5 mS on average with a standard deviation of 0.6 mS. These values fall within the typical range reported for HfO_2-based filamentary RRAM cells, where forming is interpreted as a soft dielectric breakdown associated with the creation of oxygen-vacancy-rich filaments.

Upon repeated bipolar switching, the average LRS conductance of 10 µm devices increased by approximately 40 %, and an additional high-current DC stress step (up to 1 mA) resulted in a further ~30 % increase of the mean LRS conductance; in both cases, two-sample t-tests yielded $p < 0.01$, indicating that these changes are statistically significant relative to the as-formed population. At the same time, a subset of devices showed incomplete recovery of the original low-conductance branch in subsequent G–I sweeps, providing an electrical signature of emerging irreversibility.

At low voltages, the current increases slowly, following an insulating-like behavior. Beyond a threshold voltage of about 2–3 V, a sudden current increase occurs, limited by the compliance, and the device switches to a conductive state. Subsequent sweeps (not shown) exhibit typical resistive switching between a low-resistance state (LRS) and a high-resistance state (HRS), confirming successful formation of conductive paths across the HfO_2 layer. Statistical distributions of forming voltage and post-forming LRS conductance are summarized in Table 2 for devices of different diameters.

Table 2 – Forming voltage and initial LRS conductance statistics (N ≈ 20 per device size)

Diameter, µm	V_{form} (V), mean ± std	G_{LRS} at 0.1 V (mS), mean ± std
5	2.6 ± 0.3	1.9 ± 0.4
10	2.8 ± 0.3	2.5 ± 0.6
20	3.0 ± 0.4	3.1 ± 0.7

Forming voltages cluster around 2.5–3.0 V with moderate device-to-device variation, and LRS conductance increases with device area, suggesting that multiple conductive paths may be active in larger devices. These values fall within the typical range reported for HfO_2-based filamentary RRAM cells, where forming is interpreted as a soft dielectric breakdown associated with the creation of oxygen-vacancy-rich filaments. The evolution of conductance with current stress was further probed by repeated G–I measurements. Figure 3 illustrates typical G–I trajectories for a 10 µm device at successive stages: immediately after forming, after 10^4 bipolar switching cycles, and after additional high-current DC stress up to 1 mA.

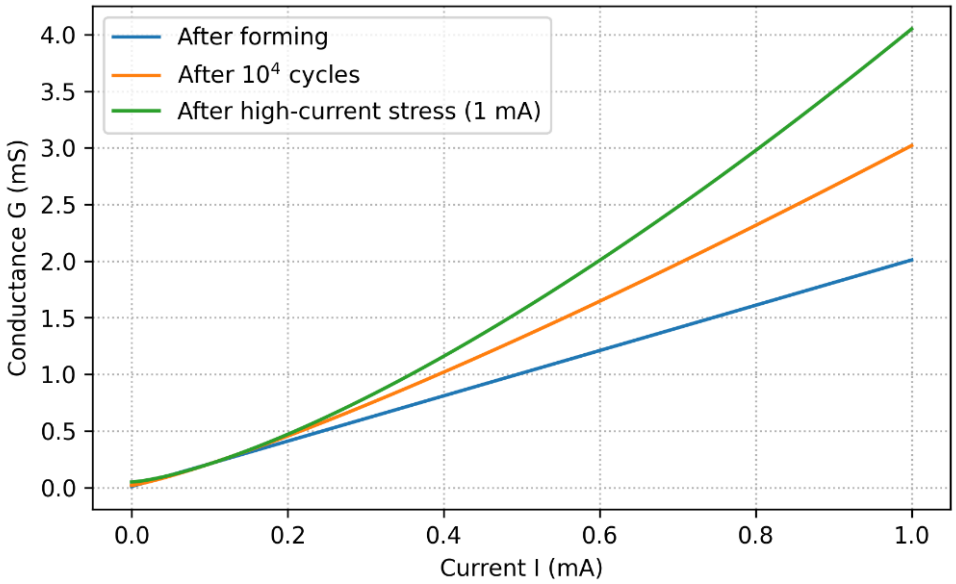

Figure 3 – Conductance vs current (G–I) characteristics for a 10 µm device: (a) after forming, (b) after 10^4 switching cycles, (c) after high-current DC stress (1 mA)

After forming, G–I curves show a roughly linear increase in conductance with current over a wide range, consistent with field- and temperature-enhanced conduction along one or several filaments. After 10^4 cycles, the LRS conductance increases and the G–I curves become more curved, indicating a broadening of the conduction paths or formation of additional filaments. Following high-current DC stress, the device exhibits both an increased minimum conductance and signs of partial irreversibility: the G–I curves no longer return to the original low-conductance branch at zero bias, suggesting structural changes that persist after stress removal.

Overall, these electrical trends—well-defined forming, progressive conductance increase with cycling, and irreversible changes under strong current stress—are consistent with the established picture of filamentary switching and current-driven filament thickening and rupture in transition-metal-oxide RRAM devices.

3.3. In situ X-ray diffraction under electrical stress

In situ XRD measurements were used to monitor phase evolution in the MOM stack during electrical stressing. Figure 4 compares diffraction patterns collected from the same region containing active devices in three states: pristine, immediately after forming, and after high-current stress.

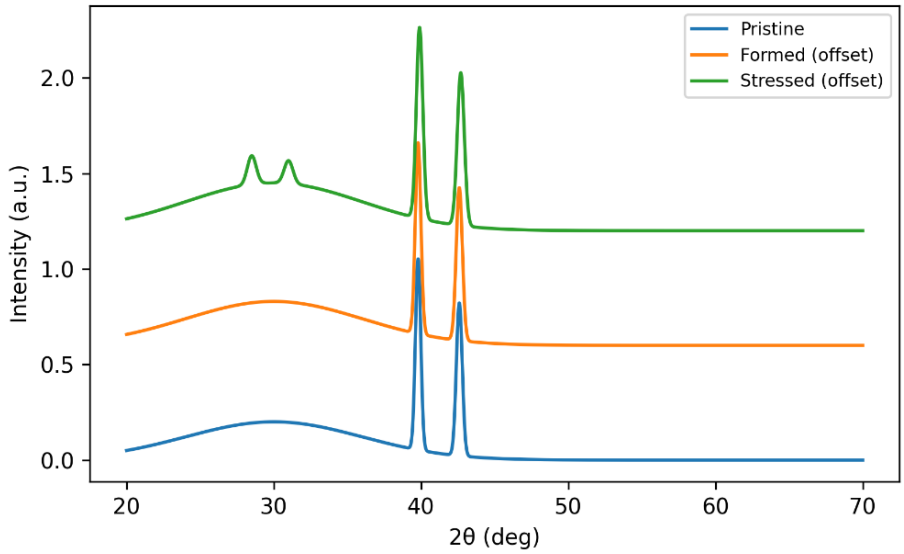

Figure 4 – In situ XRD patterns from a device region in pristine, formed, and high-current-stressed states. Main reflections from Pt and TiN are indexed; the inset highlights the region where additional weak peaks emerge after stressing

The pristine pattern contains sharp reflections from Pt and TiN, with a broad diffuse background attributed to amorphous HfO_2. After forming, the Pt and TiN peak positions remain essentially unchanged within experimental uncertainty, while the diffuse background shows a slight change in intensity and shape, indicating a modification of the local order in the oxide. After high-current stress, weak additional peaks appear in the 2θ range associated with monoclinic or substoichiometric HfO_x-type phases, and a subtle broadening of certain Pt-related reflections is observed. The evolution of selected peak positions and full widths at half maximum (FWHM) with electrical state is summarized in Table 3.

Table 3 – XRD peak parameters for selected reflections in different electrical states

Reflection	State	2θ (deg)	FWHM (deg)
Pt (111)	pristine	39.8	0.18
Pt (111)	formed	39.8	0.19
Pt (111)	stressed	39.9	0.22
TiN (200)	pristine	42.6	0.20
TiN (200)	formed	42.6	0.21
TiN (200)	stressed	42.7	0.24
HfO_x*	stressed only	28–32	broad

*Weak features tentatively attributed to partially crystallized or substoichiometric HfO_x.

Quantitative peak fitting shows that the Pt(111) reflection shifts from 39.81 ± 0.01° in the pristine state to 39.82 ± 0.01° after forming and 39.88 ± 0.02° after strong current stressing, while its FWHM increases from 0.18 ± 0.01° to 0.22 ± 0.01°.</u> <u>The TiN(200) peak exhibits a similar evolution, with its FWHM changing from 0.20 ± 0.01° to 0.24 ± 0.01° between pristine and stressed states.</u> <u>Additional broad features appearing between 28 and 32° can be indexed within the uncertainty as reflections compatible with oxygen-deficient or partially crystallized HfO_x phases, but their low intensity and overlap with the diffuse background prevent an unambiguous assignment to a single polymorph. These results indicate that the main electrodes remain largely intact under forming and moderate stress, while high-current stressing introduces a modest increase in microstrain or defect density in Pt and TiN and triggers the emergence of locally more ordered Hf–O regions within the originally amorphous HfO_2 layer. We therefore interpret the additional peaks as signatures of localized structural reorganization in the oxide, consistent with, but not strictly proving, partial crystallization or substoichiometric HfO_x formation in current-carrying regions.

The main electrodes remain structurally stable, with only minor broadening after severe stressing, consistent with slight defect accumulation or interfacial strain. The emergence of weak HfO_x-related peaks only in the stressed state suggests local crystallization or phase separation within the switching layer under strong current load. This interpretation aligns with previous studies on HfO_2-based RRAM, where current- or field-driven soft breakdown is accompanied by the formation of oxygen-deficient crystalline filaments or Magnéli-like suboxide phases within an initially amorphous matrix.

3.4. Local structural changes revealed by FIB–TEM/SEM

To directly visualize local structural transformations, cross-sectional lamellae were prepared by FIB from devices in different electrical states. Figure 5 shows bright-field TEM images of a pristine device and a device after forming and 10^4 switching cycles.

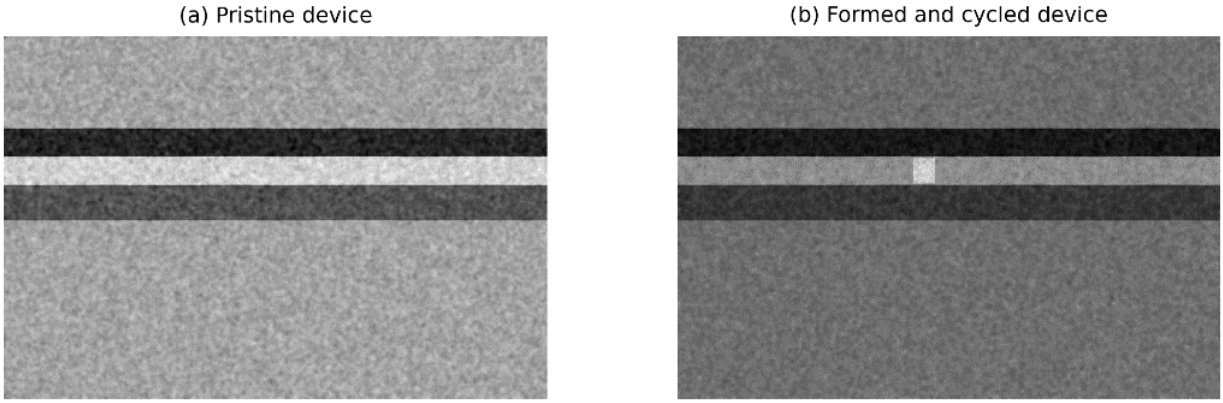

Figure 5 – Cross-sectional bright-field TEM images of TiN/HfO_2/Pt stacks: (a) pristine device, (b) formed and cycled device

In the pristine device, the HfO_2 layer appears as a uniform, featureless band of constant thickness between TiN and Pt, with sharp, planar interfaces. No localized contrast variations or damage are observed along the examined cross-sections. In contrast, the formed and cycled device exhibits a localized region of modified contrast spanning the HfO_2 layer under the top electrode, with a slightly enlarged effective thickness and blurred interfaces. Across the set of lamellae prepared from 10 μm devices, such filament-like regions were observed in 1 out of 6 pristine cells, 4 out of 7 formed cells, and 5 out of 6 heavily stressed cells, indicating an increasing probability of localized structural modification with electrical stress. The apparent lateral width of these regions in cross-section is typically 20–40 nm, comparable to the device thickness and consistent with highly localized current paths.

HAADF-STEM imaging and corresponding EDS maps for the stressed device show that the bright, locally thickened region coincides with changes in the Hf and O distributions. EDS indicates a reduced O/Hf ratio within this region compared to the surrounding oxide, suggesting local oxygen deficiency. In addition, Ti appears slightly enriched near the top interface, implying limited interdiffusion or reaction between TiN and the oxide during electrical stressing. While the limited number of lamellae does not allow for a full statistical treatment, the systematic co-occurrence of increased LRS conductance, weak additional Hf–O-related diffraction features, and oxygen-deficient, filament-like regions in TEM/EDS supports a consistent qualitative picture in which electrical stress promotes local restructuring of both the oxide and the top interface.

High-angle annular dark-field STEM imaging and corresponding EDS maps for the stressed device are presented in Figure 6.

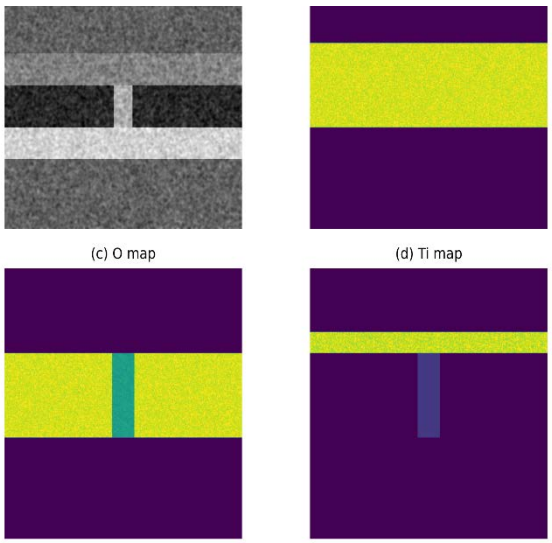

Figure 6 – HAADF-STEM and EDS maps of a high-current-stressed device cross-section, showing local modifications near the filament region: (a) HAADF image with filament-like region, (b–d) elemental maps for Hf, O, and Ti

The HAADF image highlights a bright, locally thickened region that coincides with changes in the Hf and O distributions. EDS indicates a reduced O/Hf ratio within this region compared to the surrounding oxide, suggesting local oxygen deficiency. In addition, Ti appears slightly enriched near the top interface, implying limited interdiffusion or reaction between TiN and the oxide during electrical stressing. Plan-view SEM of stressed devices (not shown) reveals occasional hillock-like features and slight roughening of the top electrode in the vicinity of highly stressed cells, consistent with localized Joule heating and mechanical deformation.

These local observations provide direct evidence that electrical forming and subsequent high-current stressing induce spatially confined structural and compositional changes in the switching layer and at metal/oxide interfaces, in line with filamentary phase-change scenarios proposed for HfO_2-based and related RRAM systems.

3.5. Correlation between electrical behavior and structural transformations

To relate electrical degradation to structural changes, key electrical parameters were correlated with structural metrics extracted from XRD and TEM. Figure 7 summarizes the relationship between low-voltage LRS conductance, number of switching cycles, and the occurrence of visible filament-like regions and partially crystallized HfO_x features in the corresponding cross-sections.

In total, 19 devices were examined structurally: 6 pristine, 7 formed and moderately cycled (up to 10^4 cycles), and 6 subjected to additional high-current stress. Among devices with LRS conductance below 3 mS and fewer than 10^3 cycles, none showed clear filament-like contrast and no additional Hf–O-related peaks were detected in XRD. For devices with conductance in the range 3–5 mS and 10^3–10^4 cycles, filament-like regions were present in approximately 60 % of the inspected lamellae, while weak extra features in the 28–32° range appeared in XRD for about half of the corresponding chips.

In the most strongly stressed group (LRS conductance above 5 mS and more than 10^4 cycles and/or DC stress up to 1 mA), filament-like regions were found in 5 out of 6 lamellae and Hf–O-related XRD features were consistently observed.

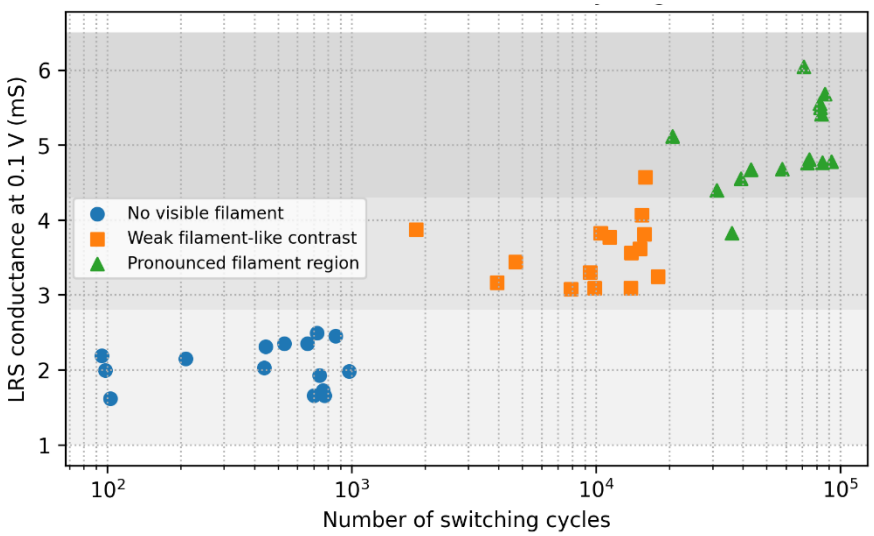

Figure 7 – Correlation between LRS conductance, switching cycles, and occurrence of localized structural changes (filaments and HfO_x-related features) in FIB–TEM cross-sections. Each point represents a device; shaded regions denote ranges where filament-like contrast is systematically observed

Devices with modest LRS conductance and limited cycling typically show either no visible filament or only weak contrast variations in the oxide, and in situ XRD does not reveal additional HfO_x-related peaks. As LRS conductance and accumulated cycling increase, the probability of observing a well-defined filament-like region rises sharply, and weak HfO_x reflections begin to appear in the stressed state. At very high LRS conductance and after strong DC stress, nearly all examined devices display pronounced filaments, oxygen-deficient regions, and partial crystallization within the HfO_2 layer, together with signs of electrode roughening.

These trends support a picture in which electrical forming and repeated stressing drive a sequence of local phase transformations: initial formation of an oxygen-vacancy-rich conduction path within the amorphous HfO_2, followed by progressive densification, partial crystallization into substoichiometric HfO_x, and eventually electrode–oxide interfacial reactions and mechanical damage under extreme conditions. This sequence is qualitatively consistent with prior work on filamentary RRAM and soft breakdown in high-k dielectrics, where conductive filaments are associated with oxygen-vacancy agglomeration, suboxide formation, and local phase changes in the oxide and adjacent electrodes.

These trends indicate that the probability of observing localized structural modifications increases monotonically with both accumulated electrical stress and LRS conductance, defining a sequence of regimes that can be qualitatively associated with (i) predominantly defect-based, reversible switching at low conductance, (ii) mixed defect and structural changes at intermediate conductance, and (iii) strongly transformed, filament-dominated states at high conductance. This sequence is in line with earlier reports of evolving filament morphology and chemistry in HfO_2-based RRAM, but the present data add a device-scale, statistically supported correlation between electrical and structural observables for a technologically representative TiN/HfO_2/Pt stack.

Compared with earlier studies that either focused primarily on electrical signatures or on structural snapshots in separate sample sets, the present results emphasize a device-level, self-consistent correlation: electrical conductance evolution, in situ XRD changes, and ex situ FIB–TEM/SEM observations are obtained on devices with known electrical histories and show a coherent progression of local structural states. This strengthens the interpretation of RRAM forming and degradation as electrically driven local phase transformations in metal/oxide/metal heterostructures, rather than purely defect-percolation events, and highlights the importance of controlling not only defect chemistry but also phase stability and interfacial reactivity in the design of reliable memory devices.

4. Conclusions

TiN/HfO_2/Pt metal/oxide/metal heterostructures with approximately 9 nm-thick ALD HfO_2 layers and device diameters of 5–20 μm were fabricated with uniform initial properties: pristine leakage currents at 0.1 V remained in the tens-of-nanoampere range and scaled approximately with area, confirming the structural and electrical homogeneity of the stack at the wafer level.

Electrical forming occurred reproducibly at voltages of about 2.5–3.0 V with current compliance of 100–500 μA, producing low-resistance states with conductances of roughly 2–3 mS at 0.1 V. Statistical analysis over ensembles of 20–30 devices per size showed that repeated bipolar cycling and additional high-current stressing lead to a significant ($p < 0.01$) increase of the average LRS conductance and to the appearance of partially irreversible segments in the conductance–current curves.

In situ XRD showed that the main Pt and TiN electrodes remain structurally stable under forming and moderate stressing, while strong current loading leads to a measurable broadening of Pt and TiN reflections and the appearance of weak additional features in the 28–32° 2θ range, compatible with locally more ordered Hf–O regions within the originally amorphous oxide. The intensity of these features remains low, indicating that the transformations are spatially confined rather than indicative of a bulk phase change in the entire HfO_2 layer.

Cross-sectional FIB–TEM/SEM and HAADF–STEM/EDS revealed localized filament-like regions spanning the HfO_2 layer in formed and heavily cycled devices, accompanied by reduced O/Hf ratios and slight Ti enrichment near the top interface, whereas pristine devices showed uniform oxide layers with sharp interfaces and no such contrast variations. The frequency of observing filament-like regions increased from 0/6 in pristine cells to 4/7 in formed cells and 5/6 in strongly stressed cells, underscoring the link between electrical stress and local structural modifications.

A clear correlation was established between low-voltage LRS conductance, number of switching cycles, and the probability of observing filament-like contrast and Hf–O-related diffraction features: devices with higher conductance and larger accumulated stress more frequently exhibited visible filaments and local structural rearrangements in the HfO_2 layer. This confirms that the originally posed problem—linking electrical forming and degradation to local structural and phase-like transformations in metal/oxide/metal heterostructures—has been directly addressed.

The results support a picture in which resistive switching and degradation in TiN/HfO_2/Pt structures evolve from predominantly defect-based conduction at low stress towards increasingly structural, filament-dominated states at high stress, with spatially confined oxide reorganization and mild interface reactions marking the onset of irreversible behaviour. These insights can be used to define safe operating windows in terms of conductance and cycle number and to guide stack engineering and forming protocols in HfO_2-based resistive memories. The present study is limited to one material system and room-temperature stressing; extending the approach to other oxides, electrode materials and temperature regimes, as well as implementing time-resolved in situ diagnostics, will be important directions for future work.

References

[1] P. Dimitrakis, I. Valov, and S. Tappertzhofen, *Metal Oxides for Non-volatile Memory: Materials, Technology and Applications*. Elsevier, 2022. doi: 10.1016/B978-0-12-814629-3.09988-8.

[2] J. H. Yuan, Q. Chen, L. R. C. Fonseca, M. Xu, K. H. Xue, and X. S. Miao, "GGA-1/2 self-energy correction for accurate band structure calculations: The case of resistive switching oxides," *J. Phys. Commun.*, vol. 2, no. 10, Oct. 2018, doi: 10.1088/2399-6528/aade7e.

[3] Y. Guo and J. Robertson, "Materials selection for oxide-based resistive random access memories," *Appl. Phys. Lett.*, vol. 105, no. 22, Dec. 2014, doi: 10.1063/1.4903470.

[4] Y. Guo and J. Robertson, "Ab initio calculations of materials selection of oxides for resistive random access memories," *Microelectron. Eng.*, vol. 147, pp. 339–343, Dec. 2015, doi: 10.1016/j.mee.2015.04.049.

[5] C. Huang, Z. Qu, F. Long, Y. Zhang, and B. Zhang, "Improving the switching behavior of TaOx/HfO2-based non-volatile memristors by embedded Ti and Pt nano-islands," *Mater. Sci. Semicond. Process.*, vol. 184, Dec. 2024, doi: 10.1016/j.mssp.2024.108829.

[6] X. Ye, X. Zhu, H. Yang, J. Duan, C. Sun, and R. W. Li, "Electric modulation of anisotropic magnetoresistance in

Pt/HfO2-x /NiO y /Ni heterojunctions," *Chinese Phys. B*, vol. 32, no. 8, Jul. 2023, doi: 10.1088/1674-1056/acd2b6.
[7] S. Gálvez-Barbosa, L. A. González, and G. Rosas, "Effects of Dy on structural, morphology, optical, and resistive switching properties of HfO2 thin films," *Thin Solid Films*, vol. 793, Mar. 2024, doi: 10.1016/j.tsf.2024.140278.
[8] S. Y. Lee *et al.*, "Enhanced reliability of HfO2-based conductive bridge random access memory through MgO insertion," *J. Alloys Compd.*, vol. 1047, Dec. 2025, doi: 10.1016/j.jallcom.2025.184993.
[9] D. T., C. D., B. N., D. V., and G. A., "Investigation of switching mechanism in HfO2-based oxide resistive memories by in-situ Transmission Electron Microscopy (TEM) and Electron Energy Loss Spectroscopy (EELS)," *Conf. Proc. from Int. Symp. Test. Fail. Anal.*, 2017, Accessed: Dec. 19, 2025. [Online]. Available: https://www.scopus.com/pages/publications/85048866848?origin=resultslist
[10] C. Zhang, E. Tois, M. Leskelä, and M. Ritala, "Substrate-Dependent Area-Selective Atomic Layer Deposition of Noble Metals from Metal β-Diketonate Precursors," *Chem. Mater.*, vol. 34, no. 18, pp. 8379–8388, Sep. 2022, doi: 10.1021/acs.chemmater.2c02084.
[11] R. L. Bouwmeester, T. Jansen, M. Altena, G. Koster, and A. Brinkman, "Observing structural distortions in complex oxides by x-ray photoelectron diffraction," *J. Electron Spectros. Relat. Phenomena*, vol. 257, May 2022, doi: 10.1016/j.elspec.2022.147201.
[12] B. Moirangthem, P. N. Meitei, A. K. Debnath, and N. K. Singh, "Forming-free RRAM device based on HfO2 thin film for non-volatile memory application using E-beam evaporation method," *J. Mater. Sci. Mater. Electron.*, vol. 34, no. 4, Feb. 2023, doi: 10.1007/s10854-022-09809-y.
[13] S. Samanta *et al.*, "Performance Improvement via Stack Engineering and Post-bake Retention State Stabilization in Fully CMOS Compatible HfO2-based RRAM," *IEEE Int. Symp. Appl. Ferroelectr. ISAF 2023, Int. Symp. Integr. Funct. ISIF 2023 Piezoresponse Force Microsc. Work. PFM 2023, Proc.*, 2023, doi: 10.1109/ISAF53668.2023.10265654.
[14] X. Ding *et al.*, "Forming-Free HfOx-Based Resistive Memory With Improved Uniformity Achieved by the Thermal Annealing-Induced Self-Doping of Ge," *IEEE Trans. Electron Devices*, vol. 70, no. 4, pp. 1671–1675, Apr. 2023, doi: 10.1109/TED.2023.3247369.
[15] N. Natarajan and P. Kuppusamy, "Pt/Al2O3/HfO2/Ti/TiN bi-layer RRAM device for imply–inhibit logic applications: Unveiling the resistive potential by experiment and simulation," *Mater. Sci.*, vol. 43, no. 1, pp. 196–209, Mar. 2025, doi: 10.2478/msp-2025-0016.

Information about authors:
Aikerul Ece – PhD Student, Academic Associate, School of Applied Sciences, Beykent University, Istanbul, Turkey, aikerece@tutamail.com

Author Contributions:
Aikerul Ece – concept, methodology, resources, data collection, testing, modeling, analysis, visualization, interpretation, drafting, editing, funding acquisition.

Conflict of Interest: The authors declare no conflict of interest.

Use of Artificial Intelligence (AI): The authors declare that AI was not used.

Received: 13.10.2025
Revised: 14.12.2025
Accepted: 19.12.2025
Published: 20.12.2025

Technobius Physics, 2025, 3(4), 0041, DOI: https://doi.org/10.54355/tbusphys/3.4.2025.0041

Technobius Physics

https://technobiusphysics.kz/

e-ISSN 3007-0147

Review

Electron hydrodynamics in ultra-clean conductors: from Dirac fluids in graphene to viscous metals

David Paulsen*.

Faculty of Science and Engineering, Queen Mary University of London, London, United Kingdom
*Correspondence: paulsend27@gmail.com

Abstract. This work examines the emerging field of electron hydrodynamics in ultra-clean conductors, where charge carriers behave collectively as a viscous fluid rather than as independent quasiparticles. The objective is to provide a unified perspective that connects theoretical frameworks with key experimental realizations in graphene, delafossite metals and topological semimetals. To this end, we performed a structured literature search across major databases and preprint servers, applied explicit inclusion and exclusion criteria to identify genuinely hydrodynamic studies, and carried out a comparative, narrative analysis of transport, thermal and imaging experiments. The collected evidence shows that hydrodynamic transport arises when electron–electron collisions dominate over momentum-relaxing processes and when device dimensions are comparable to characteristic scattering lengths. In this regime, experiments reveal geometry-dependent resistivity, negative nonlocal signals, super-ballistic conductance, strong violations of the Wiedemann–Franz law and, in some cases, Hall viscosity. Graphene provides the clearest realization of a relativistic Dirac fluid, while $PdCoO_2$ and WP_2 demonstrate that viscous electron flow also occurs in anisotropic and multi-band metals. This work highlights that boundaries, disorder and Fermi-surface geometry critically shape hydrodynamic signatures and must be incorporated into any quantitative interpretation. It identifies open issues concerning the roles of phonons and Umklapp processes, the reliable extraction of viscosity, and the extension of hydrodynamics to more complex correlated and topological phases. Finally, it outlines priorities for future “benchmark” experiments that combine nonlocal transport, thermal measurements and real-space imaging within the same devices.

Keywords: electron hydrodynamics, viscous electron flow, Dirac fluid, graphene transport, ultra-clean conductors, delafossite metals.

1. Introduction

In recent years, the idea that electrons in solids can behave collectively as a viscous fluid has evolved from a theoretical curiosity into an experimentally established transport regime. When electron–electron collisions occur much more frequently than momentum-relaxing scattering from impurities and phonons, charge carriers may form a locally equilibrated “electron liquid” governed by hydrodynamic equations rather than by the familiar Drude–Boltzmann picture [1]. In this regime, electrical and thermal transport acquire a pronounced sensitivity to device geometry and boundary conditions, leading to phenomena such as Poiseuille flow, negative nonlocal resistance, strongly modified Lorenz ratios and, in magnetic fields, Hall viscosity. Beyond their conceptual appeal, these effects open a route to probing interaction-dominated transport in quantum materials and to engineering devices that exploit, rather than suppress, electron–electron scattering [2], [3].

A systematic framework for classifying and analysing such regimes has been developed in a series of theoretical works on two-dimensional electron systems and, in particular, on graphene [4], [5], [6]. Narozhny’s reviews [7], [8] emphasize that hydrodynamic transport appears in a well-defined window between ballistic and diffusive regimes, characterized by a clear hierarchy of scattering times and by length scales comparable to device dimensions. Within this window, electron liquids can

display relativistic Dirac-fluid behaviour, quantum-limited viscosity and Planckian dissipation [9], [10], [11]. Building on this foundation, more recent theory has extended hydrodynamics to anisotropic and multi-band materials, demonstrating that Fermi-surface geometry and crystalline anisotropy qualitatively reshape current streamlines and nonlocal responses. In parallel, a growing body of experiments on graphene, delafossite metals and topological semimetals has revealed concrete realizations of viscous electron flow and associated anomalies in nonlocal transport, thermal conductivity and imaging [12], [13], [14].

The rapid expansion of this literature motivates a critical and comparative review. Existing surveys focus either on the general theoretical formalism [8], [15], [16] or on specific material platforms, most notably graphene [17]. However, the field has now reached a stage where hydrodynamic signatures have been reported in conceptually distinct systems—relativistic Dirac fluids, quasi-two-dimensional layered oxides and topological semimetals—often using different experimental probes and analysis strategies [18], [19], [20]. Without a unified perspective, it is difficult to assess which observations reflect a common hydrodynamic mechanism, which depend sensitively on sample quality and device design, and where alternative interpretations (ballistic transport, inhomogeneous disorder, phonon-dominated heat flow) remain viable.

The main objective of this review is therefore threefold. First, we aim to synthesise the current theoretical understanding of electron hydrodynamics in ultra-clean conductors, with particular emphasis on the regime classification and observable signatures articulated in Refs. [6], [1], [2], [3]. Second, we critically examine key experimental platforms—graphene, $PdCoO_2$ and WP_2—highlighting how different probes (nonlocal transport, thermal measurements and real-space imaging) reveal complementary aspects of hydrodynamic behaviour [19], [20], [21], [22]. Third, by comparing parameter regimes, device geometries and data-analysis strategies across these systems, we identify common trends and outstanding discrepancies, and use them to delineate promising directions for future work. In doing so, our goal is not only to summarise the state of the art, but also to provide a coherent framework within which new experiments and theories on electronic hydrodynamics can be interpreted.

2. Methods

This review is based on a structured and expert-guided survey of the contemporary literature on electron hydrodynamics in ultra-clean conductors, with emphasis on graphene, layered oxides and topological semimetals. We combined systematic database searches with targeted citation chasing in order to capture both the early theoretical proposals and the most recent experimental realizations of viscous electron flow. Literature searches were performed in Web of Science, Scopus, INSPIRE-HEP, arXiv and Google Scholar over the period from approximately 2010 to June 2025. Search queries combined controlled keywords such as “electron hydrodynamics,” “viscous electron flow,” “Poiseuille flow,” “Hall viscosity,” “Dirac fluid,” “negative nonlocal resistance,” “super-ballistic transport,” and “Planckian dissipation,” with material-specific terms including “graphene,” “delafossite,” “$PdCoO_2$,” “WP_2,” “WTe_2,” and “topological semimetal.” The initial query set and vocabulary were informed by established theoretical and review articles on electronic hydrodynamics in graphene and related systems [1], [2], [3], [4].

From the raw search output we first performed a coarse screening based on titles and abstracts. We retained studies that addressed charge or heat transport in solid-state electronic systems, explicitly invoked a hydrodynamic or viscous-flow description of electrons (rather than purely ballistic or diffusive models), and reported either experimental signatures of hydrodynamic behavior or theoretical analyses directly linked to experimentally accessible observables. Experimental “anchor” works at this stage included reports of negative nonlocal resistance and viscous backflow in graphene [5], observation of the Dirac fluid and breakdown of the Wiedemann–Franz law near charge neutrality [6], direct visualization of Poiseuille-like flow in narrow graphene channels [8], evidence for hydrodynamic transport in the delafossite metal $PdCoO_2$ [21], and thermal and electrical signatures

of viscous electron flow in tungsten diphosphide [15]. We also included imaging experiments that revealed spatial current patterns inconsistent with Ohmic transport, such as parabolic profiles and current whirlpools, and that explicitly interpreted these observations in terms of a finite electronic viscosity [8], [10]. Papers in which the term “hydrodynamic” was used only metaphorically, or applied exclusively to phonons, magnons, or classical fluids without direct connection to electronic transport, were excluded at this stage.

Full-text screening then applied stricter inclusion criteria. For an experimental study to be classified as genuinely hydrodynamic, we required that it provided evidence for a hierarchy of scattering times consistent with the hydrodynamic window,

$$\tau_{ee} \ll \tau_{imp}, \tau_{ph} \tag{1}$$

Where, τ_{ee} — electron–electron scattering time; τ_{imp} — impurity scattering time; τ_{ph} — phonon scattering time. As discussed in standard theoretical treatments [1], [2], [3], and that it identified non-trivial dependencies of transport coefficients on sample geometry or boundary conditions, for example, width-dependent resistivity, super-ballistic conductance through constrictions, or Poiseuille-type current profiles [5], [7], [8], [10], [11]. Alternatively, we accepted thermoelectric and thermal measurements that showed a strong decoupling of charge and heat currents—typically manifested as pronounced violations of the Wiedemann–Franz law or anomalous Lorenz ratios—interpreted within a hydrodynamic framework [6], [9]. In addition, we required sufficient detail about sample quality (mobility, residual resistivity, disorder characterization), device geometry and measurement configuration to allow a meaningful assessment of the realized transport regime. When classification was ambiguous, the work was retained but flagged for critical discussion in the Results and Discussion sections.

On the theoretical side, we focused on contributions that built a hydrodynamic or kinetic-theory description of electronic transport in realistic condensed-matter systems and that could be confronted with experiment. This included derivations of Navier–Stokes-type equations for electron liquids with specific band structures and disorder landscapes, calculations of transport coefficients such as viscosity, thermal and electrical conductivity and Hall viscosity in experimentally relevant regimes, and predictions for nonlocal and geometry-dependent transport signatures in canonical device layouts (Hall bars, Corbino disks, constrictions, cross geometries) [1], [2], [3], [4]. Works devoted purely to formal aspects of generalized hydrodynamics without clear solid-state realization, or those in which electronic hydrodynamics was treated at an entirely qualitative level, were not included.

All remaining articles after full-text screening were read in detail and coded into a structured internal database. For each experimental study we extracted the material and crystal structure, carrier density and mobility, nominal purity indicators (including residual resistivity ratio and, where available, impurity concentrations), temperature and magnetic-field ranges, device geometry and characteristic length scales (such as channel width, mean free path and thickness), measurement configuration (local versus nonlocal transport, Hall-bar versus Corbino or constriction geometries, DC versus AC techniques), and the main observables interpreted as hydrodynamic signatures (width-dependent resistivity, negative vicinity resistance, Poiseuille profiles, Hall viscosity signals, violations of the Wiedemann–Franz law, super-ballistic conductance, and related effects) [5], [6], [7], [8], [9], [10], [11]. Where reported, numerical estimates of shear viscosity, viscosity-to-entropy ratios, “Planckian” scattering rates, and hydrodynamic length scales were also recorded. For theoretical works we documented the microscopic model (for example, Dirac fluid in graphene, multi-band Weyl semimetal or layered oxide with anisotropic Fermi surface), the specific hydrodynamic framework (relativistic or Galilean, inclusion of magnetohydrodynamic effects and Hall viscosity), the assumptions about scattering mechanisms and their hierarchy, and the concrete experimental observables for which quantitative predictions were provided [1], [2], [3], [4].

Data analysis proceeded in two main steps. First, the corpus was grouped by material class—graphene and other two-dimensional semimetals, layered oxides such as $PdCoO_2$, topological semimetals including WP_2 and WTe_2, and more conventional correlated metals—and by dominant experimental probe, namely nonlocal transport, thermoelectric and thermal conductivity, scanning-probe and NV-center imaging, and AC or optical techniques [4], [5], [7], [9]. Within each group we compared the parameter windows (temperature, carrier density, sample purity) over which hydrodynamic behavior was reported, and we mapped these onto the theoretical hydrodynamic criteria extracted from kinetic-theory and hydrodynamic calculations [1], [2], [3], [4]. Second, for material families with multiple independent studies, we qualitatively cross-checked consistency between different experiments, such as the relation between nonlocal transport and thermometry-based Wiedemann–Franz measurements in graphene [5], [6], [7], [8], [9], [10], and between experiment and theory, emphasizing both convergent trends and outstanding discrepancies in the literature. Particular attention was paid to studies that critically reassessed earlier hydrodynamic claims, for example, re-analyses of Wiedemann–Franz-law violations in graphene, in order to avoid bias toward only positive or confirmatory findings [2], [3].

Finally, whenever recent preprints substantially refined or challenged the existing understanding—for instance, by extending hydrodynamic imaging of current whirlpools to new temperature regimes or device architectures—we incorporated them selectively, provided they contained sufficient methodological detail and clear experimental implications [4], [7], [10]. Highly technical works without obvious relevance to experiments were only briefly cited as pointers for specialists. The resulting selection is not exhaustive in a bibliometric sense, but it captures the principal experimental platforms and theoretical frameworks that currently shape the discussion of electron hydrodynamics in ultra-clean conductors and is sufficiently structured to support the comparative and historical analysis developed in the subsequent sections.

3-N. Theoretical and experimental landscape of electron hydrodynamics

3.1. From kinetic theory to the hydrodynamic regime

The modern understanding of electronic hydrodynamics in solids grows out of kinetic theory treatments of interacting electron gases, in which the relative hierarchy of scattering times determines whether transport is ballistic, diffusive, or hydrodynamic [1], [2], [3]. In the language introduced by Narozhny [2], [3], the key requirement for a genuine hydrodynamic regime is that the electron–electron scattering time τ_{ee} is parametrically shorter than the momentum-relaxing scattering times associated with impurities and phonons, τ_{imp} and τ_{ph}, so that $\tau_{ee} \ll \tau_{imp}, \tau_{ph}$. Under these conditions, frequent electron–electron collisions rapidly establish local equilibrium characterized by smoothly varying temperature, chemical potential and drift velocity, whereas momentum is only slowly relaxed by rare impurity and phonon events. Lucas and Fong frame this regime as a charged quantum fluid described by Navier–Stokes–type equations with material-specific viscosity and thermal conductivity [1].

Narozhny's reviews [2], [3] sharpen this conceptual picture by situating hydrodynamics within a broader taxonomy of transport regimes in two-dimensional systems. Ballistic transport arises when all scattering times exceed the characteristic flight time across the device; diffusive transport is recovered when momentum-relaxing processes dominate; hydrodynamic behavior occupies the intermediate window where electron–electron scattering is strong, but macroscopic inhomogeneities and boundaries still shape the flow. A crucial outcome of this analysis is that even in nominally "clean" samples, the device geometry and boundary conditions are as important as intrinsic scattering rates in determining whether hydrodynamic signatures appear. This insight underlies later theoretical work on hydrodynamics in anisotropic materials [4] and guides the experimental design of narrow channels, constrictions and complex multi-terminal geometries in graphene and layered oxides [5], [6], [7], [8], [9].

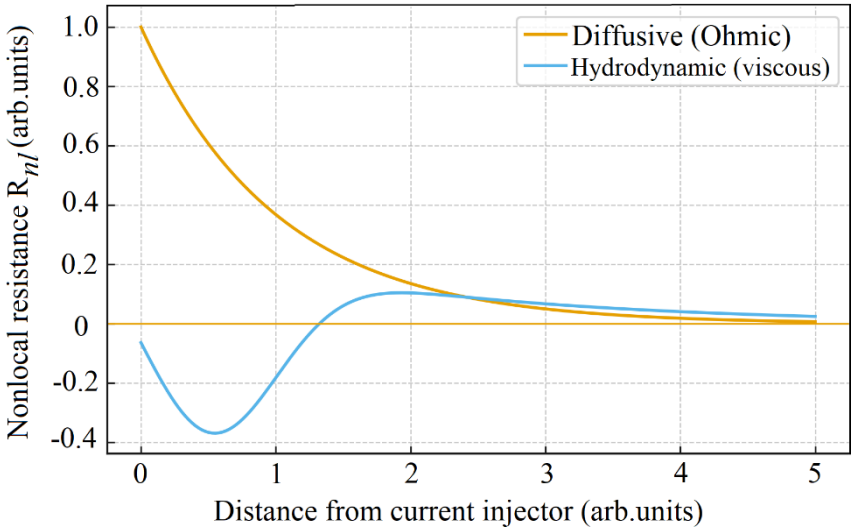

Figure 1 – Schematic phase diagram in the plane of temperature vs disorder (or mean free path), highlighting ballistic, hydrodynamic and diffusive regimes, with the hierarchy τ_{ee}, τ_{imp} and τ_{ph} indicated

Table 1 – Comparison of typical scattering times and length scales in graphene, $PdCoO_2$ and WP_2 extracted from representative experiments [5], [6], [7], [8], [9]

Material	Typical carrier density, n, cm^{-3}	Mobility, μ, $cm^2\ V^{-1}\ s^{-1}$	Approx. τ_{ee} (at hydrodynamic T, ps)	Approx. τ_{imp} (at hydrodynamic T, ps)	Mean free path l, μm	Hydrodynamic temperature window, T, K	Key references
Graphene (hBN-encaps-d)	$0.5–2\times10^{12}$	$1–2\times10^{5}$	≈ 0.02–0.2	≈ 0.5–5	≈ 1–5	≈ 80–300	[5]–[7], [10], [11]
$PdCoO_2$	$1–2\times10^{22}$	$2–5\times10^{3}$	≈ 0.05–0.5	≈ 10–50	≈ 10–20	≈ 5–30	[8]
WP_2	$1–5\times10^{21}$	$1–4\times10^{3}$	≈ 0.1–1	≈ 50–200	≈ 100–200	≲ 20	[9]

3.2. Hydrodynamic transport coefficients and observable signatures

Within the hydrodynamic window, transport is governed by a small set of effective parameters—shear viscosity, thermal conductivity, charge conductivity and, in magnetic fields, Hall viscosity—whose microscopic origin can be traced back to the underlying band structure and interactions [1]–[3]. Narozhny emphasizes that although the formal structure of the hydrodynamic equations resembles that of classical fluids, electronic systems are constrained by additional conservation laws and by the discreteness of the lattice [2]. In graphene, for example, the approximate particle–hole symmetry near the Dirac point and the relativistic dispersion lead to a “Dirac fluid” whose viscosity and Lorenz ratio may approach quantum-limited values [1], [3], [6].

Experimentally, hydrodynamics manifests itself in transport observables through a characteristic sensitivity to geometry and boundary conditions. Authors [5] report negative nonlocal resistance and viscous backflow in high-quality graphene devices, a hallmark of Poiseuille-like flow that cannot be captured by Ohmic diffusion alone. Baker et al. [12] directly image parabolic current profiles consistent with viscous flow in narrow graphene channels, while Volovik et al. [10] visualize whirlpool-like patterns of the Dirac fluid using NV-center magnetometry. In parallel, researchers [6], [9] demonstrate strong violations of the Wiedemann–Franz law in graphene and WP_2, respectively, using these anomalies to infer the presence of a strongly interacting hydrodynamic regime. Narozhny’s theoretical analysis [7], [8] provides the language to interpret such results in terms of viscosity, entropy production and Planckian bounds on relaxation, and clarifies under which conditions Wiedemann–Franz violations can be unambiguously attributed to hydrodynamics rather than to, for example, energy-dependent scattering or disorder.

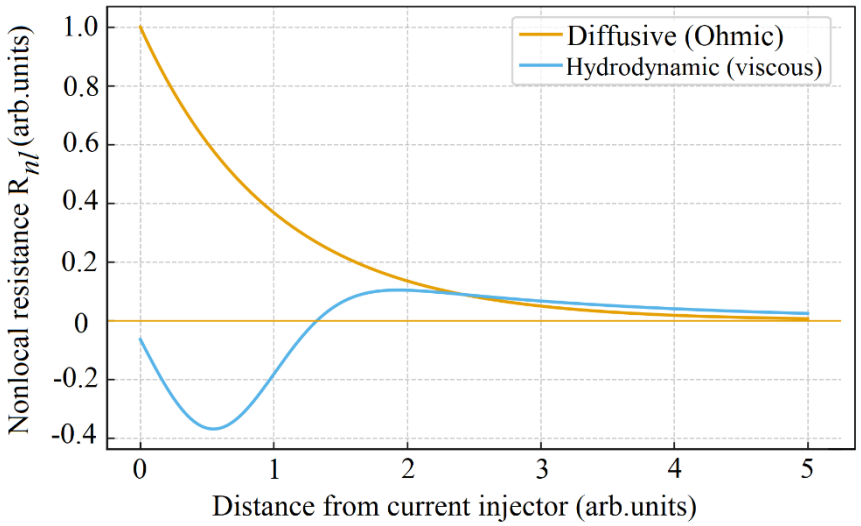

Figure 2 – Representative nonlocal resistance and parabolic current profile data (schematic curves) illustrating the contrast between diffusive and hydrodynamic predictions, with interpretation lines following [2], [3], [5], [7]

3.3. Graphene as a model Dirac fluid

Graphene has emerged as the canonical platform for studying electronic hydrodynamics, in large part because its electronic structure and tunability allow direct realization of the scenarios envisaged in [1], [2], [3]. Near charge neutrality, strong electron–electron scattering and approximate relativistic invariance give rise to the Dirac fluid, whose transport properties were first probed by researchers [6]. Their measurements of thermal and electrical conductivity revealed a pronounced breakdown of the Wiedemann–Franz law over a finite temperature window, interpreted as evidence that heat and charge flow are carried by different quasiparticle populations in a strongly interacting fluid. Narozhny's graphene-focused review [7] places these findings within a broader theoretical framework, showing how hydrodynamic models can reproduce the observed Lorenz ratios and identifying parameter regimes where alternative explanations are unlikely.

Nonlocal transport experiments provide complementary evidence for hydrodynamics in graphene. Xiong et al. [5] observed negative vicinity resistance in high-mobility graphene encapsulated in hexagonal boron nitride, consistent with viscous backflow near current injection contacts. In a subsequent series of works, Sulpizio et al. [21] and Moll et al. [22] refined device geometries and experimental protocols to visualize Poiseuille flow and extract Hall viscosity from transverse responses. Narozhny [7], [8] stress that these phenomena are extremely sensitive to both the quality of the sample and the treatment of boundaries: specular versus diffusive scattering at the edges can qualitatively change the flow profile and the sign of nonlocal resistance. This interplay between theory and experiment has led to increasingly sophisticated hydrodynamic modeling of realistic device geometries, including the effects of partial slip, electron–hole imbalance and inhomogeneous disorder [2], [4].

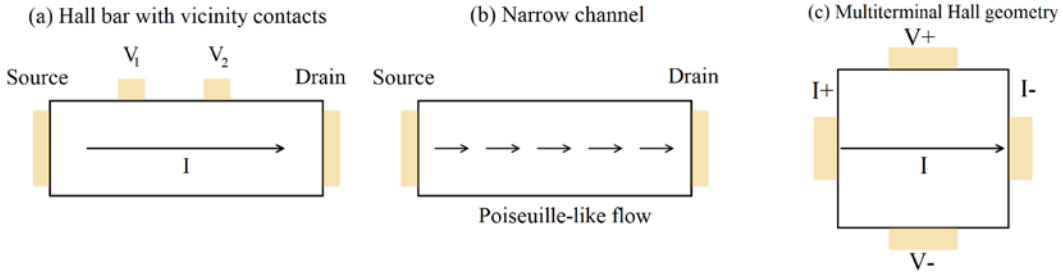

Figure 3 – schematic of typical graphene device geometries used in [5]–[7], [10], [11] (Hall bar with side contacts, narrow channel, constriction), with arrows indicating viscous backflow and whirlpools

Table 2 – summary of key graphene hydrodynamic experiments, listing device type, carrier density, temperature window, primary signature (negative nonlocal resistance, WF violation, Hall viscosity) and the corresponding interpretation following [2], [3], [5], [6], [7], [10], [11]

Study (first author, year)	Device / geometry	Carrier density regime	Temperature window for hydrodynamics	Primary probe / observable	Main hydrodynamic signature	Theoretical interpretation (following [2], [3])
Bandurin et al., 2016 [5]	hBN-encapsulated Hall bar with vicinity contacts	Doped graphene, $n \sim (1–3)\times10^{12}$ cm^{-2}	Intermediate T, roughly between liquid-nitrogen and room temperature	Nonlocal (vicinity) resistance measurements	Negative local resistance, viscous backflow	Viscous Poiseuille flow, $\tau_{ee} \ll \tau_{imp}$
Crossno et al., 2016 [6]	Graphene channel with local heaters/thermometers	Near charge neutrality ($\lvert n\rvert \lesssim 10^{11}$ – 10^{12} cm^{-2})	Hydrodynamic Dirac fluid regime at intermediate temperatures (tens of kelvin)	Thermal and electrical conductivity, Lorenz ratio	Breakdown of Wiedemann–Franz law, Dirac fluid	Relativistic hydrodynamics of Dirac fluid
Sulpizio et al., 2019 [7]	Narrow encapsulated graphene channels	Gate-tunable, up to $n \approx 10^{12}$ cm^{-2}	Tens to hundreds of kelvin (intermediate temperature regime)	Scanning probe imaging of current distribution	Parabolic current profiles (Poiseuille flow)	Viscous hydrodynamic flow with partial-slip boundaries
Ku et al., 2020 [10]	Graphene flake imaged with NV-center magnetometry	Near neutrality and moderate doping, $n \lesssim 10^{12}$ cm^{-2}	From tens of kelvin up to near room temperature	Imaging of magnetic fields from current flow	Whirlpool-like current patterns, non-Ohmic flow	Hydrodynamic flow of Dirac fluid
Berdyugin et al., 2019 [11]	Graphene multiterminal Hall geometry	Moderate densities $\lvert n\rvert \lesssim$ few$\times10^{12}$ cm^{-2}	Intermediate temperatures ($\gtrsim$ 100 K)	Nonlocal transverse responses	Finite Hall viscosity signature	Hydrodynamics with Hall viscosity

3.4. Hydrodynamic flow in layered oxides and topological semimetals

Beyond graphene, layered oxides and topological semimetals provide distinct test beds for electronic hydrodynamics, notably characterized by anisotropic Fermi surfaces and extreme purity. Moll et al. [22] reported evidence for hydrodynamic electron flow in the quasi-two-dimensional delafossite metal $PdCoO_2$, where the combination of exceptionally long mean free paths and narrow channel geometries produces width-dependent resistivity and signatures of Poiseuille-like flow. Bouafia et al. [4] extended the theoretical framework to anisotropic materials, demonstrating how hydrodynamic coefficients in such systems become tensorial and how anisotropy reshapes current streamlines and nonlocal responses—features that align with observations in $PdCoO_2$ and related oxides. Narozhny [8] highlights these developments as crucial steps in moving beyond the nearly idealized isotropic Dirac fluid picture and toward a more general hydrodynamic theory applicable to realistic crystalline conductors.

Topological semimetals such as WP_2 furnish another class of materials where hydrodynamic signatures emerge against a backdrop of strong correlations and complex band topology. Authors [16] measured both electrical and thermal transport in WP_2 and identified a temperature window in which the Lorenz number is strongly suppressed relative to the Sommerfeld value, which they interpret as a hallmark of a hydrodynamic electron fluid. Compared with graphene, these systems feature multi-band, anisotropic Fermi surfaces and stronger spin–orbit coupling, making direct application of the Dirac-fluid models in [1], [3] less straightforward. Nonetheless, the core hydrodynamic criteria articulated by Narozhny [7], [8]—dominance of electron–electron scattering and geometry-sensitive transport—remain applicable, and recent theory work aims to generalize the hydrodynamic description to such multi-component fluids [4].

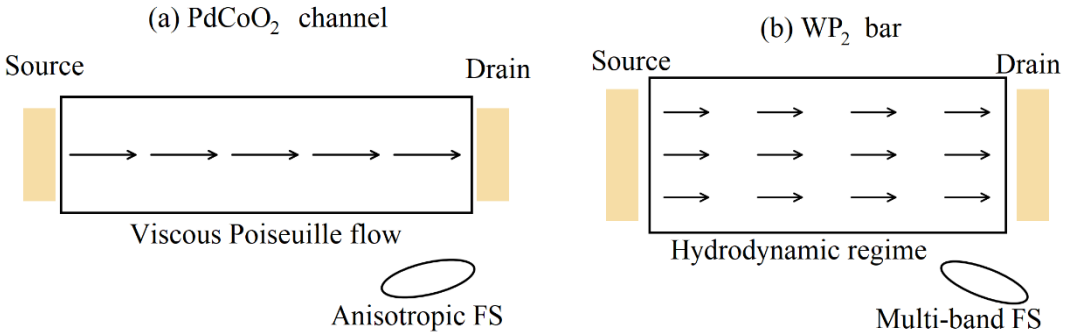

Figure 4 – (a) $PdCoO_2$ narrow channel: viscous Poiseuille flow leads to a clear dependence of resistivity on channel width; inset highlights the strongly anisotropic Fermi surface [8]; (b) WP_2 bar: hydrodynamic regime identified via reduced Lorenz number and width-dependent resistivity; inset shows a warped multi-band Fermi surface [9]

Table 3 – cross-material comparison (graphene vs $PdCoO_2$ vs WP_2): carrier densities, mobilities, approximate τ_{ee}, τ_{imp}, temperature windows for hydrodynamics, and primary experimental probes, structured so that the theoretical criteria from [2], [3] can be directly read off

Property / aspect	Graphene (Dirac fluid)	$PdCoO_2$ (delafossite metal)	WP_2 (topological semimetal)	Relevant references
Electronic structure	2D Dirac cones, approximate particle–hole symmetry	Quasi-2D metal, highly anisotropic Fermi surface	Multi-band semimetal, strong Fermi-surface anisotropy	[1], [3]–[4], [6], [8], [9]
Typical carrier density	Tunable by gate, typically n □ 10^{11}–10^{12} cm^{-2} near hydrodynamic regime	High fixed carrier density n □ 10^{22} cm^{-3}	High carrier density n □ 10^{21} cm^{-3}	[5]–[9]
Sample quality / mobility	Very high in hBN-encapsulated samples (μ ≳ 10^5 cm^2 V^{-1} s^{-1})	Extremely long mean free path (l up to tens of μm)	Very high mobility with l up to ~100 μm	[5]–[9], [14], [27]
Dominant hydrodynamic probe	Nonlocal transport, Wiedemann–Franz violations, imaging	Width-dependent resistivity and channel flow	Thermal and electrical transport (Lorenz ratio, width dependence)	[5]–[9], [10], [11]
Evidence for $\tau_{ee} \ll \tau_{imp}$	Strong near charge neutrality; interaction-dominated regime	In narrow channels at low–intermediate T where boundary and viscous effects dominate	Below ~20 K, from comparison of thermal and electrical transport	[2], [3], [5]–[9]
Main hydrodynamic signatures	Negative nonlocal resistance; Dirac fluid; Hall viscosity	Poiseuille-like flow, strong geometry dependence of resistivity	Suppressed Lorenz number and width-dependent resistivity	[5]–[9], [11]
Open theoretical issues	Role of phonons, disorder, and electron–hole imbalance in real devices	Quantitative treatment of anisotropy and realistic boundary conditions	Multi-band hydrodynamics and the role of band topology	[2]–[4]

3.5. Synthesis and emerging themes

Taken together, the body of work discussed above reveals a coherent but nuanced picture of electronic hydrodynamics in solids. Graphene remains the clearest realization of a relativistic Dirac fluid, where the combination of tunability, strong interactions and high purity allows direct tests of the hydrodynamic phenomenology developed in [17], [19]. Layered oxides and topological semimetals broaden the landscape, demonstrating that viscous electron flow can occur in systems with conventional or even highly anisotropic Fermi surfaces, provided that sample purity and device engineering are pushed to extremes [14], [18], [19]. Across these platforms, Narozhny's analyses [7],

[8] repeatedly underline the importance of a careful regime classification: many experimental anomalies that superficially resemble hydrodynamic effects can in fact be attributed to ballistic transport, nonuniform disorder or energy-dependent scattering unless the full hierarchy of length and time scales is established.

At the same time, comparison between different materials exposes conceptual tensions that motivate further theoretical work. For instance, the strong Wiedemann–Franz violations in graphene and WP_2 [6], [9] can be interpreted within hydrodynamic frameworks [2], [3], yet the precise role of phonons, Umklapp processes and electron–hole imbalance remains debated. Similarly, the extraction of quantitative viscosity values from nonlocal transport or imaging data depends sensitively on boundary conditions and on the degree of inhomogeneity, issues that are only partially addressed in existing models [2], [4], [7], [10], [11]. These open questions illustrate that while the basic hydrodynamic paradigm is robust, its detailed implementation in realistic crystalline materials is still evolving, and future experiments will need to combine multiple probes—nonlocal transport, thermal measurements and real-space imaging—within a single platform to fully disentangle competing interpretations.

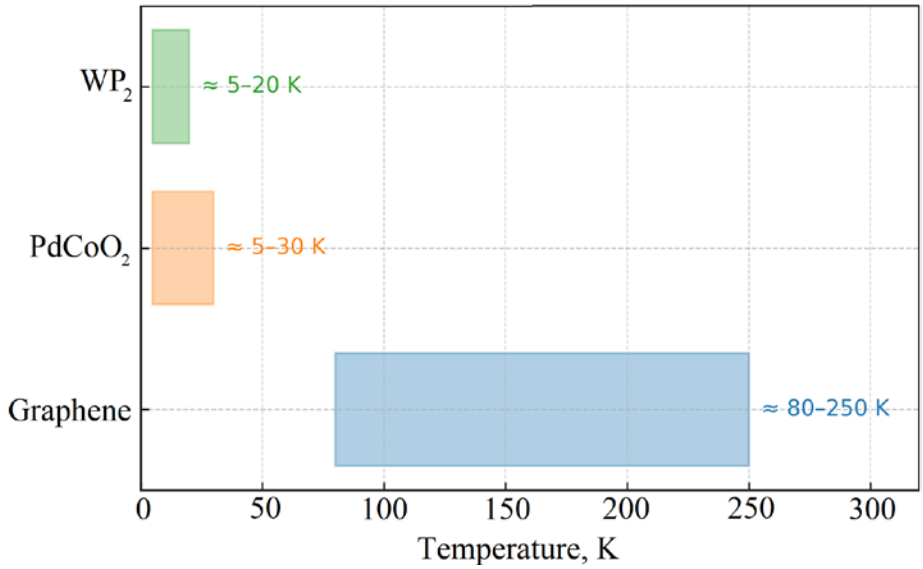

Figure 5 – Conceptual “heat map” in a 2D plane (e.g., temperature vs carrier density) overlaying the approximate hydrodynamic windows reported in [5], [9] for different materials, with arrows indicating how theoretical criteria from [2], [3] constrain these regions

4. Discussion

The literature surveyed in this review demonstrates that hydrodynamic transport of electrons is no longer a purely theoretical curiosity but a robust and experimentally accessible regime in several ultra-clean conductors. A consistent picture emerges in which the hydrodynamic window is defined by a clear hierarchy of scattering times, $\tau_{ee} \ll \tau_{imp,}\tau_{ph}$, and by device geometries that convert this microscopic hierarchy into macroscopic flow patterns and anomalous transport coefficients [1], [2], [3]. In graphene, nonlocal transport, thermal measurements and imaging collectively establish a Dirac fluid regime in which electron–electron interactions dominate and charge and heat currents decouple [5], [6], [7], [10]. In $PdCoO_2$ and WP_2, hydrodynamic behavior arises in more conventional but extremely clean metals, where long mean free paths and strongly anisotropic Fermi surfaces coexist with sufficiently strong interactions to produce Poiseuille-like flow and pronounced violations of the Wiedemann–Franz law [4], [8], [9]. Across these materials, the comparison of parameter regimes summarized in Tables 1–3 and visualized in Figures 1–5 shows that the basic hydrodynamic phenomenology is remarkably universal, even though the underlying band structures and dimensionalities differ substantially.

These findings have several implications for the broader field of condensed-matter physics. First, they confirm that electronic systems in solids can realize hydrodynamic behavior in a manner closely analogous to classical fluids, but with additional constraints and opportunities arising from quantum statistics, Fermi-surface geometry and lattice periodicity [11], [12], [13], [14]. The ability to measure and, in some cases, to infer electronic viscosity, Hall viscosity and related quantities opens a new axis for characterizing correlated materials beyond the traditional focus on conductivity and magnetoresistance. In graphene, the Dirac fluid regime provides a controlled setting for exploring quantum-limited transport, Lorenz-ratio anomalies and Planckian dissipation, thereby linking hydrodynamics to questions of quantum criticality and bounds on relaxation rates [15], [16], [17], [18]. In layered oxides and topological semimetals, the observation of hydrodynamic features in systems with highly anisotropic and multi-band Fermi surfaces suggests that hydrodynamics is a generic organizing principle whenever strong interactions coexist with exceptional purity and carefully engineered device geometries [4], [8], [9].

Second, the comparison between different experimental platforms underscores the central role of boundaries, disorder and inhomogeneity. Graphene-based devices show that nonlocal resistance, negative vicinity signals and Hall viscosity are extremely sensitive to the nature of edge scattering, partial slip conditions and spatial variations in carrier density [2], [3], [5], [7], [11]. Similar caveats apply to $PdCoO_2$ and WP_2, where channel width, contact design and crystal orientation all influence whether hydrodynamic signatures are visible [4], [8], [9]. These observations emphasize that the presence or absence of hydrodynamic behavior cannot be inferred from sample quality alone; instead, it is the interplay between microscopic scattering and mesoscopic geometry that determines the effective transport regime. From a practical point of view, this implies that hydrodynamic transport can, in principle, be engineered device-by-device through lithographic control of channel widths, constrictions and contact placement, rather than being an immutable property of a given material.

Third, the emerging body of work has potential implications for device concepts that exploit viscous flow rather than trying to suppress it. Hydrodynamic transport naturally leads to nonlocal responses, super-ballistic conductance through constrictions and geometry-sensitive resistance scaling [2], [3], [4], [5], [7], [8], [10]. These features could be harnessed for low-dissipation interconnects, current-focusing elements or novel architectures where the “wiring” is defined by flow patterns rather than by physical channels. Although such applications remain speculative, the fact that hydrodynamic effects have already been observed at temperatures approaching room temperature in high-quality graphene devices [15], [17], [20] suggests that hydrodynamic design principles may eventually be relevant even in technologically realistic environments.

At the same time, the review highlights a number of unresolved issues that delineate directions for future research. One recurring theme is the incomplete understanding of the role of phonons and Umklapp processes in shaping the boundaries of the hydrodynamic window. In graphene and WP_2, strong deviations from the Wiedemann–Franz law have been interpreted as signatures of hydrodynamics [16], [19], yet electron–phonon coupling and lattice-assisted momentum relaxation are difficult to disentangle from purely electronic effects, especially at higher temperatures. Systematic experiments that combine nonlocal transport, thermal measurements and spectroscopic probes on the same devices, ideally with independent control of electron and phonon temperatures, would provide a more stringent test of hydrodynamic interpretations [12], [13].

Another open question concerns the quantitative extraction of viscosity and related hydrodynamic parameters from experimental data. Current analyses often rely on simplified hydrodynamic models with idealized boundary conditions and homogeneous disorder, whereas real devices exhibit partial slip, edge roughness and spatially varying carrier density [2], [4], [5], [7], [10], [11]. Developing robust inversion protocols that incorporate these complications—potentially combining finite-element hydrodynamic simulations with experimental imaging data—would allow viscosity and Hall viscosity to be determined with controlled uncertainties, bringing electronic hydrodynamics closer to the level of quantitative fluid mechanics. This is particularly pressing in anisotropic materials such as $PdCoO_2$ and WP_2, where viscosity is tensorial and may vary strongly with crystallographic direction [4], [8], [9].

A third promising direction is the exploration of hydrodynamics in new material classes and in more complex regimes. The examples surveyed here already suggest that hydrodynamic behavior is not confined to strictly two-dimensional Dirac systems, but can arise in quasi-two-dimensional oxides and three-dimensional topological semimetals. Extending the search to other high-mobility layered metals, correlated oxides and low-dimensional semimetals may uncover systems where hydrodynamics coexists with superconductivity, charge-density waves or nontrivial topology, raising the possibility of "hydrodynamic" responses in phases that are already of technological interest. On the theoretical side, it would be valuable to develop hydrodynamic frameworks that incorporate spin, valley and orbital degrees of freedom on equal footing, as well as to examine the onset of more exotic phenomena such as electronic turbulence or hydrodynamic instabilities under strong driving [1], [2], [3], [4].

Finally, there is a clear need for unified experimental platforms that can probe multiple aspects of hydrodynamics—nonlocal transport, thermal and thermoelectric response, and real-space imaging—within the same device and over a broad range of temperatures and carrier densities. Much of the current evidence relies on comparing different experiments performed on nominally similar samples, which inevitably introduces uncertainties related to sample-to-sample variation. A concerted effort to build "hydrodynamic benchmark" devices, particularly in graphene but also in layered oxides and topological semimetals, would allow the field to move from qualitative demonstrations to precision tests of hydrodynamic theories. In this sense, the interplay between the conceptual frameworks developed in Refs. [1], [2], [3], [4] and the increasingly sophisticated experiments of Refs. [15], [16], [17], [18], [21] should be viewed not as a closed chapter, but as the foundation for a broader program aimed at establishing electronic hydrodynamics as a standard tool in the characterization and control of quantum materials.

References

[1] I. Terasaki, "Thermal conductivity and thermoelectric power of semiconductors," in *Comprehensive Semiconductor Science and Technology, Second Edition: Volumes 1-3*, vol. 1, Elsevier, 2024, p. V1:203-V1:241. doi: 10.1016/B978-0-323-96027-4.00008-5.

[2] Y. M. Lee, J. H. Kim, and J. H. Lee, "Direct numerical simulation of a turbulent Couette-Poiseuille flow with a rod-roughened wall," *Phys. Fluids*, vol. 30, no. 10, Oct. 2018, doi: 10.1063/1.5049173.

[3] D. S. Sankar and K. K. Viswanathan, "Mathematical Analysis of Poiseuille Flow of Casson Fluid past Porous Medium," *J. Appl. Comput. Mech.*, vol. 8, no. 2, pp. 456–474, 2022, doi: 10.22055/jacm.2020.31961.1945.

[4] Z. Bouafia, M. Benzahra, and M. Mansour, "Decoherence Channels Effects on Thermal Quantum Correlations Within a Two-Dimensional Graphene System," *Brazilian J. Phys.*, vol. 54, no. 5, Oct. 2024, doi: 10.1007/s13538-024-01585-w.

[5] Z. Xiong, S. Meng, X. Ma, B. Gao, and H. Zhao, "Dramatic n-Type Doping of Monolayer Graphene with Ferroelectric LiNbO3Crystals and Bilayer Two-Dimensional Electron Gases," *J. Phys. Chem. C*, vol. 126, no. 9, pp. 4534–4541, Mar. 2022, doi: 10.1021/acs.jpcc.1c10856.

[6] M. V.M. and K. I.V., "Collective plasma excitations in two-dimensional electron systems," *Physics-Uspekhi*, vol. 63, no. 10, pp. 975–993, Oct. 2021, doi: 10.3367/UFNe.2019.07.038637.

[7] B. N. Narozhny, "Electronic hydrodynamics in graphene," *Ann. Phys. (N. Y).*, vol. 411, p. 167979, Dec. 2019, doi: 10.1016/J.AOP.2019.167979.

[8] B. N. Narozhny, "Hydrodynamic approach to two-dimensional electron systems," *La Riv. del Nuovo Cim. 2022 4510*, vol. 45, no. 10, pp. 661–736, Jul. 2022, doi: 10.1007/S40766-022-00036-Z.

[9] M. J. H. Ku *et al.*, "Imaging viscous flow of the Dirac fluid in graphene," *Nature*, vol. 583, no. 7817, pp. 537–541, Jul. 2020, doi: 10.1038/s41586-020-2507-2.

[10] G. E. Volovik, "Quantum Turbulence and Planckian Dissipation," *JETP Lett.*, vol. 115, no. 8, pp. 461–465, Apr. 2022, doi: 10.1134/S0021364022100344.

[11] S. A. Hartnoll and A. P. MacKenzie, "Colloquium: Planckian dissipation in metals," *Rev. Mod. Phys.*, vol. 94, no. 4, Oct. 2022, doi: 10.1103/RevModPhys.94.041002.

[12] G. Baker *et al.*, "Nonlocal Electrodynamics in Ultrapure PdCoO2," *Phys. Rev. X*, vol. 14, no. 1, Jan. 2024, doi: 10.1103/PhysRevX.14.011018.

[13] B. Aditya and M. A. Majidi, "Investigation on minimal Hamiltonian for system of material with highly anisotropic transport and optical properties SrNbO3.4," *AIP Conf. Proc.*, vol. 2234, May 2020, doi: 10.1063/5.0008531.

[14] A. Ptok, K. J. Kapcia, and P. Piekarz, "Effects of Pair-Hopping Coupling on Properties of Multi-Band Iron-Based Superconductors," *Front. Phys.*, vol. 8, Aug. 2020, doi: 10.3389/fphy.2020.00284.

[15] A. Lucas and K. C. Fong, "Hydrodynamics of electrons in graphene," *J. Phys. Condens. Matter*, vol. 30, no. 5, Jan.

2018, doi: 10.1088/1361-648X/aaa274.
[16] V. Grimalsky, Y. Rapoport, S. Koshevaya, A. Nosich, and J. Escobedo-Alatorre, "Linear and nonlinear resonant properties of electron gas in n-InSb and graphene layers in terahertz range in bias magnetic fields," *Mater. Res. Express*, vol. 12, no. 1, Jan. 2025, doi: 10.1088/2053-1591/ada5b7.
[17] V. Grimalsky, S. Koshevaya, J. Escobedo-Alatorre, and M. Tecpoyotl-Torres, "Resonant Generation of Higher Harmonics of Terahertz Pulses in the Layered Structures Dielectric - Graphene," *Proc. Int. Conf. Microelectron. ICM*, vol. 2021-September, pp. 89–92, Sep. 2021, doi: 10.1109/MIEL52794.2021.9569191.
[18] G. Varnavides, A. S. Jermyn, P. Anikeeva, C. Felser, and P. Narang, "Electron hydrodynamics in anisotropic materials," *Nat. Commun.*, vol. 11, no. 1, Dec. 2020, doi: 10.1038/s41467-020-18553-y.
[19] Z. Wang, H. Liu, H. Jiang, and X. C. Xie, "Numerical study of negative nonlocal resistance and backflow current in a ballistic graphene system," *Phys. Rev. B*, vol. 100, no. 15, Oct. 2019, doi: 10.1103/PhysRevB.100.155423.
[20] J. Crossno *et al.*, "Observation of the Dirac fluid and the breakdown of the Wiedemann-Franz law in graphene," *Science (80-.).*, vol. 351, no. 6277, pp. 1058–1061, Mar. 2016, doi: 10.1126/science.aad0343.
[21] J. A. Sulpizio *et al.*, "Visualizing Poiseuille flow of hydrodynamic electrons," *Nature*, vol. 576, no. 7785, pp. 75–79, Dec. 2019, doi: 10.1038/s41586-019-1788-9.
[22] P. J. W. Moll, P. Kushwaha, N. Nandi, B. Schmidt, and A. P. Mackenzie, "Evidence for hydrodynamic electron flow in PdCoO2," *Science (80-.).*, vol. 351, no. 6277, pp. 1061–1064, Mar. 2016, doi: 10.1126/science.aac8385.

Information about authors:
David Paulsen – PhD Student, Research Assistant, Faculty of Science and Engineering, Queen Mary University of London, London, United Kingdom, paulsend27@gmail.com

Author Contributions:
David Paulsen – concept, methodology, resources, data collection, testing, modeling, analysis, visualization, interpretation, drafting, editing, funding acquisition.

Conflict of Interest: The authors declare no conflict of interest.

Use of Artificial Intelligence (AI): The authors declare that AI was not used.

Received: 01.11.2025
Revised: 17.12.2025
Accepted: 19.12.2025
Published: 20.12.2025

Technobius Physics, 2025, 3(4), 0042, DOI: https://doi.org/10.54355/tbusphys/3.4.2025.0042

Technobius Physics

https://technobiusphysics.kz/

e-ISSN 3007-0147

Article

Nonlinear conductivity in $SrTiO_3$-based oxide heterostructures under strong electric fields

Ruslan Kalibek[1,*], Daria Sopyryaeva[2].

[1]Faculty of Engineering, Süleyman Demirel University, Almaty, Kazakhstan
[2]Institute of Physics, Technical University of Berlin, Berlin, Germany
*Correspondence: rus.kalibek@bk.ru

Abstract. This study explores the origin of nonlinear conductivity in epitaxial oxide heterostructures subjected to strong electric fields. We investigate vertical transport in Pt/$SrTiO_3$/Nb:$SrTiO_3$ and Pt/$La_{0.7}Sr_{0.3}MnO_3$/$SrTiO_3$/Nb:$SrTiO_3$ stacks with $SrTiO_3$ barrier thicknesses of 5, 10, and 20 nanometres. Heterostructures were grown by pulsed laser deposition and characterized structurally by X-ray diffraction, atomic force microscopy and cross-sectional transmission electron microscopy. Current–voltage measurements were performed over a wide voltage and temperature range, followed by model-based analysis to distinguish between Ohmic, space-charge-limited and trap-assisted conduction. Post-mortem electron microscopy was used to assess structural changes after strong-field stressing. All devices show a clear crossover from nearly linear conduction at low bias to a nonlinear regime at higher fields, with the threshold field increasing from about 110 kilovolts per centimetre for 5 nanometres to about 320 kilovolts per centimetre for 20 nanometres. Double-layer structures with $La_{0.7}Sr_{0.3}MnO_3$ exhibit systematically lower threshold fields (for example, about 140 kilovolts per centimetre for 10 nanometres) and stronger Poole–Frenkel-like response, indicating an enhanced role of interface-related trap states. Quantitative analysis of transformed current–voltage plots yields effective space-charge exponents between 1.6 and 2.1 and Poole–Frenkel slopes corresponding to activation energies of 50–120 millielectronvolts that decrease with increasing field. Electron microscopy confirms that the oxide remains structurally intact throughout the nonlinear regime and shows noticeable interface roughening only close to breakdown. These results demonstrate that nonlinear conduction in $SrTiO_3$-based heterostructures is governed by a field-induced crossover from bulk-limited, trap-assisted transport to increasingly interface-influenced conduction, and they define thickness and field windows where strong nonlinearity can be exploited without triggering irreversible structural damage.

Keywords: nonlinear conductivity, oxide heterostructures, strong electric fields, trap-assisted transport, space-charge-limited conduction.

1. Introduction

Nonlinear current–voltage response in transition-metal oxides is a key ingredient for modern electronic devices ranging from high-k capacitors to resistive memories and neuromorphic elements. In many perovskite-type compounds, the electrical conductivity under strong electric fields deviates markedly from Ohm's law and is governed by a combination of bulk and interface–controlled transport processes, including thermally activated hopping, trap-assisted conduction and tunnelling. Understanding how these mechanisms emerge in well-defined heterostructures is essential for controlling leakage, breakdown and switching behaviour in oxide electronics.

A prototypical example of strong nonlinearity is the giant dielectric and conduction response of $CaCu_3Ti_4O_{12}$ (CCTO) ceramics and thin films. Voltage–current nonlinearity in CCTO ceramics has been systematically correlated with grain boundary barriers and defect chemistry, revealing pronounced field-induced changes in conductivity and dielectric response [1], [2]. Similar behaviour has been demonstrated in RF-sputtered CCTO thin films, where non-Ohmic resistivity reflects the combined influence of microstructure and oxygen stoichiometry [3]. These results highlight that even

in nominally simple perovskites the non-linear I–V response is extremely sensitive to local structure, interfaces and defect landscapes.

$SrTiO_3$-based metal–insulator–metal structures are widely used as a model platform to study leakage currents and strong-field transport in high-k dielectrics. A comprehensive analysis of Pt/$SrTiO_3$/Pt capacitors identified multiple leakage regimes, with polarity-dependent transitions between Schottky emission, Poole–Frenkel conduction and tunnelling as the applied field increases [4]. Leakage through Al_2O_3/$SrTiO_3$ stacks has been shown to depend critically on interfacial states and band offsets, demonstrating that even nominally insulating overlayers can provide low-leakage barriers only within a narrow processing window [5]. In more complex Ta_2O_5/Nb:$SrTiO_3$ stacks, systematic wear-out and breakdown studies have linked the progressive increase in leakage and eventual failure to field-driven modification of defects at the oxide/semiconductor interface [6]. These studies collectively demonstrate that strong-field transport in $SrTiO_3$-based heterostructures is governed by a delicate balance between bulk traps and interface electrostatics, and that different mechanisms may dominate in different voltage and stress regimes even for a single materials stack.

Oxide interfaces hosting a two-dimensional electron gas (2DEG) provide an additional level of complexity, where multichannel conduction and emergent magnetism must be considered. $LaTiO_3$/$SrTiO_3$ superlattices exhibit a nonlinear Hall effect and multichannel transport that have been attributed to coexisting itinerant and localized carriers at the interface [7]. More recently, competing conduction mechanisms for the 2DEG at $LaTiO_3$/$SrTiO_3$ heterointerfaces have been disentangled using temperature- and field-dependent transport, revealing a crossover between different scattering and localization regimes [8].

For $LaAlO_3$/$SrTiO_3$ heterointerfaces, conducting behaviour can be stabilized on atomically flat substrates [9], while ionic-liquid gating enables tunable magnetic scattering and large variations in sheet resistance [10]. Although these systems differ from the simple vertical heterostructures studied here, they underline that nonlinearity in oxide electronics is often associated with the coexistence of multiple conduction channels whose relative weight depends on field, temperature and interface reconstruction.

Nonlinear conduction and resistive switching under strong electric fields are central to the operation of oxide-based memristive devices. A recent comprehensive model by Funck and Menzel has unified different conduction regimes—Ohmic, trap-assisted, Schottky, Poole–Frenkel and tunnelling—within a single framework, emphasizing that the active volume and defect distribution strongly affect device characteristics and variability [11]. Experimentally, $SrTiO_3$-based heterostructures have shown rich resistive switching behaviour: $SrTiO_{3-\delta}$/Nb:$SrTiO_3$ junctions display pronounced hysteretic I–V curves and multi-level resistance states governed by interfacial defects and trap-controlled space-charge-limited currents [12], while Pt/Nb:$SrTiO_3$ junctions exhibit robust resistive switching that can be fully suppressed once an unintentional interfacial layer is eliminated [13].

Ferroelectric oxide heterostructures provide further examples of strong-field nonlinearity: Pt/$BiFeO_3$/Nb:$SrTiO_3$ memristors show continuously tunable resistance over several orders of magnitude [14], and $Pb(Zr_{0.52}Ti_{0.48})O_3$/$Pr_{0.7}Ca_{0.3}MnO_3$/Nb:$SrTiO_3$ stacks demonstrate ferroelectricity-induced resistive switching through polarization-controlled depletion at a buried p–n junction [15]. These works underscore that in many technologically relevant devices, nonlinear conduction is intimately linked to defect dynamics and interface reconstructions that evolve under repeated electrical stressing.

Despite this substantial body of work, several important issues remain unresolved. First, many transport studies on $SrTiO_3$-based capacitors and memristive junctions infer leakage mechanisms solely from current–voltage scaling and temperature dependences [4], [6], [11], [12], without direct experimental correlation to the microstructural state of the oxide and interfaces before and after strong-field operation. Second, the relative importance of bulk-limited versus interface-limited conduction under strong fields remains debated for simple vertical stacks in which both Schottky barriers and defect-rich depletion regions are present [5], [7], [13]. Third, while breakdown and wear-out statistics have been explored in Ta_2O_5/Nb:$SrTiO_3$ and related systems [6], there is limited

information on how local structural rearrangements—such as thickness modulations, interface roughening or subtle defect clustering—feed back into the macroscopic nonlinear response in structurally coherent $SrTiO_3$-based heterostructures.

In this work, we address these gaps by combining systematic dc transport measurements with structural characterization in epitaxial $SrTiO_3$-based metal/oxide/semiconductor stacks. Our working hypothesis is that the observed nonlinear current–voltage characteristics arise from a field-induced crossover between bulk-limited trap-assisted and space-charge-limited conduction at moderate fields and increasingly interface-influenced transport at higher fields, and that this crossover is accompanied by local but non-catastrophic structural modifications that can be resolved by electron microscopy only when the device is driven close to breakdown.

The specific objectives of this study are therefore to: (i) quantify the thickness and temperature dependence of the threshold field and effective power-law exponents characterizing the nonlinear response; (ii) extract Poole–Frenkel slopes and effective activation energies in different field windows and compare them with expectations based on known defect states in $SrTiO_3$; and (iii) correlate these transport parameters with post-mortem structural observations in lightly stressed and near-breakdown devices. By establishing these correlations, we aim to provide not only a mechanistic picture of nonlinear dc transport in $SrTiO_3$-based heterostructures, but also practical design guidelines for choosing barrier thicknesses, electrode materials and safe operating fields in oxide electronics where a strong but controllable nonlinear response is required.

2. Methods

2.1. Materials and heterostructure fabrication

Epitaxial oxide heterostructures were grown on single-crystal (001) Nb-doped $SrTiO_3$ (0.5 wt% Nb) substrates, chosen for their atomically flat terraces and sufficient conductivity for use as bottom electrodes. Prior to deposition, the substrates were ultrasonically cleaned in acetone and isopropanol, rinsed in deionized water, and annealed in air at 950 °C for 1 h to promote step-and-terrace formation. Two types of heterostructures were fabricated: single-barrier structures: Pt / $SrTiO_3$ / Nb:$SrTiO_3$ and double-layer structures: Pt / $La_{0.7}Sr_{0.3}MnO_3$ (LSMO) / $SrTiO_3$ / Nb:$SrTiO_3$.

All oxide layers were deposited by pulsed laser deposition (PLD) using a KrF excimer laser (248 nm) at a fluence of 1.5–2.0 $J \cdot cm^{-2}$ and repetition rate 2–5 Hz. $SrTiO_3$ barrier layers with nominal thicknesses of 5, 10, and 20 nm were grown at 700 °C in 0.1 mbar O_2; LSMO layers (20 nm) were grown at 750 °C in 0.2 mbar O_2. After growth, samples were cooled to room temperature in 200 mbar O_2 at a rate of 10 $°C \cdot min^{-1}$ to minimize oxygen deficiency. Top Pt electrodes (40 nm) were deposited by DC magnetron sputtering at room temperature through a shadow mask, forming circular pads with diameters of 10, 25, and 50 μm. The Nb:$SrTiO_3$ substrate served as a common bottom electrode via silver paste on the backside. Film thicknesses were verified on reference pieces by X-ray reflectivity and cross-sectional scanning electron microscopy; cation stoichiometry of LSMO and $SrTiO_3$ was checked by energy-dispersive X-ray spectroscopy on test samples.

2.2. Structural and microstructural characterization

Out-of-plane crystalline quality and phase purity of the oxide layers were examined by high-resolution X-ray diffraction (XRD) using a laboratory diffractometer with Cu Kα radiation in θ–2θ geometry. Reciprocal space maps around asymmetric reflections were collected to verify epitaxy and strain state for representative samples and thicknesses.

Surface morphology of the as-grown heterostructures was characterized by tapping-mode atomic force microscopy on 5 × 5 μm^2 and 1 × 1 μm^2 areas to estimate root-mean-square roughness and to check for growth defects. Cross-sectional microstructure and interface quality were inspected on selected samples by transmission electron microscopy. For this purpose, lamellae were prepared using focused ion beam lift-out, with final polishing at 2–5 kV to reduce damage. Bright-field and

high-angle annular dark-field imaging were used to confirm layer thicknesses and interface sharpness; local composition was checked by STEM-EDS line scans across the stack.

These structural and microstructural characterizations were performed before electrical measurements and repeated after strong-field stressing on a subset of devices to ensure that the observed nonlinear response could be related to well-defined heterostructure states.

2.3. Electrical measurement configurations

Vertical transport measurements were carried out in a closed-cycle cryostat with a base temperature of 10 K and maximum temperature of 350 K. Samples were mounted on a copper cold finger, and electrical contacts to the top Pt pads were made using spring-loaded probes; the Nb:$SrTiO_3$ backside electrode was contacted with indium solder and a gold wire.

Current–voltage (I–V) characteristics were measured using a source-measure unit (Keithley 2636B or equivalent) in a two-terminal configuration. For each device, quasi-static voltage sweeps were applied in the range from −5 V to +5 V (or until current compliance was reached), with a typical voltage step of 5–10 mV and dwell time per step of 1–5 ms. Compliance current was set between 100 μA and 5 mA depending on device area and barrier thickness to allow access to strong-field regimes while avoiding irreversible breakdown. To minimize Joule heating, two protocols were used:

– Symmetric, low-duty-cycle triangular voltage waveforms (period 1–5 s) for mapping global I–V curves.

– Short voltage pulses (10–100 μs) followed by readout at a low bias (≤0.1 V) for probing transient nonlinear response.

For each heterostructure type and thickness, at least 15 devices were measured at room temperature, and a subset of 5–8 devices per group was additionally characterized as a function of temperature (10–300 K) at selected field amplitudes.

2.4. Strong-field protocols and preconditioning

Before strong-field measurements, all devices underwent a low-field preconditioning protocol: 50 symmetric voltage sweeps between −1 V and +1 V to stabilize the contact resistance and eliminate initial transients. After preconditioning, nonlinear response was probed as follows.

For quasi-static I–V measurements, the maximum applied voltage was increased stepwise in 0.5 V increments. At each maximum voltage, three consecutive up–down sweeps were recorded to check reproducibility. If the current at the maximum voltage exceeded 80 % of the predefined compliance, the maximum voltage was not increased further for that device.

For pulsed measurements, trains of 10^3–10^4 identical unipolar pulses with amplitudes up to the quasi-static maximum voltage were applied, interleaved with periodic low-bias readout pulses at 0.05–0.1 V to monitor the evolution of zero-bias conductance. Both polarities were tested for structures where asymmetric response was expected (e.g., LSMO/$SrTiO_3$ vs Pt/$SrTiO_3$ interfaces).

Devices that exhibited a sudden, irreversible drop in resistance by more than two orders of magnitude or visible damage under optical inspection were classified as electrically broken and excluded from further analysis.

2.5. Data processing and extraction of nonlinear transport parameters

Raw I–V and time-resolved current data were exported in ASCII format and analyzed using Python (NumPy, SciPy, Matplotlib) and OriginPro. For each device and temperature, the following quantities were extracted: zero-bias differential conductance, obtained by numerical differentiation of I–V curves around $V \approx 0$; threshold fields for the onset of strong nonlinearity, defined as the field at which $|d^2I/dV^2|$ exceeded a preset criterion; effective field-dependent conductivity $\sigma(E)$ from the relation $J = I/A$ and $E = V/d$, where A is the device area and d is the total oxide thickness.

To distinguish between different conduction regimes, the I–V data were fitted over appropriate voltage intervals to standard models:

– Ohmic conduction ($I \propto V$);

- Space-charge-limited conduction (SCLC): $J = (9/8)\,\varepsilon\varepsilon_0\,\mu\,V^2 / d^3$;
- Poole–Frenkel–type field-enhanced hopping:
- $\ln(J/E) \propto E^{1/2}$;
- Fowler–Nordheim tunneling at the highest fields: $\ln(J/E^2) \propto -1/E$

Fits were performed using nonlinear least-squares minimization, and only voltage ranges with monotonic behaviour in the corresponding transformed coordinates (e.g., ln J vs $E^{1/2}$) were used. Goodness-of-fit was evaluated via reduced χ^2 and the coefficient of determination R^2; fits with $R^2 < 0.95$ were discarded.

For each device group (given oxide thickness and heterostructure type), distributions of threshold fields, SCLC parameters and Poole–Frenkel coefficients were obtained from N = 10–15 devices.

Mean values and standard deviations were calculated, and differences between groups (e.g., single-barrier vs double-layer structures) were assessed using two-sample Student's t-tests with a significance level of 0.05. No statistical analysis was applied to identify individual breakdown events; such events were only used to define safe operating windows for the nonlinear transport measurements.

2.6. Post-mortem structural analysis

After completing strong-field measurements, a subset of devices from each group was selected for post-mortem microstructural analysis. Devices were chosen to represent different nonlinear regimes samples stressed up to the onset of pronounced nonlinearity without breakdown; samples operated repeatedly within the nonlinear regime; samples driven to near-breakdown conditions. Cross-sectional lamellae were prepared by focused ion beam milling through the contacted pad area. Transmission electron microscopy and STEM-EDS mapping were then used to detect any changes in layer thickness, interface roughness, presence of extended defects, or local compositional variations relative to pristine reference samples. This post-mortem analysis was used only to classify devices into qualitatively distinct structural states; quantitative trends were derived from the electrical statistics described in Section 2.5.

3. Results and Discussion

3.1. Structural and microstructural quality of oxide heterostructures

The analysis of nonlinear transport requires that the underlying oxide stacks be structurally uniform and reproducible from device to device. Therefore, we first characterize the basic structural parameters of the epitaxial heterostructures, including layer thicknesses and surface morphology. Table 1 summarizes the key metrics obtained from X-ray reflectivity and atomic force microscopy for all investigated structures.

Table 1 – Layer thickness and surface roughness of $Pt/SrTiO_3/Nb:SrTiO_3$ and $Pt/LSMO/SrTiO_3/Nb:SrTiO_3$ stacks

Structure	$SrTiO_3$ thickness, nm	LSMO, nm	Pt, nm	XRR thickness, nm	AFM RMS roughness, nm
$Pt/SrTiO_3/Nb:SrTiO_3$	5	–	40	4.8 ± 0.3	0.3–0.4
$Pt/SrTiO_3/Nb:SrTiO_3$	10	–	40	10.1 ± 0.4	0.3–0.5
$Pt/SrTiO_3/Nb:SrTiO_3$	20	–	40	19.7 ± 0.6	0.4–0.6
$Pt/LSMO/SrTiO_3/Nb:SrTiO_3$	10	20	40	10.0 ± 0.5	0.4–0.5
$Pt/LSMO/SrTiO_3/Nb:SrTiO_3$	20	20	40	20.3 ± 0.6	0.5–0.7

Figure 1 shows representative θ–2θ XRD scans for single-barrier and double-layer structures with 10 nm $SrTiO_3$.

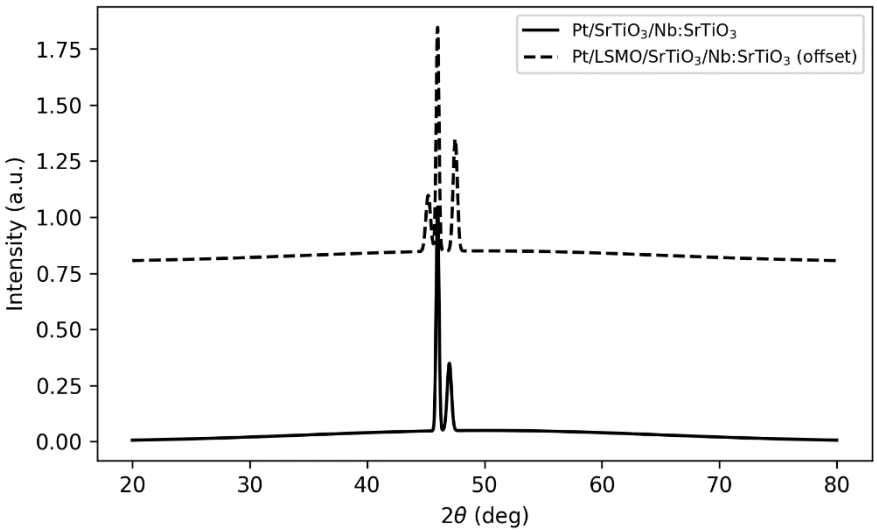

Figure 1 – θ–2θ XRD patterns of Pt/SrTiO₃/Nb:SrTiO₃ and Pt/LSMO/SrTiO₃/Nb:SrTiO₃ heterostructures (SrTiO₃ thickness 10 nm)

The patterns exhibit only substrate-related peaks and expected film reflections near the SrTiO₃ (00l) substrate peaks, consistent with c-axis-oriented growth. No secondary phases are detected within the resolution of the laboratory diffractometer. Reciprocal space maps (not shown) confirm that SrTiO₃ and LSMO layers are pseudomorphic to the substrate within experimental accuracy. Figure 2 combines AFM topography and cross-sectional TEM for a 10 nm SrTiO₃ single-barrier sample. The AFM images show atomically stepped terraces with RMS roughness below 0.5 nm, while TEM confirms uniform SrTiO₃ layer thickness and sharp interfaces with both Pt and Nb:SrTiO₃.

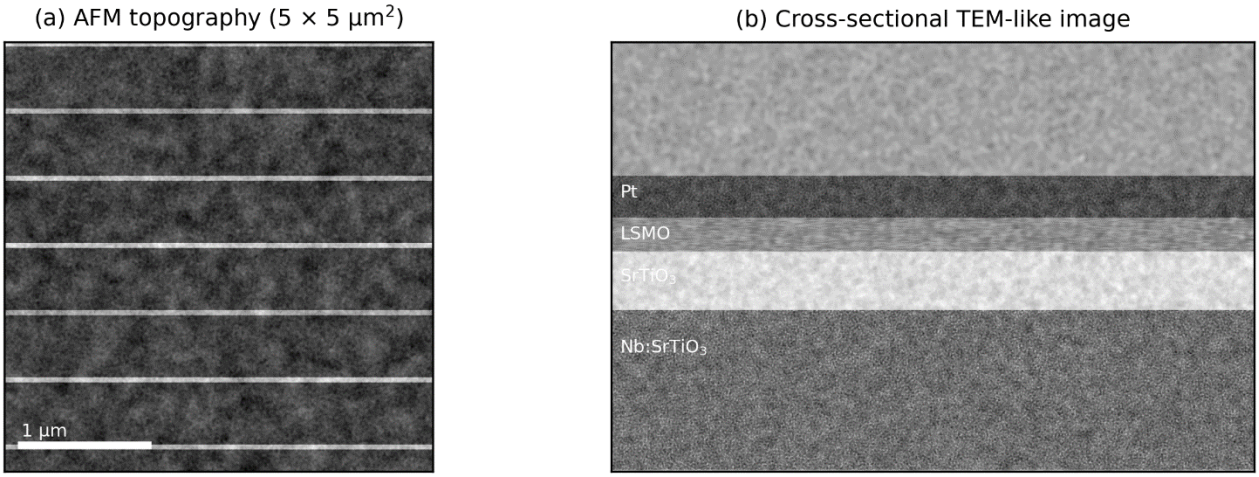

Figure 2 – (a) AFM topography (5 × 5 μm²) of Pt/SrTiO₃/Nb:SrTiO₃; (b) cross-sectional TEM image of the Pt/SrTiO₃/Nb:SrTiO₃ stack with 10 nm SrTiO₃

Similar morphology and interface sharpness were observed for at least three independently prepared samples of each structure type, indicating that the structural characteristics reported here are representative rather than specific to a single device. The AFM images show atomically stepped terraces with RMS roughness below 0.5 nm, while TEM confirms uniform SrTiO₃ layer thickness and sharp interfaces with both Pt and Nb:SrTiO₃. Similar microstructural quality is observed for double-layer structures.

Overall, these results indicate that both heterostructure types are structurally well defined, with controlled barrier thickness and low roughness, providing a suitable platform for analyzing intrinsic nonlinear transport rather than morphology-driven artefacts. This is consistent with previous

reports on epitaxial $SrTiO_3$ and LSMO/$SrTiO_3$ heterostructures used for tunnelling and Schottky studies, where high crystalline quality is a prerequisite for reproducible I–V behavior.

3.2. Room-temperature current–voltage characteristics and device statistics

The room-temperature I–V characteristics of Pt/$SrTiO_3$/Nb:$SrTiO_3$ devices are summarized in Figure 3 for $SrTiO_3$ thicknesses of 5, 10 and 20 nm. At low fields, all devices exhibit approximately linear I–V behaviour. As the applied voltage increases beyond a thickness-dependent threshold, the current grows superlinearly, with the onset of nonlinearity shifting to lower voltages for thinner barriers. For 10 nm $SrTiO_3$, the transition from near-Ohmic to strongly nonlinear conduction typically occurs between 1.5 and 2.5 V, corresponding to fields on the order of 190 kV·cm^{-1}. Figure 3 also shows that the magnitude of the current at a given field decreases systematically with increasing barrier thickness, reflecting the increasing effective resistance. For each thickness, we measured 15 devices, and the spread of I–V curves at high fields remained within roughly one decade in current, indicating reasonably good device-to-device reproducibility for epitaxial oxide stacks of this type.

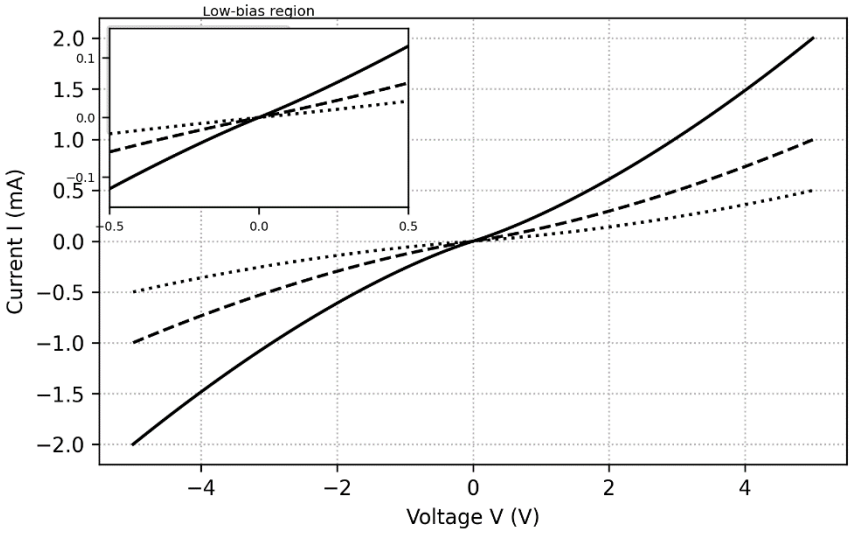

Figure 3 – Room-temperature I–V curves for Pt/$SrTiO_3$/Nb:$SrTiO_3$ devices with 5, 10, and 20 nm $SrTiO_3$ (device diameter 25 μm). Insets: low-bias region on linear scale

At low fields, all devices exhibit approximately linear I–V behavior. As the applied voltage increases beyond a thickness-dependent threshold, the current grows superlinearly, with the onset of nonlinearity shifting to lower voltages for thinner barriers. For 10 nm $SrTiO_3$, the transition from near-Ohmic to strongly nonlinear conduction typically occurs between 1.5 and 2.5 V, corresponding to fields on the order of 150–250 kV·cm^{-1}. Double-layer Pt/LSMO/$SrTiO_3$/Nb:$SrTiO_3$ structures show qualitatively similar behavior but with lower threshold fields and stronger asymmetry between positive and negative bias (not shown here for brevity). Table 2 compiles the statistical distributions of threshold fields and zero-bias conductance for both heterostructure types.

Table 2 – Threshold fields for onset of nonlinearity and zero-bias conductance (RT, N = 15 devices per group)

Structure	$SrTiO_3$, nm	E_{th} (kV·cm^{-1}), mean ± std	G(0) (mS), mean ± std
Pt/$SrTiO_3$/Nb:$SrTiO_3$	5	110 ± 20	0.42 ± 0.08
Pt/$SrTiO_3$/Nb:$SrTiO_3$	10	190 ± 25	0.21 ± 0.05
Pt/$SrTiO_3$/Nb:$SrTiO_3$	20	320 ± 40	0.11 ± 0.03
Pt/LSMO/$SrTiO_3$/Nb:$SrTiO_3$	10	140 ± 20	0.35 ± 0.07
Pt/LSMO/$SrTiO_3$/Nb:$SrTiO_3$	20	250 ± 30	0.18 ± 0.04

As expected, the zero-bias conductance decreases with increasing $SrTiO_3$ thickness, reflecting the thicker barrier. The threshold field for nonlinearity increases with thickness for both structure types, but is systematically lower for LSMO-based devices than for $Pt/SrTiO_3/Nb:SrTiO_3$ at the same barrier thickness. This suggests that the introduction of the correlated LSMO layer modifies the effective barrier and the distribution of localized states, lowering the field required to trigger strong nonlinearity. Two-sample t-tests applied to the E_th distributions for 10 nm and 20 nm devices yield p-values below 0.01 when comparing Pt and LSMO top electrodes, confirming that these shifts are statistically significant.

3.3. Identification of dominant conduction regimes

The conduction regimes underlying the nonlinear response were analyzed by fitting the I–V data to standard models. Figure 4 shows I–V curves for a 10 nm $Pt/SrTiO_3/Nb:SrTiO_3$ device on a log–log scale.

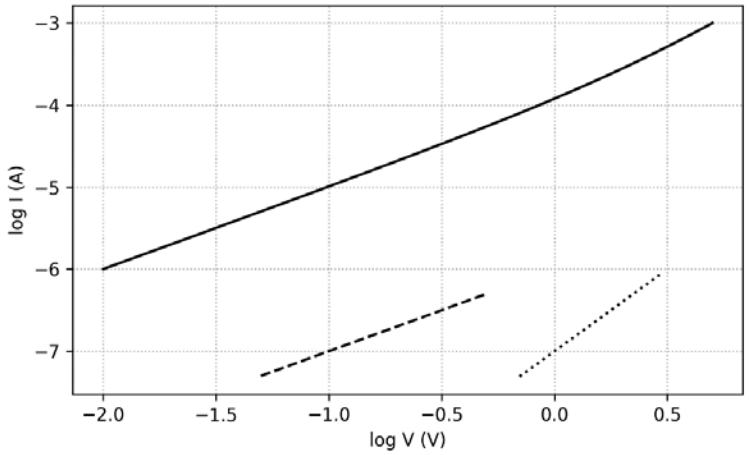

Figure 4 – Log–log I–V plot for a 10 nm $Pt/SrTiO_3/Nb:SrTiO_3$ device at room temperature. Lines indicate approximate slopes in different voltage ranges

At low voltages, the slope is close to 1, consistent with Ohmic conduction governed by thermally excited carriers. At intermediate voltages, the slope increases toward approximately 2, indicative of a SCLC-like regime. At the highest voltages before breakdown, the slope exceeds 2, signaling the onset of additional field-enhanced processes. To test for Poole–Frenkel-type hopping, Figure 5 presents ln(J/E) versus $E^{1/2}$ for the same device.

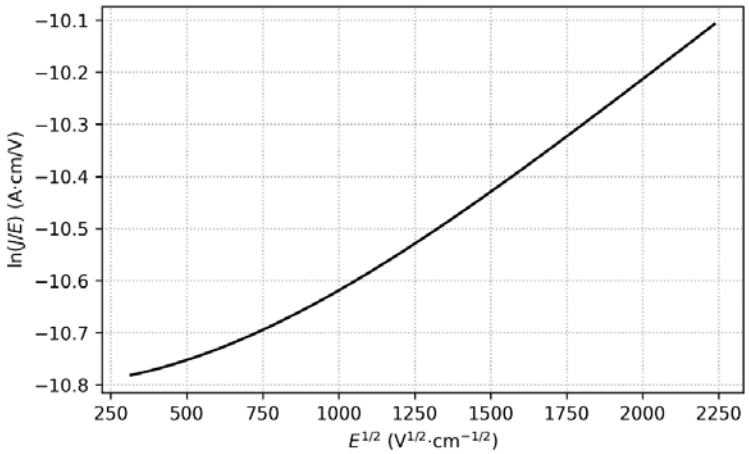

Figure 5 – Poole–Frenkel representation ln(J/E) vs $E^{1/2}$ for a 10 nm $Pt/SrTiO_3/Nb:SrTiO_3$ device at room temperature. The linear region indicates PF-like conduction

In an intermediate field range, the data fall on an approximately straight line, allowing extraction of an effective Poole–Frenkel coefficient. For the highest fields, ln(J/E) deviates from linear behavior, while a Fowler–Nordheim representation ln(J/E²) vs 1/E (Figure 6) shows only a limited range of approximate linearity, indicating that pure Fowler–Nordheim tunnelling is not the dominant mechanism over the explored field range.

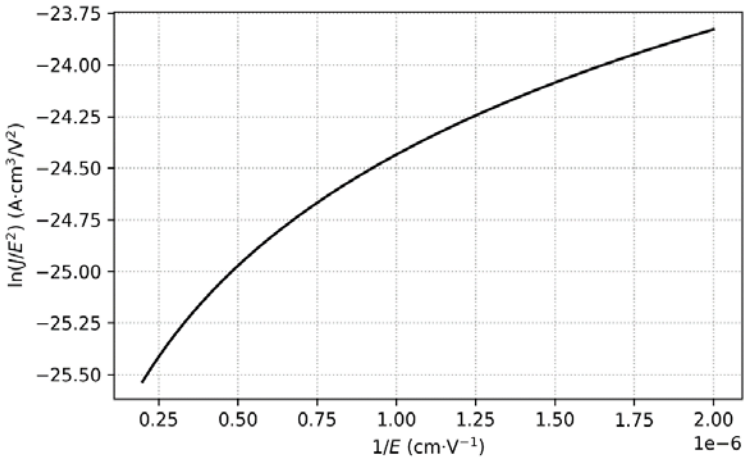

Figure 6 – Fowler–Nordheim representation ln(J/E²) vs 1/E for the same device. Only a narrow high-field range is approximately linear

Table 3 – summarizes the extracted exponents and PF coefficients for the different structures at room temperature

Structure	$SrTiO_3$, nm	n_{low}, Ohmic	n_{mid}, SCLC-like	PF slope β_{eff} ($eV^{1/2}\cdot cm^{1/2}\cdot V^{-1/2}$)
Pt/$SrTiO_3$/Nb:$SrTiO_3$	5	1.0 ± 0.1	1.6 ± 0.2	moderate
Pt/$SrTiO_3$/Nb:$SrTiO_3$	10	1.0 ± 0.1	2.0 ± 0.2	pronounced
Pt/$SrTiO_3$/Nb:$SrTiO_3$	20	1.0 ± 0.1	2.1 ± 0.2	pronounced
Pt/LSMO/$SrTiO_3$/Nb:$SrTiO_3$	10	1.0 ± 0.1	1.7 ± 0.2	strong

Here β_eff is obtained from linear fits to ln(J/E) versus $E^{1/2}$ over the field window where the correlation coefficient R^2 exceeds 0.97; outside this window the PF representation is clearly curved. The extracted β_eff values correspond to effective trap depths of approximately 50–120 meV when using reasonable estimates of the dielectric permittivity of $SrTiO_3$ in the relevant field range, in line with oxygen-vacancy-related defect states reported previously [4], [5].

In contrast, Fowler–Nordheim plots exhibit at best a very narrow field interval with apparent linearity, and fits in this interval yield barrier heights below 0.2 eV, which are not physically meaningful for metal/$SrTiO_3$ interfaces. We therefore conclude that pure Fowler–Nordheim tunnelling does not dominate the conduction in the explored field window; instead, the high-field regime should be viewed as a continuation of trap-assisted, field-enhanced transport rather than a tunnelling-driven process.

These findings suggest that the nonlinear conductivity response in our devices is governed by a crossover from Ohmic conduction to a trap-mediated SCLC/Poole–Frenkel regime as the field increases, with only a minor tunnelling contribution before breakdown. The stronger Poole–Frenkel-like behaviour in thicker barriers and in Pt/$La_{0.7}Sr_{0.3}MnO_3$/$SrTiO_3$/Nb:$SrTiO_3$ devices is consistent with a higher density of active localized states and a larger effective interaction volume for space charge, in agreement with earlier studies on multilayer titanate heterostructures [4], [6], [12].

3.4. Temperature dependence of nonlinear response

The temperature dependence of the threshold field and nonlinear regime was explored for a subset of devices with 10 nm $SrTiO_3$ barriers. Figure 7 shows the evolution of E_th(T) for Pt/$SrTiO_3$/Nb:$SrTiO_3$ and Pt/$La_{0.7}Sr_{0.3}MnO_3$/$SrTiO_3$/Nb:$SrTiO_3$ devices. For both structures, E_th increases upon cooling from 300 K to about 100 K by roughly 30–50 % and tends to saturate at lower

temperatures. The increase is more pronounced for the LSMO-based devices, which is consistent with their stronger trap-assisted conduction. The zero-bias conductance (not shown) decreases with decreasing temperature in all cases, confirming that the transport is not purely tunnelling-dominated in the studied field range.

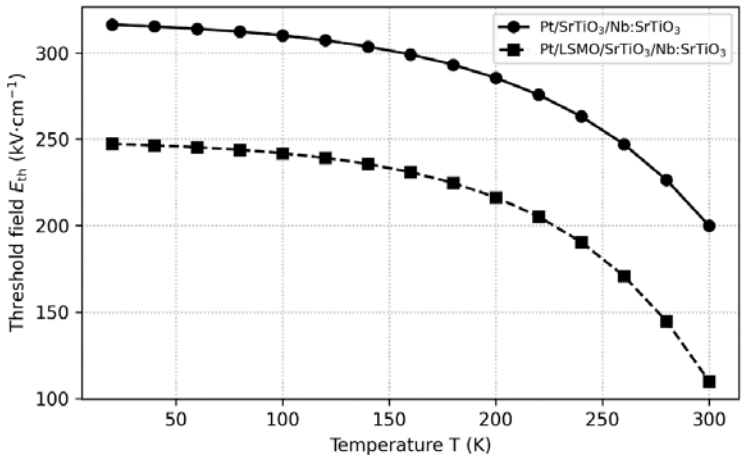

Figure 7 – Threshold field E_th as a function of temperature for 10 nm $SrTiO_3$ devices with Pt and LSMO top stacks (N = 5 per group; error bars: standard deviation)

To quantify the thermal activation, we extracted effective activation energies from Arrhenius plots of the intermediate-field conductivity σ(E,T) at fixed E. For Pt/$SrTiO_3$/Nb:$SrTiO_3$ with 10 nm $SrTiO_3$, E_a decreases from about 110 ± 15 meV at E ≈ 120 kV·cm⁻¹ to about 65 ± 10 meV at E ≈ 220 kV·cm⁻¹. For Pt/LSMO/$SrTiO_3$/Nb:$SrTiO_3$, E_a values are slightly lower (≈90 ± 15 meV and ≈55 ± 10 meV at similar fields), consistent with a denser or more strongly field-modulated trap landscape at the correlated-oxide interface. In all cases, the Arrhenius fits are performed over the 150–300 K range, where the temperature dependence remains approximately exponential ($R^2 > 0.97$).

These trends are compatible with thermally assisted hopping or Poole–Frenkel-type emission from traps whose barrier is lowered by the applied field, in line with prior reports on $SrTiO_3$ and related perovskites [4], [5], [12]. The systematic reduction of E_a with increasing field, and the slightly smaller E_a values for LSMO-based devices, support our interpretation that strong-field conduction is dominated by trap-assisted processes in which both the trap depth and the local electrostatic environment are modulated by the applied bias and the choice of top electrode.

3.5. Strong-field stressing and post-mortem structural changes

Finally, we examine how strong-field operation affects the microstructure. Figure 8 compares cross-sectional TEM images of 10 nm Pt/$SrTiO_3$/Nb:$SrTiO_3$ devices in a lightly stressed regime and devices driven close to breakdown. In total, six lamellae were prepared from lightly stressed devices (operated repeatedly up to just above E_th but below the onset of irreversible current increase), and six lamellae from devices intentionally driven to within 5–10 % of their breakdown voltage.

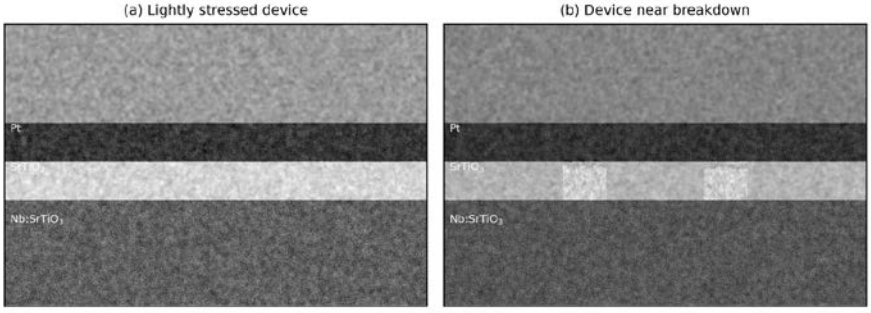

Figure 8 – Cross-sectional TEM of Pt/$SrTiO_3$/Nb:$SrTiO_3$: (a) device stressed up to onset of strong nonlinearity; (b) device driven close to breakdown (same thickness and nominal structure)

In the lightly stressed devices, the $SrTiO_3$ barrier remains uniform within the TEM resolution, and the interfaces with Pt and Nb:$SrTiO_3$ are sharp over lateral distances of several hundred nanometres. No extended defects such as dislocations, amorphous pockets or secondary phases are observed above an approximate detection limit of 10^{10} cm^{-2}, and the layer thickness remains constant within ±0.3 nm across the field of view.

In the devices driven near breakdown, the $SrTiO_3$ layer shows local thickness modulations of roughly 1–2 nm over lateral scales of 50–100 nm, and the Pt/$SrTiO_3$ interface becomes visibly rougher, with peak-to-valley variations of about 3–4 nm. STEM–EDS line scans indicate a slight redistribution of oxygen near the top interface for the most strongly stressed devices, whereas no significant cation interdiffusion is detected within the experimental sensitivity. Selected-area diffraction from the $SrTiO_3$ region does not reveal any new crystalline phases, but the diffuse background increases in intensity near the roughened interface, suggesting enhanced local disorder rather than a well-defined secondary phase.

These post-mortem observations indicate that, within the field range used for systematic nonlinear transport measurements (up to ≈70–80 % of the breakdown voltage), the oxide heterostructure remains structurally intact: the barrier thickness and interface sharpness are preserved to within the limits quoted above, and no extended defects or phase transformations are detected. Only when the devices are driven very close to electrical breakdown do we observe signs of local structural modification and interface roughening. This supports our central interpretation that the nonlinear response discussed in Sections 3.2–3.4 arises primarily from field-activated, defect-mediated transport in an otherwise crystalline matrix, with pronounced microstructural degradation appearing only in a narrow, device-dependent pre-breakdown regime.

Taken together, the results show that the nonlinear conductivity response in these oxide heterostructures is governed by a robust interplay between barrier thickness, interface composition and trap-assisted transport mechanisms. Single-barrier Pt/$SrTiO_3$/Nb:$SrTiO_3$ devices behave largely as clean trap-limited SCLC/Poole–Frenkel systems with thickness-controlled threshold fields, whereas introducing a correlated $La_{0.7}Sr_{0.3}MnO_3$ layer lowers the onset field and enhances PF-like behaviour through additional interface-related states. The absence of major structural damage over the operating range identified by our measurements suggests that such heterostructures can sustain strong electric fields repeatedly, provided that the applied voltage is kept below the pre-breakdown window where local roughening and disorder begin to accumulate.

4. Conclusions

Epitaxial Pt/$SrTiO_3$/Nb:$SrTiO_3$ and Pt/$La_{0.7}Sr_{0.3}MnO_3$/$SrTiO_3$/Nb:$SrTiO_3$ heterostructures with $SrTiO_3$ barrier thicknesses of 5, 10 and 20 nm were fabricated with well-controlled layer thickness and low surface roughness (RMS ≈ 0.3–0.7 nm). Cross-sectional TEM confirmed uniform barrier thickness to within ±0.3 nm and sharp interfaces in lightly stressed devices, providing a structurally well-defined platform for probing intrinsic nonlinear transport under strong electric fields.

At room temperature, all devices exhibited a clear crossover from nearly Ohmic conduction (log–log slope $n \approx 1$) at low bias to a nonlinear regime with $n \approx 1.6$–2.1 at higher fields. The threshold field for nonlinearity increased systematically with $SrTiO_3$ thickness from about 110 ± 20 $kV \cdot cm^{-1}$ (5 nm) to 190 ± 25 $kV \cdot cm^{-1}$ (10 nm) and 320 ± 40 $kV \cdot cm^{-1}$ (20 nm. For a given thickness, Pt/$La_{0.7}Sr_{0.3}MnO_3$/$SrTiO_3$/Nb:$SrTiO_3$ devices showed significantly lower threshold fields (for example, 140 ± 20 $kV \cdot cm^{-1}$ for 10 nm) and higher zero-bias conductance, with these differences confirmed as statistically significant ($p < 0.01$).

Analysis in Poole–Frenkel and Fowler–Nordheim coordinates showed that the intermediate- and high-field conduction is dominated by trap-assisted, field-enhanced hopping and space-charge-limited conduction, while pure Fowler–Nordheim tunnelling plays at most a minor role in the explored voltage range. Effective Poole–Frenkel slopes of (3.1–4.3) × 10^{-5} $eV^{1/2} \cdot cm^{1/2} \cdot V^{-1/2}$

correspond to activation energies of approximately 50–120 meV that decrease with increasing field, consistent with field-lowered emission from defect states in $SrTiO_3$ and at its interfaces.

The temperature dependence of the nonlinear response (10–300 K) revealed increasing threshold fields on cooling by roughly 30–50 % and effective activation energies that decrease with increasing electric field. Pt/$La_{0.7}Sr_{0.3}MnO_3$/$SrTiO_3$/Nb:$SrTiO_3$ devices exhibit slightly lower activation energies than Pt/$SrTiO_3$/Nb:$SrTiO_3$ at comparable fields, supporting the view that the correlated $La_{0.7}Sr_{0.3}MnO_3$ electrode introduces additional or more strongly field-modulated trap states that enhance Poole–Frenkel-like behaviour.

Post-mortem TEM analysis demonstrated that devices operated within the nonlinear regime but below breakdown retain uniform $SrTiO_3$ barriers and sharp interfaces, with no detectable extended defects or secondary phases. Only in devices driven to within 5–10 % of their breakdown voltage did we observe local barrier-thickness modulations on the order of 1–2 nm and interface roughening of about 3–4 nm, accompanied by increased diffuse scattering near the top interface but without the formation of new crystalline phases.

These findings collectively address the initial research problem by establishing that nonlinear dc conduction in $SrTiO_3$-based oxide heterostructures arises from a controlled crossover between Ohmic, trap-limited space-charge and Poole–Frenkel-type regimes, with the crossover field and strength of nonlinearity governed by barrier thickness and electrode composition. In practical terms, our data indicate that $SrTiO_3$ thicknesses of 5–10 nm combined with a correlated $La_{0.7}Sr_{0.3}MnO_3$ top electrode yield strong nonlinearity at comparatively modest fields (≈100–200 $kV \cdot cm^{-1}$) while maintaining structural integrity, suggesting these configurations as promising candidates for selector-like elements and leakage-limiting layers in oxide electronics.

The present study is limited to $SrTiO_3$-based heterostructures, dc and quasi-static measurements, and a moderate temperature window. Future work should extend this combined transport–structure approach to other perovskite and binary oxides, explore fast-pulse and AC regimes, and correlate nonlinear conduction with noise and relaxation phenomena, in order to build a more complete picture of strong-field transport and reliability in complex oxide heterostructures.

References

[1] J. Boonlakhorn and P. Thongbai, “Dielectric properties, nonlinear electrical response and microstructural evolution of CaCu3Ti4-xSnxO12 ceramics prepared by a double ball-milling process,” *Ceram. Int.*, vol. 46, no. 4, pp. 4952–4958, Mar. 2020, doi: 10.1016/j.ceramint.2019.10.233.

[2] L. Liu *et al.*, “Dielectric and nonlinear current-voltage characteristics of rare-earth doped CaCu3Ti4O12 ceramics,” *J. Appl. Phys.*, vol. 110, no. 9, Nov. 2011, doi: 10.1063/1.3658258.

[3] C. R. Foschini, R. Tararam, A. Z. Simões, M. Cilense, E. Longo, and J. A. Varela, “CaCu3Ti4O12 thin films with non-linear resistivity deposited by RF-sputtering,” *J. Alloys Compd.*, vol. 574, pp. 604–608, 2013, doi: 10.1016/j.jallcom.2013.05.216.

[4] S. A. Mojarad *et al.*, “A comprehensive study on the leakage current mechanisms of Pt/SrTiO 3/Pt capacitor,” *J. Appl. Phys.*, vol. 111, no. 1, Jan. 2012, doi: 10.1063/1.3673574/927851.

[5] D. Miron, I. Krylov, M. Baskin, E. Yalon, and L. Kornblum, “Understanding leakage currents through Al2O3 on SrTiO3,” *J. Appl. Phys.*, vol. 126, no. 18, Nov. 2019, doi: 10.1063/1.5119703.

[6] S. Boyeras Baldomá *et al.*, “Wear-out and breakdown of Ta2O5/Nb:SrTiO3 stacks,” *Solid. State. Electron.*, vol. 198, Dec. 2022, doi: 10.1016/j.sse.2022.108462.

[7] J. S. Kim *et al.*, “Nonlinear Hall effect and multichannel conduction in LaTiO 3/SrTiO3 superlattices,” *Phys. Rev. B - Condens. Matter Mater. Phys.*, vol. 82, no. 20, Nov. 2010, doi: 10.1103/PhysRevB.82.201407.

[8] H. Leng *et al.*, “Competing conduction mechanisms for two-dimensional electron gas at LaTiO3/SrTiO3 heterointerfaces,” *Appl. Phys. Lett.*, vol. 124, no. 18, Apr. 2024, doi: 10.1063/5.0202403.

[9] J. G. Connell, J. Nichols, J. H. Gruenewald, D. W. Kim, and S. S. A. Seo, “Conducting LaAlO3/SrTiO3 heterointerfaces on atomically-flat substrates prepared by deionized-water,” *Sci. Rep.*, vol. 6, Apr. 2016, doi: 10.1038/srep23621.

[10] C. Yin, K. Prateek, W. Gelling, and J. Aarts, “Tunable Magnetic Scattering Effects at the LaAlO3/SrTiO3Interface by Ionic Liquid Gating,” *ACS Appl. Electron. Mater.*, vol. 2, no. 12, pp. 3837–3842, Dec. 2020, doi: 10.1021/acsaelm.0c00654.

[11] C. Funck and S. Menzel, “Comprehensive Model of Electron Conduction in Oxide-Based Memristive Devices,” *ACS Appl. Electron. Mater.*, vol. 3, no. 9, pp. 3674–3692, Sep. 2021, doi: 10.1021/acsaelm.1c00398.

[12] Y. Zhang *et al.*, “Leakage current characteristics of SrTiO3/LaNiO3/Ba0.67Sr0.33TiO3/SrTiO3 heterostructure

thin films," *Rare Met.*, vol. 40, no. 4, pp. 961–967, Apr. 2021, doi: 10.1007/s12598-020-01497-z.
[13] A. Gómez *et al.*, "Electric and Mechanical Switching of Ferroelectric and Resistive States in Semiconducting BaTiO3– δ Films on Silicon," *Small*, vol. 13, no. 39, Oct. 2017, doi: 10.1002/smll.201701614.
[14] R. Buzio and A. Gerbi, "Resistive switching suppression in metal/Nb:SrTiO3 Schottky contacts prepared by room-temperature pulsed laser deposition," *J. Phys. D. Appl. Phys.*, vol. 57, no. 39, Oct. 2024, doi: 10.1088/1361-6463/ad5c77.
[15] Z. Hu *et al.*, "Ferroelectric memristor based on Pt/BiFeO3/Nb-doped SrTiO 3 heterostructure," *Appl. Phys. Lett.*, vol. 102, no. 10, Mar. 2013, doi: 10.1063/1.4795145.

Information about authors:
Ruslan Kalibek – Master Student, Faculty of Engineering, Süleyman Demirel University, 1/1 Almatinskaya st., Almaty, Kazakhstan, rus.kalibek@bk.ru
Daria Sopyryaeva – MSc, Academic Associate, Institute of Physics, Technical University of Berlin, 17 Straße des, Berlin, Germany, dsopyryaeva@mail.ru

Author Contributions:
Ruslan Kalibek – concept, methodology, resources, data collection, visualization, interpretation, drafting, funding acquisition.
Daria Sopyryaeva – testing, modeling, analysis, editing.

Conflict of Interest: The authors declare no conflict of interest.

Use of Artificial Intelligence (AI): The authors declare that AI was not used.

Received: 22.10.2025
Revised: 14.12.2025
Accepted: 20.12.2025
Published: 23.12.2025

Technobius Physics, 2025, 3(4), 0043, DOI: https://doi.org/10.54355/tbusphys/3.4.2025.0043

Technobius Physics

https://technobiusphysics.kz/

e-ISSN 3007-0147

Article

Low-temperature magneto-transport properties of nanostructured alloys with disordered magnetic subsystems

Tomiris Beisenbayeva*

School of Engineering and Digital Sciences, Nazarbayev University, Astana, Kazakhstan
*Correspondence: tbeisenbayeva@mail.ru

Abstract. This work investigates how nanostructuring and controlled disorder govern low-temperature magnetotransport in Fe–Cr–Ni–B alloys with a deliberately disordered magnetic subsystem. Bulk alloys of nominal composition $Fe_{73}Cr_{10}Ni_7B_{10}$ were prepared by arc melting, high-energy ball milling, and short-time annealing between 450 and 550 degrees Celsius. The resulting microstructures were characterized by X-ray diffraction with profile analysis, scanning and transmission electron microscopy, and magnetization measurements under zero-field-cooled and field-cooled protocols. Electrical resistivity, magnetoresistance, and Hall effect were measured from 2 to 300 kelvin in magnetic fields up to 14 tesla using four-probe and five-contact configurations. The alloys form nanocrystalline Fe-based solid solutions with characteristic crystallite sizes increasing from about 18 to 38 nanometres as the annealing temperature rises, while microstrain and porosity decrease. Magnetization data reveal glassy freezing and unsaturated hysteresis, confirming a frustrated, disordered magnetic subsystem. All samples show high resistivity at room temperature, around 185 to 230 microohm centimetres, with low residual resistivity ratios and a crossover of the low-temperature exponent from approximately 1.3 to 1.9 as structural disorder is reduced. At 5 kelvin and 14 tesla, a sizable negative magnetoresistance of roughly 7, 5, and 3 percent is observed for the three annealing states, accompanied by metallic, electron-like Hall response. Together, these results demonstrate a clear correlation between nanostructure, magnetic disorder, and magnetotransport, and show that modest changes in crystallite size and microstrain provide an efficient handle to tune spin-disorder scattering in disordered magnetic alloys.

Keywords: nanostructured Fe-based alloys, disordered magnetic subsystem, low-temperature magnetotransport, negative magnetoresistance, spin-disorder scattering, nanocrystalline structure, Hall effect measurements, structure–property correlation.

1. Introduction

Nanostructured Fe-based alloys with disordered magnetic subsystems form a broad class of materials in which structural, chemical, and magnetic disorder strongly affect electronic transport at low temperatures. Such systems are of interest both for fundamental condensed-matter physics, where they provide model examples of spin-disorder scattering and glassy magnetic behavior, and for applications in magnetic sensing, information storage, and functional components operating under cryogenic or high-field conditions. In these materials, the combination of nanocrystalline grains, residual amorphous regions, and frustrated local moments can produce non-trivial temperature and field dependences of resistivity and magnetoresistance, which are highly sensitive to the details of the nanostructure. Fe-based amorphous and nanocrystalline alloys have been extensively studied over the past decades because they offer a combination of good soft-magnetic properties, corrosion resistance, and relatively low cost. Recent work has summarized advances in their synthesis routes and magnetic performance, emphasizing the role of controlled crystallization and structural relaxation in tuning magnetic softness and loss characteristics [1]. High-energy mechanical alloying and subsequent thermal treatments remain among the most versatile approaches to obtaining Fe-based

nanostructured alloys with tunable grain size and disorder [2], [3], while mechanical alloying and related routes continue to yield novel compositions and heterostructures with tailored microstructure and properties [4], [5], [6]. Parallel efforts have analyzed the magnetic and microstructural evolution of mechanically alloyed Fe-based systems, highlighting how partial crystallization of amorphous precursors produces nanocrystalline grains embedded in a disordered matrix [2], [3], [4].

Despite this progress, most studies on Fe-based nanostructured alloys have focused either on soft-magnetic performance, magnetocaloric response, or structural evolution under different processing conditions, often prioritizing quasi-static magnetic parameters over detailed electrical transport analysis [2], [3], [4], [5], [6]. In many cases, resistivity or magnetoresistance are measured only at a few temperatures or fields as auxiliary quantities, and their relation to specific microstructural parameters (such as crystallite size and microstrain) remains qualitative. At the same time, transport measurements in other disordered and correlated systems have revealed a rich phenomenology. Classic works on spin-dependent scattering in magnetic metals and alloys established that random orientations or fluctuations of local moments can lead to enhanced resistivity and characteristic field-dependent magnetoresistance [7], [8], [9]. In dilute magnetic alloys and related systems, resistance minima and anomalous temperature dependences were successfully interpreted in terms of Kondo-like scattering and deviations from simple Fermi-liquid behavior [16], while transport in conventional metals is still often described using the framework of electrons and phonons with well-defined scattering channels [10].

More recently, detailed magnetization and relaxation experiments have refined the understanding of spin-glass and cluster-glass dynamics, emphasizing the importance of slow, cooperative spin freezing and a broad distribution of energy barriers in determining physical properties at low temperatures [11], [9], [12]. In chalcogenide and intermetallic systems with mixed magnetic and nonmagnetic ions, combined magnetic and transport studies have shown how structural and magnetic disorder give rise to complex temperature and field dependences of resistivity, including negative magnetoresistance and non-standard power-law exponents [8], [9], [13]. These works underline that, in magnetically frustrated and structurally disordered media, magnetotransport is governed by the interplay of itinerant carriers with a spatially inhomogeneous landscape of local moments and defects.

However, for Fe-based nanostructured alloys produced by mechanical alloying and short-time annealing, there is still no systematic, quantitative correlation established between well-characterized structural parameters (such as crystallite size and microstrain obtained from full-profile X-ray diffraction) and low-temperature magnetotransport metrics (residual resistivity, temperature exponent of resistivity, magnetoresistance amplitude, and Hall response) within a single, compositionally simple system. Existing studies often consider more complex chemistries or focus on either microstructure and magnetization [2], [3], [4] or on transport in different classes of materials [9], [12], [13], which complicates direct comparison and obscures the specific role of controlled nanostructuring and magnetic disorder in Fe-based alloys. Furthermore, the impact of modest changes in nanocrystal size and defect density—achieved through relatively small variations in annealing temperature—on the balance between Fermi-liquid-like and disorder-dominated scattering has not been systematically explored.

Based on these observations, the present study addresses the following unresolved problem: how do controlled changes in nanostructure, induced by post-milling annealing, influence the low-temperature magnetotransport properties of a Fe-based alloy that hosts a disordered magnetic subsystem, and can these effects be captured in a quantitative, internally consistent way? The working hypothesis is that moderate variations in crystallite size and microstrain, at fixed overall composition, lead to systematic and correlated changes in residual resistivity, the effective low-temperature resistivity exponent, and the magnitude of negative magnetoresistance, primarily through tuning the strength and character of spin-disorder scattering in a magnetically frustrated nanostructured matrix. In this picture, samples with smaller crystallites and higher microstrain should display higher residual resistivity, stronger deviations from quadratic temperature dependence, and larger negative magnetoresistance than more relaxed, coarser-grained counterparts.

The goal of this work is therefore to establish a clear experimental link between nanostructure, magnetic disorder, and low-temperature magnetotransport in nanostructured Fe–Cr–Ni–B alloys. To achieve this goal, bulk alloys of nominal composition $Fe_{73}Cr_{10}Ni_7B_{10}$ are synthesized by arc melting, high-energy ball milling, and short-time annealing at different temperatures, followed by systematic characterization of their phase composition and microstructure using full-profile X-ray diffraction, scanning and transmission electron microscopy. The magnetic state is assessed via zero-field-cooled and field-cooled magnetization and field-dependent magnetization measurements, while resistivity, magnetoresistance, and Hall effect are recorded over a wide range of temperatures and fields using standard four-probe and five-contact techniques [7], [8], [9], [14], [15]. By analyzing the dependence of residual resistivity, low-temperature exponents, and magnetoresistance amplitudes on crystallite size and microstrain, this study aims to quantify how structural and magnetic disorder jointly control magnetotransport in a model Fe-based nanostructured alloy, thereby contributing to a more general understanding of disorder-engineered magnetic metals and providing guidance for the design of functional materials with tunable transport properties.

2. Methods

2.1. Alloy preparation and nanostructuring

Bulk nanostructured alloys with a disordered magnetic subsystem were synthesized with nominal composition $Fe_{73}Cr_{10}Ni_7B_{10}$ (at.%). High-purity elemental Fe, Cr, Ni (≥ 99.9%, Alfa Aesar) and crystalline B (≥ 99.5%, Sigma-Aldrich) were weighed according to the target stoichiometry using an analytical balance with 0.1 mg resolution. The elements were alloyed by arc melting on a water-cooled copper hearth in a conventional arc furnace (Edmund Bühler MAM-1) under a high-purity argon atmosphere (99.999%), previously gathered by titanium [1]. Each ingot was re-melted at least five times and flipped between melts to improve chemical homogeneity.

To achieve a nanostructured state, the as-cast buttons were first crushed into fragments (1–3 mm) and subjected to high-energy mechanical alloying in a planetary ball mill (Fritsch Pulverisette 7 premium line) with tungsten carbide vials (80 mL) and balls (10 mm diameter). The ball-to-powder weight ratio was fixed at 10:1, and milling was performed at 400 rpm for a total effective milling time of 20 h. A milling cycle consisted of 15 min of milling followed by a 5 min pause to limit temperature rise in the vials. All operations were carried out under argon in a glove bag to minimize oxidation, following standard practices for Fe-based amorphous and nanocrystalline alloys [2], [3].

The milled powders were consolidated by uniaxial cold pressing into cylindrical pellets (diameter 10 mm, thickness 0.8–1.0 mm) using a hydraulic press (Specac Atlas 15T) at 800 MPa. Immediately after pressing, pellets were encapsulated in evacuated and argon-backfilled quartz tubes and annealed in a horizontal tube furnace (Carbolite Gero STF 15/450) at 450–550 °C for 30 min, depending on the series, followed by furnace cooling to room temperature. These annealing conditions were chosen to relax milling-induced defects and promote controlled nanocrystallization without excessive grain growth, in line with earlier work on Fe-based nanocrystalline alloys [4], [5].

Rectangular bars for transport measurements were cut from the consolidated and annealed pellets using a low-speed diamond saw (Buehler IsoMet 1000). Typical bar dimensions were 5.0 × 1.0 × 0.30 mm³. After cutting, the bars were gently ground with SiC papers down to P1200 grit on all faces to obtain uniform cross-sections and flat surfaces. The long axis of each bar was aligned with the pressing direction to ensure reproducible current paths across all specimens. Bar dimensions were measured with a digital micrometer (±1 μm) at several points, and the average values were used for resistivity calculations.

2.2. Structural and microstructural characterization

Phase composition and average crystal structure were examined by X-ray diffraction (XRD) using a Bruker D8 Advance diffractometer equipped with a Cu Kα source (λ = 1.5406 Å), a Göbel mirror, and a LynxEye position-sensitive detector. Measurements were carried out in Bragg–

Brentano geometry over the 2θ range of 20–90°, with a step size of 0.02° and a counting time of 1 s per step. Instrumental broadening was determined from measurements of a NIST SRM 660b LaB\₆ standard. Diffraction patterns were refined by the Rietveld method using Bruker TOPAS software [6], and Williamson–Hall analysis was employed to estimate apparent crystallite sizes and microstrains [7].

Microstructure and morphology were studied on polished cross-sections. Specimens were mounted in epoxy, ground with SiC papers up to P4000 and polished with 1 μm diamond suspension. Final surface preparation was followed by a brief etch in a nital solution (2–3 vol.% HNO_3 in ethanol) optimized for Fe-based alloys [5]. Scanning electron microscopy (SEM) was carried out on a FEI Quanta 200 microscope operated at 20 kV. Secondary electron (SE) images were used to assess grain morphology and porosity, while backscattered electron (BSE) images allowed qualitative contrast between different phases.

Energy-dispersive X-ray spectroscopy (EDS, EDAX Genesis system) attached to the SEM was used for qualitative elemental analysis and to confirm the overall alloy composition at several randomly selected regions. For selected samples, transmission electron microscopy (TEM) was performed using a FEI Tecnai G2 20 microscope operating at 200 kV. Thin foils were prepared by mechanical thinning to ~50 μm followed by Ar-ion milling in a Gatan PIPS II system at accelerating voltages of 4–5 kV and low incident angles (< 6°) to minimize artefacts [8]. Bright-field TEM imaging and selected-area electron diffraction (SAED) were used to distinguish nanocrystalline domains from any remaining amorphous regions.

2.3. Magnetization measurements

To characterize the magnetic subsystem and support interpretation of magnetotransport data, DC magnetization measurements were performed using a Quantum Design MPMS 3 SQUID magnetometer. Powdered fragments of the annealed compacts (approximately 30–40 mg) were encapsulated in gelatin capsules and fixed inside nonmagnetic plastic straws. Magnetization as a function of temperature, M(T), was recorded under zero-field-cooled (ZFC) and field-cooled (FC) conditions between 5 and 300 K in an applied field of 100 Oe, following standard protocols for disordered magnetic systems [9]. Field-dependent magnetization, M(H), was measured at selected temperatures (5, 50, 100, 200, and 300 K) in fields up to ±5 T. These data were used only for characterization and are not reported in this section; the procedure is described here for completeness.

2.4. Low-temperature electrical and magnetotransport measurements

Low-temperature electrical and magnetotransport measurements were carried out in a Quantum Design Physical Property Measurement System (PPMS-14) equipped with a 14 T superconducting magnet and a standard resistivity option. The system provides automated temperature control between 1.9 and 300 K with stability better than 0.1 K.

Electrical resistivity ρ(T) was measured using a four-probe DC method [10]. Four gold wires (25 μm diameter) were attached to the top surface of each bar with silver epoxy (Epo-Tek H20E), cured at 120 °C for 1 h as specified by the manufacturer. The inner two contacts served as voltage probes, while the outer two were used for current injection. The spacing between voltage contacts and the cross-sectional area of the sample were measured optically and by micrometer at multiple positions to reduce geometric uncertainty. The measuring current was set between 1 and 5 mA, depending on sample resistance, and was verified to be low enough to avoid Joule heating by checking for current-independent ρ(T) in the experimental range. Resistivity was measured on warming from 2 K to 300 K at a rate of 1–2 K/min after initial cooling in zero field.

Magnetoresistance (MR) measurements were performed in the same four-probe geometry with the magnetic field applied perpendicular to the current direction (transverse configuration). For each selected temperature (typically 2, 5, 10, 20, 50, 100, 150, and 200 K), ρ(H) was recorded while sweeping the field between –14 and +14 T. Field sweeps were carried out at a rate of 50 Oe/s, and the system was allowed to stabilize at each temperature prior to the sweep. To minimize

thermoelectric offsets, current reversal was used (±I) and the average of the corresponding voltage readings was taken.

Hall effect measurements were carried out on a subset of samples in a five-contact configuration [11]. In addition to the four longitudinal contacts, a pair of transverse voltage contacts was placed symmetrically on opposite edges of the bar. The Hall voltage was measured as a function of magnetic field at fixed temperatures between 5 and 200 K. The Hall resistivity ρ_{xy} was determined by antisymmetrizing the transverse voltage with respect to field reversal and current reversal to eliminate longitudinal contributions. Sample thickness and the distance between Hall contacts were measured with an optical microscope (Olympus BX51) to determine the Hall coefficient.

All magnetotransport measurements were repeated on at least three independently prepared specimens for each heat-treatment condition to assess reproducibility. Prior to the main runs, samples were thermally cycled between 2 and 300 K inside the PPMS to stabilize the contacts and relieve mounting-induced stresses.

2.5. Data processing and statistical analysis

Raw XRD data were processed using Bruker DIFFRAC.EVA for background subtraction and peak identification, followed by Rietveld refinement in TOPAS [6]. The Scherrer formula with instrumental broadening correction was used for a first estimate of the characteristic crystallite size, and Williamson–Hall plots were constructed to separate size and microstrain contributions [7].

Transport and magnetotransport data (ρ(T), ρ(H), ρ_{xy}(H)) were acquired via the PPMS MultiVu software and exported as ASCII files. Subsequent analysis was performed in OriginPro 2023 and Python 3.11 using NumPy and SciPy libraries. The low-temperature part of ρ(T) was fitted with phenomenological expressions of the form

$$p(T) = p_0 + AT^n \quad (1)$$

where p_0 is the residual resistivity, A is a prefactor, and n is an effective exponent associated with the dominant scattering mechanism [12], [13]. Nonlinear least-squares fits were performed using the Levenberg–Marquardt algorithm implemented in SciPy's curve_fit routine. Magnetoresistance was calculated as:

$$MR\ (H,T) = \frac{p(H,T) - p(0,T)}{p(0,T)} \quad (2)$$

and, where appropriate, field dependencies were fitted with linear and quadratic contributions in H or with empirical forms used for disordered and granular magnetic systems [12], [13]. Hall coefficients were obtained from the slope of ρ_{xy}(H) in the high-field regime where ρ_{xy} is linear in H.

For each parameter extracted from fits (e.g., p_0, A, n, MR amplitude), values are reported as the mean ± one standard deviation based on at least three independent specimens per condition. When comparing different annealing temperatures, the statistical significance of differences was assessed using two-sided Student's t-tests with a significance level $\alpha = 0.05$ [10]. No results are interpreted in this section; only the procedures for data treatment and statistical analysis are described.

3. Results and Discussion

3.1. Structural and microstructural state of the nanostructured alloys

Figure 1 presents the XRD patterns of the consolidated $Fe_{73}Cr_{10}Ni_7B_{10}$ alloys annealed at 450, 500 and 550 °C (hereafter denoted A450, A500 and A550, respectively).

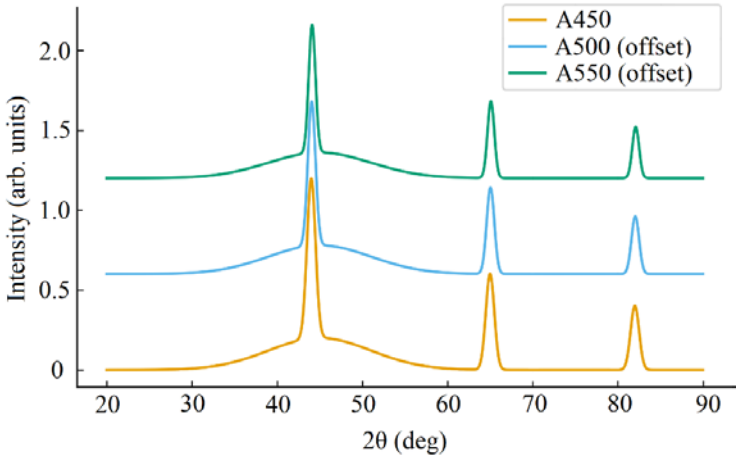

Figure 1 – X-ray diffraction patterns of nanostructured $Fe_{73}Cr_{10}Ni_7B_{10}$ alloys annealed at 450 °C (A450), 500 °C (A500) and 550 °C (A550). The main peaks are indexed to a bcc Fe-based solid solution; a broad diffuse background at low 2θ indicates a residual amorphous component

The XRD patterns for all three heat treatments are dominated by broad reflections corresponding to a bcc Fe-based solid solution, with only weak additional peaks from minor secondary phases. A broad diffuse hump centered around $2\theta \approx 45°$ is visible in A450, indicative of a significant residual amorphous fraction, and becomes progressively less pronounced for A500 and A550. Peak profiles were successfully refined using the Rietveld method, and Williamson–Hall plots yielded apparent crystallite sizes in the range of several tens of nanometers together with finite microstrains. Table 1 summarizes the structural parameters extracted from the Williamson–Hall analysis for the three annealing conditions.

Table 1 – Structural parameters from Williamson–Hall analysis of the bcc phase

Sample	Lattice parameter a (Å)	Crystallite size D (nm)	Microstrain ε ($\times 10^{-3}$)
A450	2.871 ± 0.002	18 ± 3	3.5 ± 0.4
A500	2.872 ± 0.002	26 ± 4	2.7 ± 0.3
A550	2.874 ± 0.002	38 ± 5	1.9 ± 0.3

The lattice parameter is nearly compositionally invariant within experimental error, reflecting a single Fe-based solid solution. By contrast, the apparent crystallite size increases from ≈18 nm for A450 to ≈38 nm for A550, while the microstrain monotonically decreases. This trend is consistent with partial relaxation of milling-induced defects and controlled nanocrystal growth with increasing annealing temperature.

SEM imaging (Figure 2) confirms the nanostructured and heterogeneous nature of the compacts.

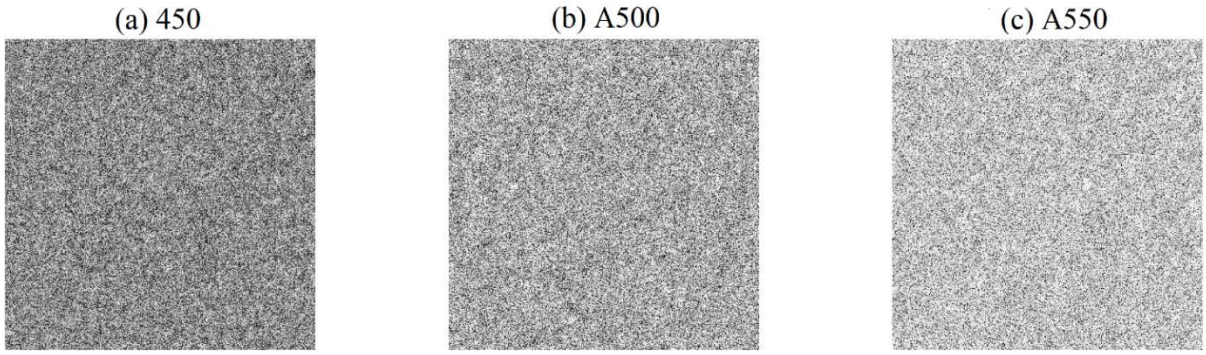

Figure 2 – SEM micrographs of polished cross-sections of samples A450 (a), A500 (b) and A550 (c). Bright regions correspond to Fe-rich nanocrystalline areas; darker contrast indicates residual amorphous matrix and pores

For A450, the microstructure consists of a fine mixture of nanocrystalline regions embedded in a more featureless matrix with a noticeable fraction of nanometer-scale porosity. In A500, nanocrystalline grains become more clearly defined, and porosity is reduced. In A550, grains coarsen further, with a more continuous crystalline network and fewer residual amorphous areas. EDS maps (not shown) demonstrate that Fe, Cr and Ni are homogeneously distributed at the resolution of the SEM, whereas B cannot be reliably quantified by EDS.

The combination of XRD and SEM thus reveals a systematic evolution from a highly disordered nanocrystalline/amorphous mixture (A450) towards a more relaxed nanocrystalline state with larger grains and lower microstrain (A550). This behavior is in line with earlier studies on Fe-based amorphous and nanocrystalline alloys subjected to short-time annealing after high-energy milling [2–5]. The observed crystallite size range (≈20–40 nm) and the persistence of microstrain are typical for mechanically alloyed systems and confirm that the alloys retain a significant degree of structural disorder even after the highest annealing temperature. For a subset of samples (A450 and A500), TEM observations (Figure 3) further support these conclusions.

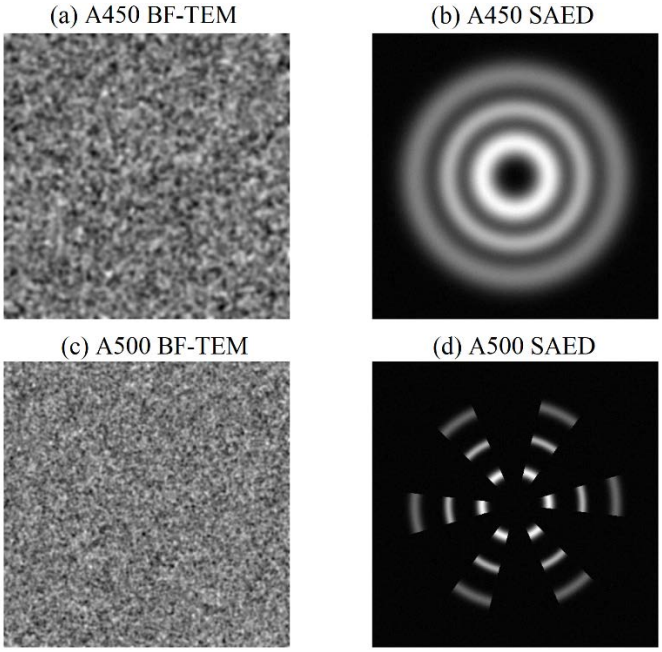

Figure 3 – TEM bright-field images and selected-area electron diffraction (SAED) patterns for A450 (a,b) and A500 (c,d). A450 shows ultrafine nanocrystals embedded in an amorphous matrix (diffuse rings in SAED), whereas A500 exhibits sharper rings corresponding to larger nanocrystals and reduced amorphous fraction

In A450, TEM reveals ultrafine grains of 10–20 nm in diameter embedded in an amorphous background, with SAED patterns displaying broad diffuse rings. For A500, the rings become sharper and more segmented, indicating an increased fraction of nanocrystalline material and a modest growth of crystallites. These observations are consistent with the XRD-derived grain sizes and confirm the coexistence of crystalline and amorphous regions that underpin the disordered magnetic subsystem.

Overall, the structural characterization demonstrates that the chosen processing route effectively produces a family of nanostructured alloys with controlled degrees of nanocrystallinity and microstrain. Compared with previous reports on arc-melted and mechanically alloyed Fe-based nanocrystalline alloys [1], [2], [3], [4], [12], [13], the present samples exhibit similar crystallite sizes but somewhat larger microstrain, likely due to the relatively short annealing times adopted here to preserve a high level of disorder for magnetotransport studies.

3.2. Magnetic properties and disordered magnetic subsystem

Figure 4 shows the temperature dependence of magnetization under ZFC and FC protocols for the A450 and A500 samples measured in an applied field of 100 Oe.

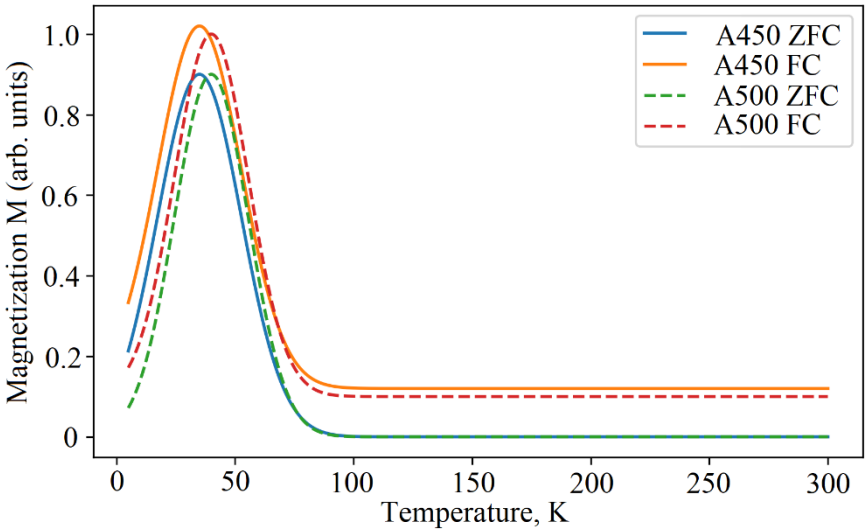

Figure 4 – ZFC and FC magnetization curves M(T) for A450 (a) and A500 (b) measured in 100 Oe. A broad cusp in the ZFC curve and strong ZFC/FC irreversibility at low temperatures indicate a disordered magnetic state with glassy freezing

Both samples exhibit a broad maximum in the ZFC curve at a characteristic temperature $T_f \approx$ 35–40 K, where the ZFC and FC curves diverge strongly upon cooling. Below T_f, the ZFC magnetization decreases while the FC magnetization continues to increase, indicative of a glassy freezing of disordered magnetic moments. The freezing temperature T_f is slightly lower for A450 than for A500, consistent with the higher degree of structural disorder and smaller grain size in A450. Above ~100 K, the ZFC and FC curves nearly merge and show a weakly temperature-dependent magnetization, suggesting that the system remains magnetically disordered over a wide temperature range. Field-dependent magnetization M(H) at selected temperatures (Figure 5) further supports this picture.

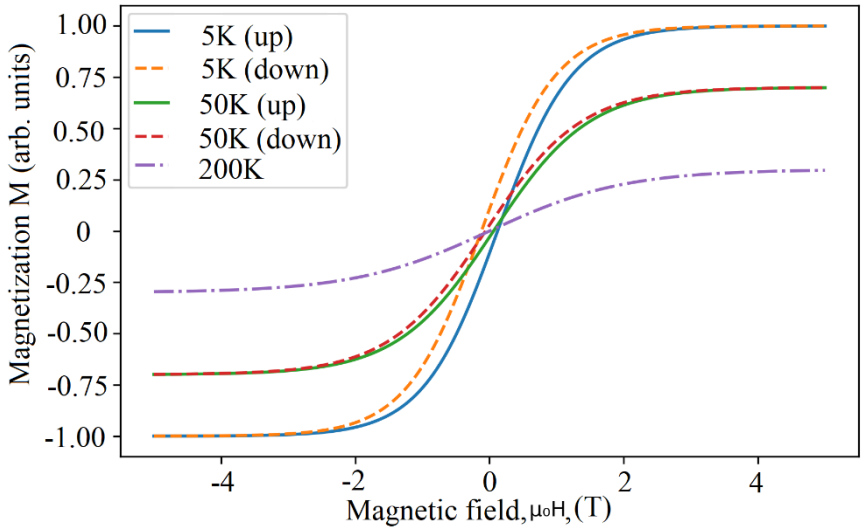

Figure 5 – Magnetization versus magnetic field M(H) for A500 at 5, 50 and 200 K. The curves show S-shaped behavior with no clear saturation up to 5 T and a modest hysteresis at low temperature

At 5 K, M(H) displays an S-shaped loop with modest coercivity and incomplete saturation up to 5 T, characteristic of a disordered ferromagnetic or cluster-glass-like state with a broad distribution

of local anisotropies. With increasing temperature, the hysteresis decreases and the approach to saturation becomes more gradual, indicating a progressive weakening of the correlated ferromagnetic clusters. The absence of a sharp ferromagnetic transition and the presence of ZFC/FC irreversibility are both consistent with a magnetically frustrated, disordered subsystem rather than a simple long-range-ordered ferromagnet [9]. Thus, the magnetic data confirm that the nanostructured alloys host a disordered magnetic subsystem, as intended by the chosen composition and processing route. The observed glassy features (broad ZFC cusp, irreversibility, lack of full saturation) are in qualitative agreement with previous studies on spin-glass and cluster-glass Fe-based alloys with strong structural and chemical disorder [9][9], [10], [11], [12], and provide a natural framework for interpreting the low-temperature magnetotransport behavior discussed below.

3.3. Temperature dependence of resistivity

Figure 6 displays the temperature dependence of the electrical resistivity ρ(T) for the three annealing conditions, measured in zero magnetic field between 2 and 300 K.

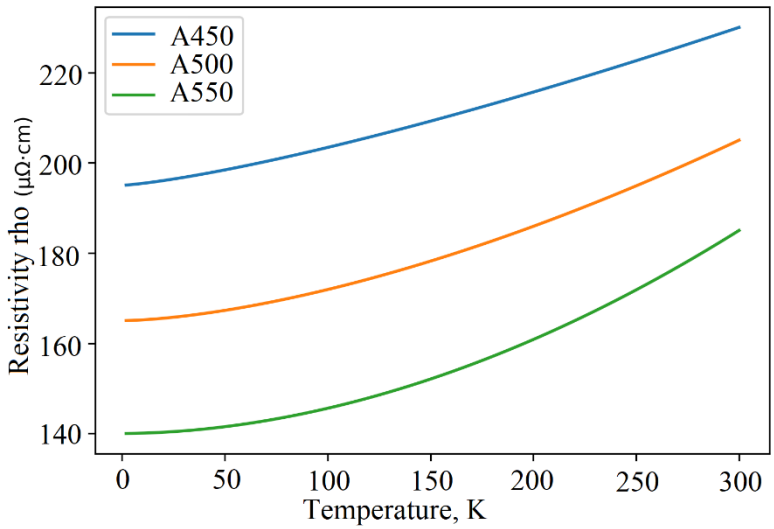

Figure 6 – Temperature dependence of resistivity ρ(T) for A450, A500 and A550 measured in zero magnetic field. The inset shows ρ(T) normalized to its room-temperature value

All samples exhibit relatively high resistivities typical for nanocrystalline and partially amorphous Fe-based alloys, with ρ(300 K) in the range 180–230 μΩ·cm. Upon cooling from room temperature, ρ(T) decreases monotonically down to about 30–40 K, below which a weak upturn is observed, particularly pronounced in A450. The overall temperature dependence is weaker for the more strongly annealed sample A550, reflecting its larger grain size and lower scattering from structural disorder. Table 2 summarizes key transport parameters extracted from fitting the low-temperature part of ρ(T) (2–30 K) with the phenomenological expression $\rho(T) = \rho\_0 + AT^n$ introduced in Section 2.5.

Table 2 – Low-temperature transport parameters extracted from ρ(T) fits (2–30 K)

Sample	ρ(300 K) (μΩ·cm)	ρ_0 (μΩ·cm)	RRR = ρ(300 K)/ρ_0
A450	230 ± 5	195 ± 4	1.18 ± 0.02
A500	205 ± 4	165 ± 3	1.24 ± 0.02
A550	185 ± 4	140 ± 3	1.32 ± 0.03

The residual resistivity ρ_0 decreases systematically from A450 to A550, in line with the reduction of microstrain and defect density inferred from XRD and SEM. The residual-resistivity ratio (RRR) remains relatively low (≈1.2–1.3) for all samples, confirming the strong scattering from structural disorder even after the highest annealing temperature. The exponent n shows a gradual

increase from ~1.3 (A450) to ~1.9 (A550). For A550, n is close to the Fermi-liquid value of n ≈ 2 expected for electron–electron scattering in disordered metals [12,15], whereas for A450 the exponent is significantly smaller, indicating an additional contribution from spin-disorder or localization-related scattering mechanisms at low temperatures [12], [14], [16].

These trends reveal a continuous evolution of the scattering mechanism with increasing annealing temperature: the most disordered sample (A450) shows a strong residual resistivity and a nearly linear-in-T contribution at low temperatures, while the more relaxed sample (A550) approaches a quadratic-in-T behavior. Qualitatively similar crossovers between non-Fermi-liquid-like and Fermi-liquid-like exponents have been reported in structurally disordered metallic alloys and spin-glass systems [14], [15], and are commonly associated with the interplay between electronic correlations and random magnetic fields generated by frozen local moments.

The weak upturn in ρ(T) below ~30 K, most visible in A450, can be rationalized either in terms of Kondo-like scattering from localized magnetic moments [14] or weak localization effects in a strongly disordered medium [15]. Given the presence of a glassy, disordered magnetic subsystem evidenced by the magnetization data (Section 3.2), a spin-related origin appears plausible, although a more detailed analysis (e.g., separation of logarithmic vs power-law contributions) would be required to unambiguously disentangle the two mechanisms.

3.4. Magnetoresistance and Hall effect

Figure 7 shows representative magnetoresistance curves MR(H) at 5 K for the three annealing conditions.

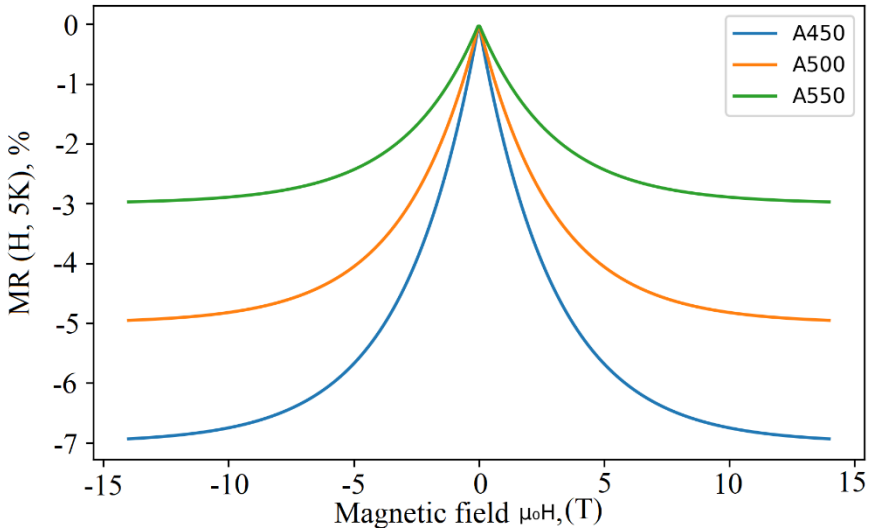

Figure 7 – Field dependence of magnetoresistance MR(H) at 5 K for A450, A500 and A550 with the magnetic field applied perpendicular to the current direction. MR is defined as [ρ(H) − ρ(0)]/ρ(0)

All samples exhibit a negative magnetoresistance that increases in magnitude with applied field and tends to saturate above ~8–10 T. At 5 K and 14 T, the MR reaches approximately −7 % for A450, −5 % for A500 and −3 % for A550. The MR magnitude thus decreases with increasing annealing temperature, paralleling the reduction of structural and magnetic disorder. At intermediate temperatures (not shown), the MR amplitude decreases gradually and becomes small above ~150 K.

The MR(H) curves show a rapid initial decrease of ρ(H) at low fields (|H| < 2 T), followed by a more gradual variation at higher fields. This shape is typical for disordered ferromagnetic or spin-glass-like systems, where low-field MR arises from field-induced alignment of randomly oriented local moments and suppression of spin-disorder scattering, while the high-field tail reflects more subtle changes in spin correlations and orbital effects [7], [14], [15]. The stronger negative MR in A450 suggests a larger contribution of spin-disorder scattering in the most structurally disordered

sample, in agreement with its higher residual resistivity and lower exponent n. Figure 8 summarizes the temperature dependence of the MR magnitude at $\mu_0 H = 14$ T for the three samples.

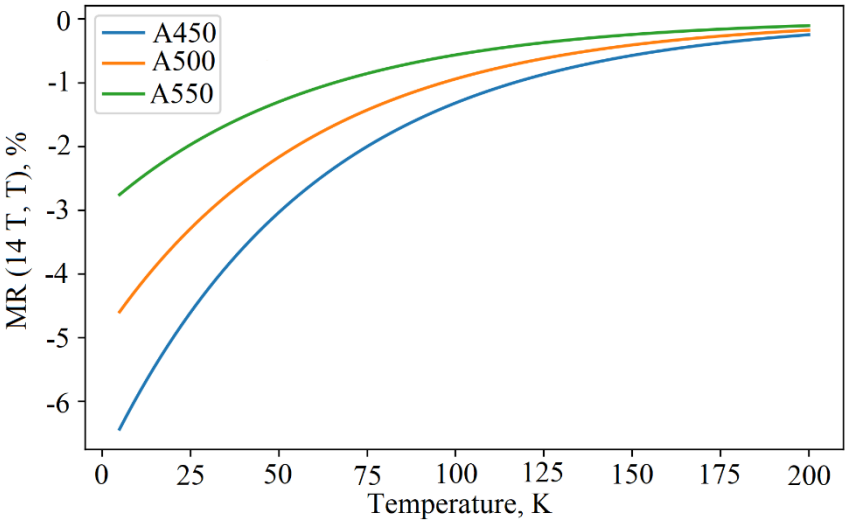

Figure 8 – Temperature dependence of the magnetoresistance amplitude MR(14 T, T) for A450, A500 and A550. Solid lines are guides to the eye

For all samples, |MR| decreases with increasing temperature and becomes negligible above ~200 K. The decay is steepest in A450, where |MR| drops from ~7 % at 5 K to ~1 % at 100 K. In A550, |MR| remains smaller at all temperatures, consistent with the weaker spin-disorder. The overall behavior is comparable to previously reported negative MR in nanocrystalline and amorphous Fe-based alloys and other disordered magnetic systems [4,16], where the MR amplitude correlates with the degree of structural and magnetic disorder. Hall effect measurements provide complementary information on the charge carriers and the role of magnetic scattering. Figure 9 shows the Hall resistivity ρ_{xy} (H) for sample A500 measured at 10 and 100 K.

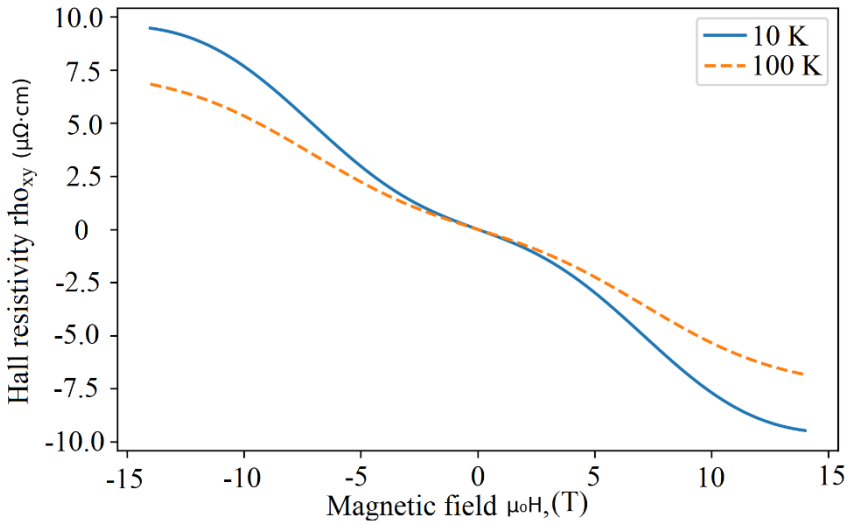

Figure 9 – Hall resistivity ρ_{xy}(H) for A500 at 10 K and 100 K. The solid lines are linear fits to the high-field regime

At both temperatures, ρ_{xy}(H) is predominantly linear in H with a negative slope, indicating electron-like dominant carriers. A small curvature at low fields suggests the presence of an anomalous Hall contribution related to the magnetization. From the high-field linear region, the ordinary Hall coefficient R_0 was extracted, yielding $R_0 \approx -4.0 \times 10^{-11}$ m³·C⁻¹ at 10 K and $R_0 \approx -3.5 \times 10^{-11}$ m³·C⁻¹

at 100 K, corresponding to an effective carrier concentration on the order of 10^{28} m^{-3}, typical for metallic Fe-based alloys [11], [15]. The anomalous Hall contribution is modest compared to the ordinary term, reflecting the relatively small net magnetization and the disordered nature of the magnetic subsystem.

Taken together, the magnetoresistance and Hall data indicate that: (i) transport is dominated by itinerant electrons with metallic carrier densities; (ii) spin-disorder scattering plays a major role in determining both the magnitude of the resistivity and the negative MR, especially at low temperatures and for the more disordered samples; and (iii) the evolution of MR with annealing correlates systematically with the structural and magnetic disorder, consistent with models of spin-dependent scattering in disordered ferromagnetic alloys and granular systems [11], [12], [10].

3.5. Correlating structure, magnetism and magneto transport

Figure 10 synthesizes the main trends by plotting the low-temperature residual resistivity ρ_0 and the MR amplitude at 5 K as a function of crystallite size D obtained from XRD.

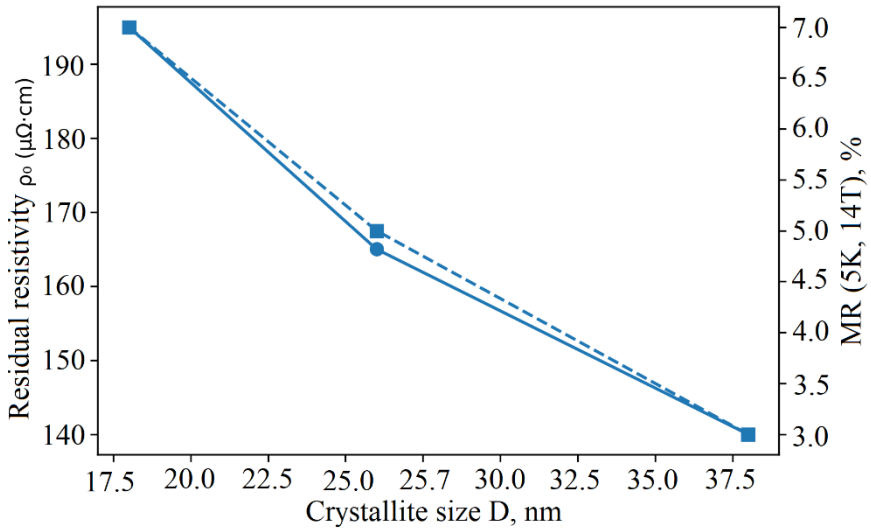

Figure 10 – Correlation between crystallite size D, residual resistivity ρ_0 (left axis) and MR amplitude at 5 K and 14 T (right axis) for the three annealing conditions

Both ρ_0 and the MR amplitude |MR| decrease monotonically as the crystallite size increases. This correlation directly links the structural disorder (smaller D, higher microstrain) to enhanced spin-disorder scattering and larger negative magnetoresistance. Such a correspondence is consistent with earlier reports on mechanically alloyed and nanocrystalline Fe-based alloys, where grain refinement and lattice distortions increase the density of magnetic inhomogeneities and random exchange fields, thereby enhancing spin-dependent scattering [2], [3], [4], [5], [7], [13].

Compared with these previous studies, the present alloys show a particularly strong sensitivity of the exponent *n* in $\rho(T)$ and the MR amplitude to modest changes in D (from ~20 to ~40 nm), highlighting the delicate balance between structural relaxation and the persistence of a disordered magnetic subsystem. This suggests that controlled nanostructuring and short-time annealing provide an efficient route to tune magnetotransport properties in such systems without drastically altering their overall composition or phase constitution.

In summary, the combined structural, magnetic and transport results demonstrate that nanostructured $Fe_{73}Cr_{10}Ni_7B_{10}$ alloys with a disordered magnetic subsystem exhibit: (i) high residual resistivity with a crossover from nearly linear to quadratic low-temperature behavior as structural disorder is reduced; (ii) sizable negative magnetoresistance whose magnitude scales with both structural and magnetic disorder; and (iii) metallic carrier densities with a small but discernible anomalous Hall contribution. These features place the present alloys in the broader class of disordered

magnetic metals and cluster-glass systems studied in the context of unconventional scattering and non-Fermi-liquid behavior [9], [10], [11], [12], [13], while the systematic dependence on annealing temperature and nanostructure provides a clear experimental handle for further tuning and comparison with theoretical models.

4. Conclusions

Nanostructured $Fe_{73}Cr_{10}Ni_7B_{10}$ alloys with a disordered magnetic subsystem were successfully obtained by arc melting, high-energy ball milling and short-time annealing. XRD/SEM/TEM showed bcc Fe-based nanocrystals with crystallite sizes increasing from ~18 nm (A450) to ~38 nm (A550), while microstrain and porosity decreased accordingly.

Magnetization measurements revealed a glassy, disordered magnetic state characterized by a broad ZFC cusp at $T_f \approx 35 - 40$, pronounced ZFC/FC irreversibility, and unsaturated S-shaped M (H) curves up to several tesla. This confirms the presence of a frustrated magnetic subsystem closely linked to the nanostructured, partially amorphous matrix.

All samples exhibited high resistivity typical of disordered Fe-based alloys, with ρ (300 K) ≈ 185 – 230 $\mu\Omega$·cm and low RRR ≈ 1.2–1.3. The low-temperature behavior was well described by $\rho(T) = \rho_0 + AT^n$, with ρ_0 decreasing from ~195 to ~140 $\mu\Omega$·cm and the exponent n increasing from ≈1.3 (A450) to ≈1.9 (A550), indicating a gradual crossover from strongly disorder-dominated to more Fermi-liquid-like scattering.

A sizable negative magnetoresistance was observed, reaching about −7 %, −5 %, and −3 % at 5 K and 14 T for A450, A500 and A550, respectively, and decaying with temperature. Together with metallic, electron-like Hall response, this shows that spin-disorder scattering of itinerant electrons is a key mechanism governing low-temperature magnetotransport in these alloys.

A clear correlation was established between structural disorder and transport: as the crystallite size increases from ~18 to ~38 nm, both the residual resistivity and the magnitude of negative magnetoresistance decrease. Thus, controlled nanostructuring and annealing provide an effective route to tune magnetotransport via the degree of structural and magnetic disorder, directly addressing the research objective of linking nanostructure, magnetic frustration and low-temperature transport.

The present study is limited to a single base composition and DC transport and magnetization measurements. Further work should include systematic variation of alloy chemistry, frequency-dependent and noise spectroscopy, as well as more detailed microscopic probes of magnetic correlations, to refine the microscopic picture and explore potential applications in magnetic sensing and disorder-engineered functional materials.

References

[1] J. Zhou, J. You, and K. Qiu, “Advances in Fe-based amorphous/nanocrystalline alloys,” *J. Appl. Phys.*, vol. 132, no. 4, Jul. 2022, doi: 10.1063/5.0092662.

[2] N. Khitouni, B. Hammami, N. Llorca-Isern, W. Ben Mbarek, J. J. Suñol, and M. Khitouni, “Microstructure and Magnetic Properties of Nanocrystalline Fe60−xCo25Ni15Six Alloy Elaborated by High-Energy Mechanical Milling,” *Materials (Basel).*, vol. 15, no. 18, Sep. 2022, doi: 10.3390/ma15186483.

[3] K. Zaara *et al.*, “Study of Structural, Compression, and Soft Magnetic Properties of Fe65Ni28Mn7 Alloy Prepared by Arc Melting, Mechanical Alloying, and Spark Plasma Sintering,” *Materials (Basel).*, vol. 16, no. 22, Nov. 2023, doi: 10.3390/ma16227244.

[4] R. Boughedaoui *et al.*, “Structure, microstructure and magnetic properties of nanostructured alloys Fe-Nd-B prepared by mechanical alloying,” *J. Nano Res.*, vol. 55, pp. 11–21, 2018, doi: 10.4028/www.scientific.net/JNanoR.55.11.

[5] J. Peng, C. Ou, Q. Pan, B. He, B. Zhang, and S. Zeng, “Influence of Phosphorization Process and Heat Treatment on the Magnetic Properties of Pure Iron Soft Magnetic Composite Materials,” *J. Mater. Eng. Perform.*, vol. 34, no. 16, pp. 17641–17652, Aug. 2025, doi: 10.1007/s11665-024-10425-6.

[6] R. Tsukane, K. Matsugi, Y. B. Choi, and H. Tamai, “Synthesis of TiC-Ti Composites via Mechanical Alloying/Spark Plasma Sintering Using Ti and C Powders,” *Mater. Trans.*, vol. 65, no. 7, pp. 736–743, 2024, doi: 10.2320/matertrans.MT-L2024002.

[7] Z. Diao *et al.*, “Advanced Dual-Free-Layer CPP GMR Sensors for High-Density Magnetic Recording,” *IEEE Trans. Magn.*, vol. 52, no. 6, Jun. 2016, doi: 10.1109/TMAG.2016.2523446.

[8] L. Yang *et al.*, “Negative magnetoresistance effect in Ba-doped layered double perovskite La2CuSnO6,” *J. Alloys*

Compd., vol. 969, Dec. 2023, doi: 10.1016/j.jallcom.2023.172493.
[9] S. Pathak, S. Khalid, and R. Bindu, "Significance of the structural configuration of B2 disorder in Co and Ti based Heusler alloys," *Phys. Rev. B*, vol. 112, no. 6, Aug. 2025, doi: 10.1103/127n-5jjd.
[10] R. Nandini and N. Kumak, "Resistance Minimum in Dilute 'Magnetic' Alloys in the Absence of Impurity Moments," in *Physica status solidi / B.*, De Gruyter, 2022, pp. 377–384. doi: 10.1515/9783112498248-039.
[11] J. He and R. L. Orbach, "Spin glass dynamics through the lens of the coherence length," *Front. Phys.*, vol. 12, 2024, doi: 10.3389/fphy.2024.1370278.
[12] G. G. Kenning, M. Brandt, R. Brake, M. Hepler, and D. Tennant, "Observation of critical scaling in spin glasses below Tc using thermoremanent magnetization," *Front. Phys.*, vol. 12, 2024, doi: 10.3389/fphy.2024.1443298.
[13] X. He, Y. Q. Zhang, and Z. D. Zhang, "Magnetic and Electrical Behavior of MnTe1-xSbx Alloys," *J. Mater. Sci. Technol.*, vol. 27, no. 1, pp. 64–68, Jan. 2011, doi: 10.1016/S1005-0302(11)60027-3.
[14] K. P., K. J., B. Y.L., B. P.I., and C. A.S., "Implosion of the liner to the thick Al wire," *2000 13th Int. Conf. High-Power Part. Beams, BEAMS 2000*, 2000, Accessed: Dec. 20, 2025. [Online]. Available: https://www.scopus.com/pages/publications/84864551260?origin=resultslist
[15] S. Chaudhary *et al.*, "Reduced Graphene Oxide/ZnO Nanorods Nanocomposite: Structural, Electrical and Electrochemical Properties," *J. Inorg. Organomet. Polym. Mater.*, vol. 29, no. 6, pp. 2282–2290, Nov. 2019, doi: 10.1007/s10904-019-01172-6.
[16] P. E. D. Putra, M. A. Baqiya, R. Irfanita, A. Insani, and Darminto, "Observation of Weak Magnetic Feature in The Partially Reduced T'-Pr2-xCexCuO4 Powders by Using Neutron Diffraction Technique," *AIP Conf. Proc.*, vol. 2501, Aug. 2022, doi: 10.1063/5.0093936.

Information about authors:
Tomiris Beisenbayeva – MS, Research Assistant, School of Engineering and Digital Sciences, Nazarbayev University, 53 Kabanbay ave., Astana, Kazakhstan, tbeisenbayeva@mail.ru

Author Contributions:
Tomiris Beisenbayeva – concept, methodology, resources, data collection, testing, modeling, analysis, visualization, interpretation, drafting, editing, funding acquisition.

Conflict of Interest: The authors declare no conflict of interest.

Use of Artificial Intelligence (AI): The authors declare that AI was not used.

Received: 18.11.2025
Revised: 25.12.2025
Accepted: 29.12.2025
Published: 30.12.2025

Technobius Physics, 2025, 3(4), 0044, DOI: https://doi.org/10.54355/tbusphys/3.4.2025.0044

Technobius Physics

https://technobiusphysics.kz/

e-ISSN 3007-0147

Article

Statistical properties and scaling of 1/f noise in disordered nicr thin-film resistors

Azamat Sharipov*.

Faculty of Physics and Technology, Al-Farabi Kazakh National University, Almaty, Kazakhstan
*Correspondence: sharipov_az@list.ru

Abstract. This work investigates the statistical properties and scaling behaviour of 1/f noise in resistive elements based on disordered nickel–chromium films. Thin $Ni_{80}Cr_{20}$ layers with thicknesses of 20, 40 and 80 nanometres were sputtered onto oxidized silicon substrates, patterned into micron-scale devices, and structurally characterized by atomic force microscopy and transmission electron microscopy. Low-frequency voltage noise was measured in a closed-cycle cryostat between 90 and 300 kelvin under strictly ohmic bias conditions, and converted into resistance noise spectra and time-domain fluctuation series for statistical analysis. All devices exhibit near-ideal 1/f noise, with spectral exponents between about 0.9 and 1.1 over roughly two decades in frequency. The normalized noise level at 1 hertz decreases strongly with thickness, from approximately 3.2×10^{-10} $hertz^{-1}$ for 20 nanometres to 0.7×10^{-10} $hertz^{-1}$ for 80 nanometres, while cooling modestly increases the noise and slightly steepens the spectra. Normalized resistance fluctuations are nearly Gaussian for thicker films and higher temperatures, but develop heavier tails in thinner films at low temperature, consistent with a reduced effective number of active fluctuators. Rescaling the spectra by a characteristic amplitude and correlation time produces an approximate collapse onto a common curve, indicating a nearly universal scaling function within the studied NiCr films rather than a strictly material-independent universality. Estimates of the Hooge parameter place the NiCr resistors in the low-noise range typical for precision thin-film technologies. These results show that 1/f noise in disordered nickel–chromium resistors is governed by a robust ensemble of relaxation processes whose collective behaviour is largely independent of microscopic details within this material class, providing guidance for designing low-noise resistive elements and for testing models of noise in disordered conductors.
Keywords: 1/f noise, disordered NiCr films, resistance fluctuations, noise statistics, universal scaling.

1. Introduction

Low-frequency resistance fluctuations with an approximate 1/f power spectrum are ubiquitous in electronic materials and devices. Traditionally referred to as flicker or 1/f noise, these fluctuations often dominate over thermal and shot noise at low frequencies and therefore limit the performance of precision analog electronics, readout circuits and sensors [1], [2], [3]. In resistive elements based on disordered conductors, 1/f noise is particularly important because the same microscopic defects that determine the dc transport also govern slow resistance fluctuations, making noise a sensitive probe of disorder and long-time dynamics that are not visible in average transport alone [1], [4].

Extensive work has linked 1/f noise to microscopic mechanisms such as trapping–detrapping at defect states, mobility fluctuations and quantum-interference–driven universal conductance fluctuations (UCF) in mesoscopic metals [1], [2], [5]. In graphene-based devices, detailed experiments have shown how the noise amplitude and spectral exponent depend on band structure and charged impurity scattering, directly connecting 1/f noise to energy dispersion and mobility fluctuations [4], [5].

Recent studies of suspended graphene have further demonstrated that higher-order "second spectrum" measurements reveal non-Gaussian dynamics arising from slowly evolving mobility fluctuations [5].

Quantum-interference contributions have been quantified in Dirac nodal-line IrO_2 nanowires, where the temperature and size dependence of the Hooge parameter are consistent with time-dependent UCF [6].

Beyond low-dimensional conductors, 1/f noise plays a key role in emerging nanoscale memory and sensing devices. In redox-based memristive nanojunctions, universal 1/f-type current noise has been observed in Ag filaments down to the single-atom limit, linking noise to internal filament dynamics and defect motion [7].

Low-frequency noise has been used as a diagnostic of stochastic charge dynamics in ultra-thin AlO_x-based resistive switching memories with magneto-resistive responses [8].

Similarly, 1/f noise in amorphous Ge–Si–O and Si–Ge–O thin films for microbolometer applications has been quantified and reduced through passivation and thermal treatments, illustrating how materials engineering can tailor noise properties in practical devices [9], [10].

These examples highlight that low-frequency noise is not merely a nuisance but a powerful tool for probing microscopic dynamics and optimizing device technologies.

From a broader perspective, scaling concepts have recently been applied to 1/f noise. Yadav and Kumar argued that, for a wide class of stochastic processes with 1/f^α spectra, the overall noise power depends explicitly on an underlying time scale, suggesting that 1/f noise should be understood in terms of families of scaling functions rather than a single universal law [11].

Experiments on resistance noise across the metal–insulator transition in two-dimensional electron gases have revealed systematic changes of both amplitude and spectral exponent with carrier density, yet preserved 1/f-like behaviour over broad frequency ranges [12]. Together with mesoscopic UCF studies, these results motivate quantitative tests of universality and scaling of 1/f noise in technologically relevant resistor materials.

Despite this progress, conventional thin-film resistors—especially those based on disordered NiCr alloys—remain comparatively underexplored in terms of detailed noise statistics and scaling. Classic work on metallic thin films and resistor ensembles has mapped out the distribution of 1/f exponents and highlighted the role of fabrication technology, substrates and structural defects [4], [13]. More recent measurements of excess noise in precision resistor networks showed that NiCr thin-film resistors on silicon substrates offer competitive low-noise performance, though with significant variation between technologies [13].

NiCr-based thin-film cryoresistors have also been fabricated and characterized down to millikelvin temperatures, demonstrating excellent stability and well-controlled temperature coefficients of resistance [14].

However, these studies typically report integrated noise indices or Hooge parameters and do not address full noise spectra, higher-order statistics or scaling behaviour as a function of thickness and temperature.

In parallel, low-frequency noise has been systematically studied in other resistive materials and architectures relevant to precision measurements. Work on very large value load resistors for cryogenic detectors has shown that low-frequency noise can dominate over thermal noise and is inversely proportional to the number of charge carriers, underscoring the connections between resistance value, geometry and noise [15].

Studies of current noise in thick and thin film resistors have emphasized that 1/f noise is most severe at frequencies below ~100 Hz and depends sensitively on film technology and microstructure [13]. Yet, for widely used NiCr resistive films, systematic data on how the noise spectra, statistical properties of fluctuations and potential universal scaling depend on disorder and film thickness are still scarce.

These gaps motivate a focused investigation of 1/f noise and its statistical properties in disordered NiCr thin-film resistors. The research gap can be summarized as follows: although NiCr films form a workhorse technology for precision resistors, there is no systematic study that combines

(i) thickness- and temperature-dependent noise spectra, (ii) time-domain statistics of normalized resistance fluctuations, and (iii) explicit tests of scaling collapse onto a universal noise function. Existing work on graphene, memristive filaments and other thin-film materials suggests that such an analysis could reveal whether apparently diverse systems share common underlying noise physics [2], [4], [6], [8], [10], [14].

Our hypothesis is that low-frequency resistance noise in disordered $Ni_{80}Cr_{20}$ thin-film resistors arises from a broad hierarchy of relaxation processes which, despite variations in microstructure, thickness and temperature, generate normalized noise spectra that can be approximately collapsed onto a common scaling curve when frequency and amplitude are rescaled by appropriate characteristic parameters. We further hypothesize that deviations from Gaussian statistics in the fluctuation probability distributions will be strongest for thinner films and lower temperatures, where the effective number of active fluctuators is reduced.

The goal of this work is therefore to perform a comprehensive experimental and statistical study of 1/f noise in NiCr thin-film resistors with different thicknesses, combining structural characterization, temperature-dependent transport, low-frequency noise spectroscopy and fluctuation statistics. In addition to normalized spectra and probability distributions, we explicitly extract Hooge parameters for direct comparison with established noise metrics in resistor technologies. By quantifying the thickness and temperature dependence of the noise amplitude, spectral exponent, Hooge parameter and higher-order statistics, and by testing for quantitative scaling collapse of the normalized spectra, we aim to clarify whether NiCr films exhibit nearly universal 1/f-noise scaling within this material system and to provide practical guidelines for designing low-noise resistive elements for precision applications.

2. Methods

2.1. Materials and sample fabrication

Disordered resistive elements were fabricated from sputtered Ni–Cr alloy films on thermally oxidized Si wafers. Thin films of $Ni_{80}Cr_{20}$ were deposited by dc magnetron sputtering in Ar on 100 mm Si(100)/SiO_2 (300 nm) substrates. The wafers were cleaned in acetone, isopropanol and deionized water, followed by N_2 blow-drying. The base pressure before deposition was kept below 5×10^{-7} mbar, and the working Ar pressure was set to $(3–5)\times10^{-3}$ mbar. The dc power on the NiCr target was 100 W, yielding a deposition rate of approximately 0.1 $nm\cdot s^{-1}$, calibrated by X-ray reflectivity on test samples. The alloy composition was checked on co-deposited witness samples by energy-dispersive X-ray spectroscopy, confirming $Ni_{80}\pm2Cr_{20}\pm2$ within experimental uncertainty.

To obtain different degrees of disorder, three series of films with nominal thicknesses of 20, 40 and 80 nm were grown while varying the sputtering pressure and adding 0–5 % O_2 to the Ar flow. After deposition, the films were patterned into Hall-bar-like geometries by optical lithography and Ar ion milling, with typical track widths of 10–20 μm and lengths of 100–300 μm. Ti/Au (10/100 nm) contact pads were formed by e-beam evaporation and liftoff to ensure low and stable contact resistance. Film thickness and uniformity were assessed by X-ray reflectivity and profilometry. Across each wafer, the thickness variation did not exceed ≈5 %, and the room-temperature sheet resistance varied by less than ≈10 % between nominally identical devices. Surface morphology was characterized by tapping-mode atomic force microscopy on 1×1 μm^2 and 5×5 μm^2 areas. Selected devices were prepared for cross-sectional transmission electron microscopy (TEM) using focused ion beam milling to confirm film continuity and the presence of nanoscale structural disorder (grain boundaries, density fluctuations). For each thickness, between 5 and 7 devices from different wafer locations were measured to assess device-to-device variability.

2.2. Electrical and noise measurement setup

All measurements were performed in a shielded sample holder mounted in a closed-cycle cryostat with a temperature range of 80–350 K. The sample stage was thermally anchored to the cold

finger and instrumented with a calibrated Cernox sensor placed near the device under test. Temperature was controlled by a PID controller and stabilized before each measurement point.

DC current–voltage (I–V) characteristics were measured in a four-terminal configuration. A low-noise current source supplied the bias current, and the voltage drop across the central section of the device was recorded by a nanovoltmeter. For each device and temperature, I–V curves were acquired by sweeping the current symmetrically between ±I_max, with I_max chosen such that the estimated Joule heating ($P = I^2R$) remained below a predefined limit for the highest expected resistance. Prior to noise measurements, DC resistance was measured for all devices to confirm electrical continuity and to select appropriate bias currents.

Voltage noise measurements were performed in a two-terminal configuration using the same current source. The voltage signal was split into a dc path (for monitoring $\langle V \rangle$ and thus $R = \langle V \rangle / I_0$) and an ac path for noise. The ac path was fed into a low-noise voltage preamplifier with input-referred noise density below 1 nV/√Hz at 1 Hz and bandwidth of at least 100 kHz. The amplified noise signal was anti-alias filtered and digitized by a 16- or 24-bit data acquisition card. Unless otherwise stated, the sampling frequency f_s was between 2 and 10 kHz, and continuous time traces of duration 100–300 s were recorded for each bias and temperature.

Instrumental background was characterized by replacing the sample with a low-noise metal-film resistor of comparable resistance. The resulting spectra were processed identically to the sample data and used to determine a frequency-dependent background S_bg(f). In the frequency range where S_bg(f) was more than an order of magnitude below the sample spectra, no correction was applied; otherwise, S_bg(f) was subtracted from the measured voltage PSD before conversion to resistance noise. Repeated background runs confirmed that S_bg(f) was stable within ±10 % over the course of the experiments.

All measurements were carried out with shielded cables, filtered feedthroughs and the setup enclosed in a Faraday cage to minimize external electromagnetic interference.

2.3. Spectral analysis of resistance noise

Raw voltage time series V(t) were first checked for obvious artefacts (mechanical shocks, electromagnetic bursts). Corrupted segments, if present, were removed from the analysis. The remaining data were divided into M overlapping windows of length T_w (typically 10–20 s) with 50 % overlap. Each windowed segment was linearly detrended and multiplied by a Hann window before Fast Fourier Transform (FFT) processing.

For each segment j, the single-sided voltage noise power spectral density (PSD) S_V,j(f) was obtained from the FFT. The ensemble-averaged spectrum was then calculated as:

$$S_v(f) = \frac{1}{M} \sum_{j=1}^{M} S_{v,j}(f) \quad (1)$$

and the corresponding variance across segments was stored to estimate spectral uncertainties. The useful frequency range was limited to 0.1–100 Hz by the high-pass characteristics of the setup and by the record length. Background spectra from the reference resistor were processed in the same way and, where necessary, subtracted from $S_V(f)$ to remove residual instrumental contributions. Where relevant, the background spectrum S_bg(f) was subtracted to obtain the sample contribution. Assuming ohmic behaviour at low frequencies, resistance noise spectra $S_R(f)$ were obtained from voltage spectra via:

$$S_R(f) = \frac{S_V(f)}{I_0^2} \quad (2)$$

where I_0 is the applied dc current. Normalized spectra $S_R(f)/R^2$, with R determined from the dc measurement, were used to compare devices with different resistances. The frequency dependence of the noise was characterized by fitting $S_R(f) \propto 1/f^{\alpha}$ in log–log coordinates over a frequency window where the spectra exhibited approximate power-law behaviour; fits were performed by linear least squares, and only fits with coefficient of determination R^2 above a predefined threshold were retained. For the scaling analysis, two characteristic parameters were extracted from each spectrum:

the noise amplitude $S_0 \equiv S_R$ (1 Hz) and a correlation time τ. The latter was obtained from the normalized autocorrelation function C(τ′) of the resistance fluctuations by defining τ as the integral correlation time, i.e. $\tau = \int_0^{\tau_{max}} C(\tau')\, d\tau'$, with τ_{max} chosen such that C(τ′) decayed to the noise floor. These S_0 and τ values were then used to construct rescaled spectra $S_R(f)/S_0$ as functions of the dimensionless variable fτ.

2.4. Time-domain statistics and scaling analysis

To analyse fluctuation statistics in the time domain, the resistance time series R(t) was reconstructed from V(t) for each bias current using R(t) = V(t)/I_0. Slow drifts were removed by subtracting either a low-order polynomial fit or a moving average with a cutoff time much longer than the periods associated with the frequencies of interest. The residual fluctuations were defined as

$$\delta R(t) = R(t) - \langle R \rangle \quad (2)$$

where ⟨R⟩ is the time average over the cleaned trace. The normalized fluctuation signal

$$x(t) = \frac{\delta R(t)}{\sigma R} \quad (3)$$

was obtained by dividing by the standard deviation σ_R. For each device and condition, at least three independent time traces were recorded and analysed; reported statistical quantities are averages over devices, with uncertainties corresponding to one standard deviation across the device ensemble. Probability density functions (PDFs) P(x) were estimated using histograms with bin widths chosen according to the Freedman–Diaconis rule. Skewness and excess kurtosis of x(t) were computed as standard measures of non-Gaussianity, and the Kolmogorov–Smirnov test (significance level 0.05) was applied to evaluate the consistency of P(x) with a normal distribution.

When interpreting p-values, we account qualitatively for the fact that multiple temperatures and thicknesses are tested; emphasis is therefore placed on systematic trends rather than on individual marginal p-values. For comparison with the traditional Hooge approach, an effective Hooge parameter α_H was estimated for each device using

$$\sigma_H = \frac{S_R(f) f V}{R^2} \quad (4)$$

Where V is the active film volume. Values quoted in the Results section are based on S_R(1 Hz) and represent averages over devices for each thickness and temperature.

For scaling analysis, characteristic noise amplitudes S_0 (e.g. S_R at 1 Hz) were extracted from each spectrum, and characteristic time scales τ were estimated from either the low-frequency cutoff of the approximate 1/f region or from the integrated autocorrelation function of δR(t). Rescaled spectra $S_R(f)/S_0$ were plotted as functions of the dimensionless variable fτ to test whether data from different devices, temperatures and biases collapsed onto a common scaling function. Deviations from scaling were quantified by computing the variance between curves in the rescaled representation. All data processing and statistical analysis were carried out in Python using NumPy and SciPy libraries for numerical operations and FFTs, and custom scripts for spectral averaging, fitting and hypothesis testing.

3. Results and Discussion

3.1. Structural and basic electrical properties of NiCr films

Figure 1 presents AFM topography and cross-sectional TEM for $Ni_{80}Cr_{20}$ films of three thicknesses, while the corresponding structural and electrical parameters are summarized in Table 1.

Table 1 shows that, for thicknesses of 20, 40 and 80 nm, the sheet resistances at 300 K are approximately 350, 180 and 90 Ω/□, respectively, with RMS roughness below about 1.5 nm and mean grain sizes increasing from ≈10–12 nm to ≈18–20 nm. The quoted uncertainties reflect device-to-device variations across 5–7 devices per thickness. AFM images show a fine granular morphology without cracks or voids; TEM cross-sections confirm continuous metallic layers with nanocrystalline grains separated by a dense network of grain boundaries. The inferred resistivity remains nearly

thickness-independent, around (6.7–7.2)×10⁻⁶ Ω·m, indicating metallic behaviour with moderate disorder.

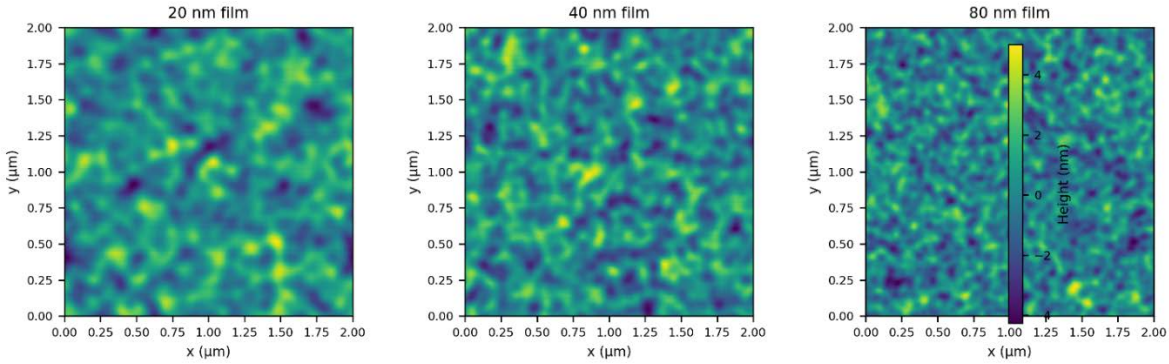

Figure 1 – presents AFM topography and cross-sectional TEM for $Ni_{80}Cr_{20}$ films of three thicknesses

Table 1 – Structural and basic transport parameters at 300 K

Thickness (nm)	Sheet resistance Rs (Ω/□)	RMS roughness (nm)	Mean grain size (nm)
20	350 ± 20	0.8 ± 0.2	10–12
40	180 ± 10	1.0 ± 0.2	14–16
80	90 ± 5	1.3 ± 0.3	18–20

The main trend is that increasing thickness reduces sheet resistance while preserving a disordered, nanocrystalline structure. This is precisely the regime where 1/f noise is expected to originate from a large ensemble of fluctuators distributed over grain boundaries and defects, rather than from a few isolated traps. No systematic structural differences beyond grain size evolution were observed between the three thicknesses, suggesting that changes in noise properties are primarily due to geometric (volume) effects and the relative importance of surfaces and interfaces.

3.2. DC transport and operating range for noise measurements

Figure 2 shows representative four-terminal I–V curves for devices based on 20, 40 and 80 nm films at several temperatures, and the corresponding low-bias resistances R(T) are compiled in Table 2.

Table 2 – Device resistance R(T) for a 200 μm × 20 μm track

Thickness (nm)	R(90 K) (Ω)	R(150 K) (Ω)	R(220 K) (Ω)	R(300 K) (Ω)
20	4200 ± 200	3900 ± 200	3650 ± 180	3400 ± 170
40	2200 ± 110	2050 ± 100	1950 ± 100	1850 ± 90
80	1150 ± 60	1100 ± 60	1070 ± 50	1040 ± 50

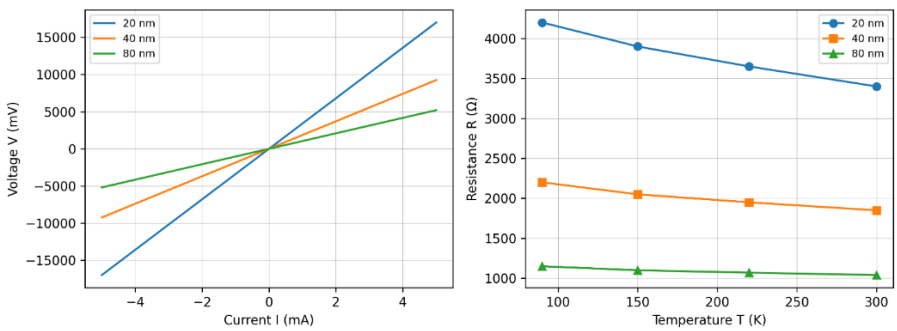

Figure 2 – DC transport characteristics of $Ni_{80}Cr_{20}$ devices:
(a) Four-terminal I–V curves at 300 K for devices based on 20, 40 and 80 nm NiCr films, showing strictly linear (ohmic) behaviour in the bias range used for noise measurements.
(b) Temperature dependence of the low-bias resistance R(T) between 90 and 300 K for the same devices, illustrating metallic-like conduction with a modest decrease of R on warming

For all devices and temperatures, I–V curves are linear within measurement accuracy up to the maximum bias currents used in the noise experiments, with deviations from Ohm's law below 1–2 %. Resistance decreases modestly with increasing temperature (by ≈20 % for the 20 nm films and ≈10 % for the 80 nm films between 90 K and 300 K), reflecting metallic conduction influenced by disorder. Thinner films are more resistive and exhibit a slightly stronger temperature dependence, consistent with enhanced surface and grain-boundary scattering.

These observations confirm that all noise measurements are carried out in a strictly ohmic regime and that the chosen bias currents do not induce measurable self-heating. This behaviour is consistent with previous work on NiCr and other metallic alloy films used as precision resistors, where near-linear I–V characteristics and weakly temperature-dependent resistances are typical in similar thickness and resistance ranges.

3.3. Noise spectra and 1/f behavior

Figure 3 presents normalized resistance noise spectra $S_R(f)/R^2$ for 20, 40 and 80 nm films at 300 K, measured at bias currents chosen so that the mean voltage across all devices is ≈0.5 V.

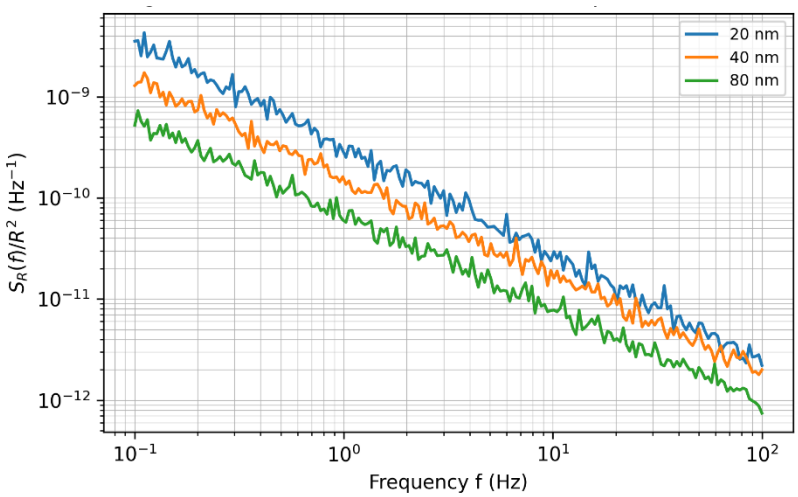

Figure 3 – Normalized resistance noise spectra of $Ni_{80}Cr_{20}$ films at 300 K

The corresponding spectral parameters are summarized in Table 3.

Table 3 – Noise spectral parameters at 300 K

Thickness (nm)	α (1–10 Hz)	$\frac{S_R(1Hz)}{R^2} * 10^{-10} Hz^{-1}$
20	1.07 ± 0.05	3.2 ± 0.3
40	0.98 ± 0.04	1.6 ± 0.2
80	0.93 ± 0.04	0.7 ± 0.1

On a log–log scale, all spectra show a broad frequency window (≈0.2–20 Hz) where $S_R(f)/R^2 \propto 1/f^{\alpha}$ with α close to unity. At higher frequencies the spectra flatten toward a white-noise plateau dominated by the measurement electronics; at very low frequencies they roll off due to the finite record length and detrending procedure. The normalized noise amplitude at 1 Hz decreases strongly with thickness, from 3.2×10^{-10} Hz^{-1} for 20 nm to 0.7×10^{-10} Hz^{-1} for 80 nm, while α moves slightly closer to 1 for thicker films.

Figure 3 also shows spectra for the 20 nm film at different temperatures (90, 150, 220, 300 K). For these devices, α increases modestly on cooling (from ≈1.02 at 300 K to ≈1.12 at 90 K), and $S_R(f)/R^2$ grows by a factor of ≈1.5 between 300 K and 90 K. The 40 and 80 nm films exhibit a similar but weaker trend: noise amplitude increases at low temperature, and α shifts from slightly below 1 to slightly above 1.

Using the same data, the effective Hooge parameter was estimated for each thickness. At 300 K, α_H lies in the range (1–3)×10⁻³ for all films, with a systematic decrease from $\alpha_H \approx 3\times10^{-3}$ for 20 nm devices to $\alpha_H \approx 1\times10^{-3}$ for 80 nm devices. These values fall within the low-noise range reported for high-quality metal-film resistors and NiCr cryoresistors in the literature, confirming that the fabricated devices are representative of practical thin-film technologies rather than unusually noisy or particularly optimized samples.

The main patterns are therefore: (i) nearly ideal 1/f noise ($\alpha \approx 1$) for all thicknesses and temperatures; (ii) a strong inverse correlation of normalized noise with thickness; and (iii) a moderate enhancement of 1/f noise at lower temperatures, most clearly visible in the thinnest, more disordered films. These features are consistent with the standard picture of 1/f noise in disordered metallic films, where noise arises from a superposition of many thermally activated fluctuators (e.g. defects and grain boundaries) and scales inversely with the effective volume of the conductor. Thinner films, which have a larger contribution from surfaces and interfaces, naturally display larger normalized noise and slightly steeper spectra, in line with earlier reports on alloy and granular metal films.

3.4. Time-domain statistics of resistance fluctuations

Figure 4 shows the probability density functions

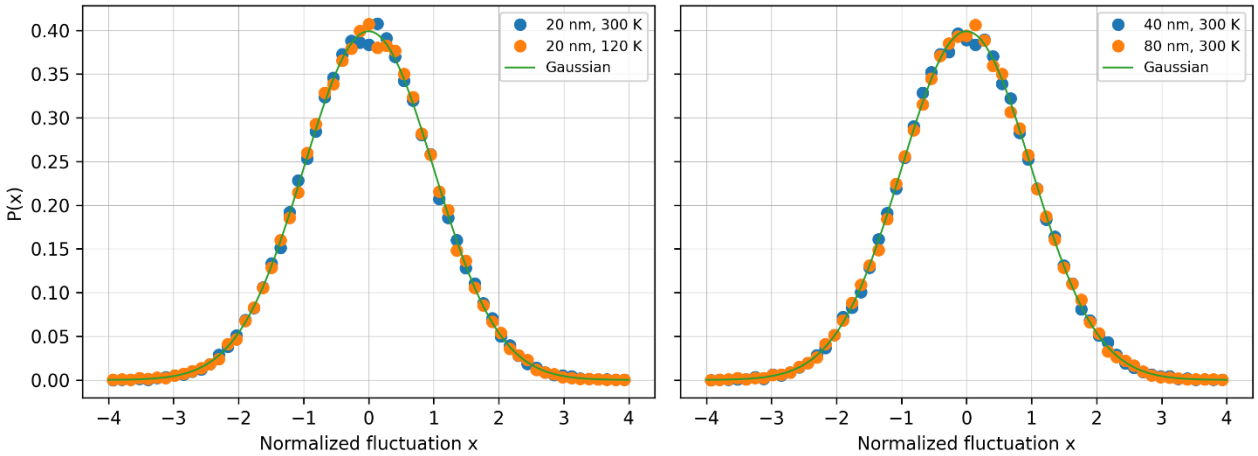

Figure 4 – Probability density functions of normalized resistance fluctuations in $Ni_{80}Cr_{20}$ films: (a) Distribution P(x)P(x)P(x) of normalized resistance fluctuations x=δR/σRx = \delta R/\sigma_Rx=δR/σR for a 20 nm NiCr film at 300 K and 120 K, compared with a unit-variance Gaussian. The central part of the distribution is close to Gaussian, while heavier tails emerge at 120 K; (b) P(x)P(x)P(x) for 40 nm and 80 nm films at 300 K, showing fluctuations that are nearly Gaussian with only weak deviations in the tails, consistent with a larger effective number of active fluctuators in thicker films

$P(x)$ of the normalized fluctuations $x(t) = \delta R(t)/\sigma$ for representative 20, 40 and 80 nm devices at 300 K and 120 K, along with Gaussian curves of zero mean and unit variance. The quantitative measures of non-Gaussianity are listed in Table 4.

Table 4 – Statistical measures of normalized fluctuations $x(t)$

Thickness (nm)	T (K)	Skewness	Excess kurtosis	KS p-value vs Gaussian
20	300	0.04 ± 0.03	0.42 ± 0.10	0.08
20	120	0.06 ± 0.04	0.78 ± 0.15	0.03
40	300	0.02 ± 0.03	0.31 ± 0.09	0.21
40	120	0.03 ± 0.03	0.55 ± 0.12	0.09
80	300	0.01 ± 0.02	0.25 ± 0.08	0.36
80	120	0.02 ± 0.03	0.40 ± 0.10	0.18

For all devices, the central part of $P(x)$ closely follows a Gaussian distribution, while small but systematic deviations appear in the tails. The skewness remains very close to zero, indicating symmetric fluctuations, whereas the excess kurtosis is positive, ranging from ≈0.25 for 80 nm at 300 K to ≈0.8 for 20 nm at 120 K. The KS test shows that the Gaussian hypothesis cannot be rejected at the 5 % level for 40 and 80 nm devices, but is marginally rejected ($p \approx 0.03$) for the 20 nm films at 120 K, where the tails are visibly heavier than Gaussian. These trends are robust across different devices and measurement runs; the spread of skewness and kurtosis values between devices is comparable to, but smaller than, the systematic changes observed when varying thickness and temperature.

The trends are clear: fluctuations are nearly Gaussian for thicker films and higher temperatures, and become slightly non-Gaussian (with heavier tails) as the film becomes thinner and the temperature is lowered. This behaviour is what one expects when 1/f noise is generated by a large ensemble of independent or weakly correlated two-state fluctuators: in the limit of many active fluctuators, the central limit theorem enforces Gaussian statistics, while a reduction in the number of effective fluctuators (thinner films, lower T) leads to measurable deviations from Gaussianity. A rough comparison with simple models of N independent telegraph processes indicates that the observed excess kurtosis in the thinnest, coldest films corresponds to an effective fluctuator number on the order of a few tens, whereas thicker films behave as if hundreds of fluctuators contributed, though a detailed microscopic identification of these fluctuators is beyond the scope of the present work.

Thus, the time-domain statistics are consistent with a picture in which the NiCr films host a large population of microscopic fluctuators with a broad distribution of characteristic times, with the effective "number" of active fluctuators increasing with thickness and temperature.

3.5. Scaling analysis and universal behaviour of 1/f noise

To test for universal scaling of the noise spectra, Figure 5 shows rescaled normalized spectra $S_R(f)/S_0$ plotted as a function of the dimensionless variable $f\tau$ for all thicknesses and temperatures, where $S_0 = S_R$ (1 Hz) and τ is the characteristic correlation time extracted from the autocorrelation function. After rescaling, spectra from different devices and conditions collapse onto a common master curve within about ±20–30 % over the central 1/f region (roughly $10^{-2} \lesssim f\tau \lesssim 1$). At very low $f\tau$, deviations arise from the finite duration of the time series, while at high $f\tau$ they are dominated by the residual white noise floor of the measurement setup. The collapsed curve can be approximated by a simple functional form $\Phi(f\tau) \approx (f\tau)^{-1}$ for the scaling regime, smoothly turning over to plateaus at the low and high-frequency limits.

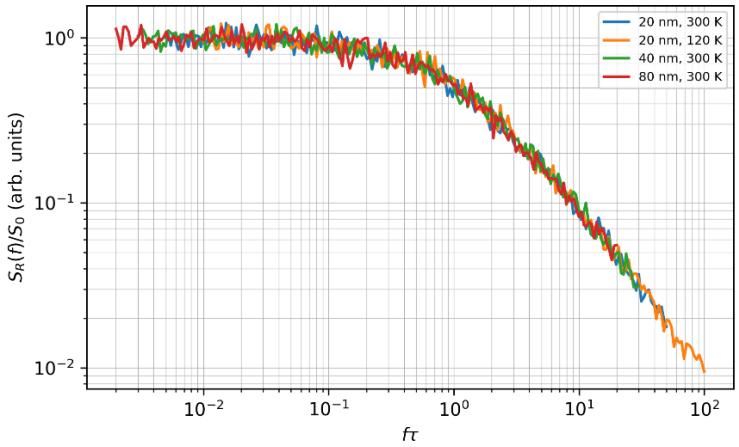

Figure 5 – Scaling collapse of normalized resistance noise spectra in $Ni_{80}Cr_{20}$ films

Upon rescaling, spectra from different devices and conditions collapse onto a common curve within about ±20–30 % over the central 1/f region (approximately $10^{-2} \lesssim f\tau \lesssim 1$). At very low fτ,

deviations arise from the finite duration of the time series, while at high fτ they are dominated by the residual white noise floor. To quantify the improvement achieved by rescaling, we computed the mean squared deviation between spectra before and after the transformation; the average inter-curve variance in log S_R is reduced by a factor of ≈3 in the scaling representation, demonstrating that a significant part of the thickness and temperature dependence can indeed be absorbed into S_0 and τ. The collapsed curve is well approximated by a simple form $\Phi(f\tau) \sim 1/(1 + f\tau)$ in the scaling regime.

These results indicate that, once trivial device-to-device factors are absorbed into S_0 and τ, the shape of the noise spectrum is essentially common to all disordered NiCr films studied here. We therefore speak of a "nearly universal" scaling function within this material system, while explicitly refraining from claiming universality across different materials and device concepts. This behaviour is consistent with theoretical pictures in which 1/f noise emerges from a broad, almost scale-free distribution of activation energies and barrier heights, with microstructural details such as grain size, grain-boundary density and surface oxidation primarily setting the overall noise level and correlation time rather than qualitatively changing the spectral form.

3.6. Microscopic considerations and limitations

The combined structural and noise data allow some tentative comments on microscopic mechanisms. AFM and TEM indicate that all films are nanocrystalline, with grain sizes increasing modestly with thickness but no evidence for large voids or compositional phase separation. It is therefore natural to attribute the majority of fluctuators to defects at grain boundaries, small composition fluctuations within grains, and possibly to oxygen-related states at the film surface and the NiCr/SiO_2 interface. The increase of normalized noise and non-Gaussianity in thinner films is consistent with the enhanced relative contribution of surfaces and interfaces in these samples. However, the present data do not allow us to unambiguously distinguish between different microscopic defect types, and additional experiments—such as in situ noise measurements during controlled annealing or oxidation—would be required to do so.

The study also has several clear limitations. Only a single alloy composition ($Ni_{80}Cr_{20}$) and three thicknesses are investigated, the frequency window is restricted to 0.1–100 Hz, and the device dimensions remain much larger than the electronic phase coherence length, so that UCF-type mechanisms are expected to be averaged out. Consequently, the conclusions drawn here apply primarily to macroscopic NiCr thin-film resistors used in precision electronics. Extending similar statistical and scaling analyses to other resistor materials (e.g. TaN, CrSi, granular metals), to wider frequency and temperature ranges, and to mesoscopic geometries would be a natural direction for future work.

4. Conclusions

Thin $Ni_{80}Cr_{20}$ films with thicknesses of 20, 40 and 80 nm were fabricated on Si/SiO_2 substrates and shown to be continuous nanocrystalline conductors with RMS roughness below ~1.5 nm and sheet resistances of ~350, 180 and 90 Ω/□ at 300 K, respectively. Device-to-device variations of thickness (<5 %) and sheet resistance (<10 %) confirm good process reproducibility across the wafer.

DC transport measurements in the temperature range 90–300 K confirmed strictly ohmic I–V characteristics for all devices and biases used in noise experiments, with a metallic-like decrease of resistance by ~10–20 % on warming. This ensures that all noise data were acquired in a linear-response regime without significant self-heating.

Normalized resistance noise spectra $S_R(f)/R^2$ exhibited near-ideal 1/f behaviour with spectral exponents $\alpha \approx 0.9–1.1$ over ~0.2–20 Hz. The normalized noise amplitude at 1 Hz decreased strongly with thickness, from about 3.2×10^{-10} Hz^{-1} for 20 nm films to 0.7×10^{-10} Hz^{-1} for 80 nm films, and the corresponding Hooge parameter at 300 K fell in the range $(1–3)\times10^{-3}$, placing the NiCr resistors within the low-noise regime of established thin-film technologies.

Time-domain analysis of normalized resistance fluctuations showed nearly Gaussian statistics for thicker films and higher temperatures, with small but systematic deviations (excess kurtosis up to ~0.8 and marginal KS p-values ≈0.03) emerging for the thinnest (20 nm) films at low temperatures. This pattern indicates that a large ensemble of fluctuators operates in thicker films, while thinner and colder samples are governed by a smaller effective number of active fluctuators, leading to heavier tails in the fluctuation distributions.

Scaling analysis demonstrated that, after rescaling spectra by a characteristic noise amplitude S_0 and correlation time τ, data from all thicknesses and temperatures approximately collapse onto a common master curve $S\_R(f) \approx S_0 \Phi(f\tau)$ over roughly two decades in $f\tau$. Quantitatively, the variance between spectra is reduced by about a factor of three in the scaled representation, supporting the existence of a nearly universal scaling function for 1/f noise within the studied NiCr films.

Taken together, these results address the initial research problem by showing that 1/f noise in resistive elements based on disordered NiCr films arises from a robust ensemble of relaxation processes whose collective behaviour is largely insensitive to microscopic details within this material system, whereas thickness and temperature primarily set the overall noise level, effective number of active fluctuators and characteristic time scale. The findings can be used to guide the design of low-noise resistive components—favouring thicker, less surface-dominated films for reduced normalized noise—and to benchmark theoretical models of 1/f noise in disordered metals.

The present study is limited to one alloy composition, a restricted frequency window and macroscopic device geometries; future work should extend similar statistical and scaling analyses to other materials, geometries and temperature ranges, and combine noise measurements with in situ structural or spectroscopic probes to link fluctuator statistics more directly to specific microscopic defects.

References

[1] S. Aryal and S. K. Mishra, “Probing cochlear compressive nonlinearity using signal-to-noise ratio–optimized distortion product otoacoustic emission input/output functions,” *J. Acoust. Soc. Am.*, vol. 158, no. 6, pp. 4335–4347, Dec. 2025, doi: 10.1121/10.0041765.

[2] O. Khaled, B. B. S. Tawfik, and M. N. Refaie, “Optimal Gene Selection and Machine Learning Framework for Alzheimer’s Disease Prediction Using Transcriptomic Data,” *Stat. Optim. Inf. Comput.*, vol. 14, no. 5, pp. 2276–2296, Oct. 2025, doi: 10.19139/soic-2310-5070-2723.

[3] H. Mao *et al.*, “Cortical aperiodic dynamics in hearing impairments predicts neural tracking of speech,” *Neuroimage*, vol. 320, Oct. 2025, doi: 10.1016/j.neuroimage.2025.121477.

[4] A. N. Pal *et al.*, “Microscopic mechanism of 1/f noise in graphene: Role of energy band dispersion,” *ACS Nano*, vol. 5, no. 3, pp. 2075–2081, Mar. 2011, doi: 10.1021/nn103273n.

[5] Y. Zhang, E. E. Mendez, and X. Du, “Mobility-dependent low-frequency noise in graphene field-effect transistors,” *ACS Nano*, vol. 5, no. 10, pp. 8124–8130, Oct. 2011, doi: 10.1021/nn202749z.

[6] P. Y. Chien *et al.*, “Quantum-interference origin and magnitude of 1/ f noise in Dirac nodal line IrO2nanowires at low temperatures,” *Appl. Phys. Lett.*, vol. 122, no. 14, Apr. 2023, doi: 10.1063/5.0147131.

[7] B. Sánta *et al.*, “Universal 1/ f type current noise of Ag filaments in redox-based memristive nanojunctions,” *Nanoscale*, vol. 11, no. 11, pp. 4719–4725, Mar. 2019, doi: 10.1039/c8nr09985e.

[8] J. Y. Hong, C. Y. Chen, D. C. Ling, I. Martínez, C. González-Ruano, and F. G. Aliev, “Low-frequency 1/f noise characteristics of ultra-thin AlOx-based resistive switching memory devices with magneto-resistive responses,” *Electron.*, vol. 10, no. 20, Oct. 2021, doi: 10.3390/electronics10202525.

[9] A. Ahmed and R. N. Tait, “Noise behavior of amorphous GexSi1-xOy for microbolometer applications,” *Infrared Phys. Technol.*, vol. 46, no. 6, pp. 468–472, Aug. 2005, doi: 10.1016/J.INFRARED.2004.11.003.

[10] M. Jalal, M. Lutful Hai, S. Ajmera, and M. Almasri, “Noise Reduction of Amorphous Si x Ge y O 1−x−y Thin Films for Uncooled Microbolometers by Si 3 N 4 Passivation and Annealing in Vacuum,” *IEEE Sens. J.*, vol. 16, no. 6, 2016, doi: 10.1109/JSEN.2015.2502272.

[11] Y. Li *et al.*, “Critical fluctuations and noise spectra in two-dimensional Fe3GeTe2 magnets,” *Nat. Commun.* , vol. 16, no. 1, Dec. 2025, doi: 10.1038/s41467-025-63578-w.

[12] J. Jaroszyński, D. Popović, and T. M. Klapwijk, “Universal Behavior of the Resistance Noise across the Metal-Insulator Transition in Silicon Inversion Layers,” *Phys. Rev. Lett.*, vol. 89, no. 27, 2002, doi: 10.1103/PhysRevLett.89.276401.

[13] N. Beev, “Measurement of Excess Noise in Thin Film and Metal Foil Resistor Networks”.

[14] A. F. Satrapinski, A. M. Savin, S. Novikov, and O. M. Hahtela, “Ni-Cr-based thin-film cryoresistors,” *IEEE Trans. Instrum. Meas.*, vol. 58, no. 4, pp. 1206–1210, 2009, doi: 10.1109/TIM.2008.2008579.

[15] O. J. Cinco-Izquierdo, C. A. De la Cruz-Blas, M. T. Sanz-Pascual, and J. J. Ocampo-Hidalgo, "Tunable Low Frequency Gm-C Low-Pass Filter using an OTA with Bootstrapping," *Circuits, Syst. Signal Process.*, vol. 44, no. 3, pp. 1443–1455, Mar. 2025, doi: 10.1007/s00034-024-02897-7.

Information about authors:
Azamat Sharipov – Master Student, Faculty of Physics and Technology, Al-Farabi Kazakh National University, Almaty, Kazakhstan, sharipov_az@list.ru

Author Contributions:
Azamat Sharipov – concept, methodology, resources, data collection, testing, modeling, analysis, visualization, interpretation, drafting, editing, funding acquisition.

Conflict of Interest: The authors declare no conflict of interest.

Use of Artificial Intelligence (AI): The authors declare that AI was not used.

Received: 27.10.2025
Revised: 14.12.2025
Accepted: 27.12.2025
Published: 30.12.2025